Charge and spin transport in carbon nanotubes:
From Coulomb blockade to Fabry-Perot interference

DISSERTATION ZUR ERLANGUNG DES DOKTORGRADES DER NATURWISSENSCHAFTEN
(DR. RER. NAT.) DER FAKULTÄT FÜR PHYSIK
DER UNIVERSITÄT REGENSBURG

vorgelegt
von

Alois Roman Dirnaichner

aus

Wasserburg am Inn

im Jahr 2016

Promotionsgesuch eingereicht am:
2.7.2015

Die Arbeit wurde angeleitet von:

Prof. Christoph Strunk

Prüfungsausschuss:

Vorsitzender: Prof. Dr. F. Gießibl
1. Gutachter: Prof. Dr. C. Strunk
2. Gutachter: Prof. Dr. M. Grifoni
weiterer Prüfer: Prof. Dr. V. Braun

Termin Promotionskolloquium: 27.4.2016

Contents

Part I

Introduction

More than 60 years after its first observation in 1952 by Radushkevich et al. [1], see Fig. 1, and 24 years after its re-discovery in 1991 [2], carbon nanotubes (CNTs) are still primarily a subject of fundamental research. With a few exceptions, e.g., when used as an additive in material compounds to increase the structural performance, CNTs can not compete with state-of-the-art materials. In electronic applications this is insofar a pity, as its superior performance as a field-effect transistor [3] or as electric wiring [4] is left idle due to the fabrication process that does not meet industrial standards. However, the predominance of silicon based semi-conductor technology is starting to wane. Since transistor sizes dropped below 22 nm, it is getting more and more difficult to overcome limitations of the fabrication process in further refinements [5]. This is currently leading to a deviation from Moore's law, a law predicting a doubling of the density of transistors in integrated circuits every two years [6]. As a result, interest grows in potential alternatives. Single-wall CNTs, being $2-5$ nm thin and ballistic conductors with high mobility, are natural candidates to overcome part of the limitations [7]. Fundamental research on the electronic properties of CNTs is important to prepare the ground for this applications.

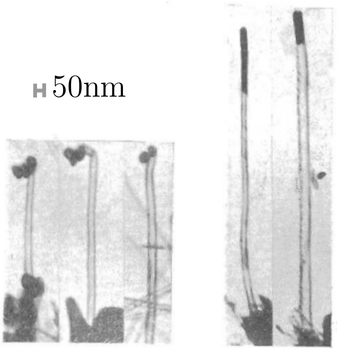

Figure 1: Multiwall CNTs in transmission electron micrographs recorded by Radushkevich et al. [1].

This said, let us share with you another, our, incentive to study CNTs. We do not sell integrated circuits. It is the fascination for a unique and versatile electronic material system that encourages us. In this work we will *only* study electronic transport properties of CNTs at low temperature, in a setup with source and drain contacts and a means to control the electrochemical potential of the CNT. This is quite a limited scope: We do not discuss nanomechanical properties [8, 9], properties at intermediate or room temperatures [10], superconducting properties [11, 12], multi-dot setups [13] etc. Still, with this ingredients we are able to study a wealth of physical phenomena. Fig. 2 shows a phase diagram of the transport regimes in this setup for a typical small bandgap carbon nanotube. The grey line trace is taken from an actual measurement of a CNT at low temperatures and low bias voltage. To the right of the band-gap, we find the regime of sequential tunneling. A quantum dot is formed on the CNT. The Coulomb force between the electrons on the CNT and the incident electrons allows for the counting of electronic charges on the CNT. In this regime, we can, e.g.,

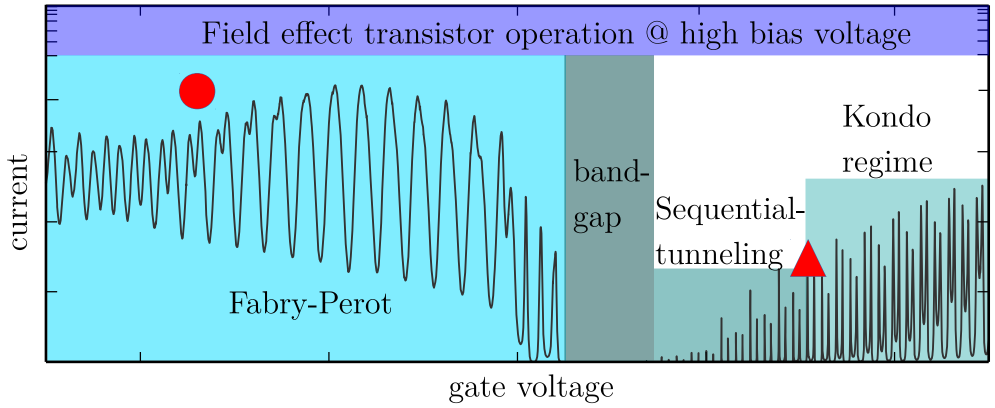

Figure 2: "Phase diagram" of electron transport in a CNT at low temperatures. The different regimes can be distinguished by the transparency of the contacts. In the sequential tunneling regime, the coupling is weak and increases with higher gate voltage until we reach the Kondo regime. In the Fabry-Perot regime to the left of the band-gap, the coupling is strongest. Applying large bias, $\sim 50\,\mathrm{mV}$, the CNT in the source-drain-gate setup can be operated as a ballistic field effect transistor. The red filled circle and the red triangle indicate the regimes that are discussed within this work.

use a magnetic field to trace the evolution of the sharp transitions between few-electron charging states [14]. Similarly, the transitions through excited states of the first and second charging state can be mapped by a magnetic field. This is insofar interesting, as the states in CNTs have both spin and orbital degrees of freedom that couple differently to the field [14–16]. The evolution of these transitions can be predicted from microscopical models. When we increase the gate voltage, we increase the coupling to the CNT and the current increases. The increased coupling enables correlations between electrons on the dot and in the contacts and the Kondo effect can be observed. Due to the entangled spin and orbital degrees of freedom in CNTs, the Kondo effect in this system is of particular interest [17]. The tool of choice in this regime is the spectroscopy of tunneling through excited states in the blockade region [18].

In the regime to the left of the band gap, hole transport takes place. While the coupling to the CNT in limited by p-n junctions on the electron side in p-doped CNTs [19], the transparency of the contacts in the hole region is usually high and allows for ballistic transport with conductances up to the maximum of a 4-channel conductor, $4\,\mathrm{e}^2/\mathrm{h}$ [20]. In carefully fabricated, clean CNT devices we can observe electron interference effects in this regime, in full analogy to the optical Fabry-Perot effect [21]. Finally, as already mentioned, CNTs can be studied in the role of high performance field effect transistors at high bias voltage [22].

Within this work we will in the first part focus on the intermediate regime between the sequential tunneling and the Kondo regime (highlighted by a red triangle in Fig. 2). While we observe no signatures of the Kondo effect, it turns out that a key aspect to the understanding of the experiment is the incorporation of charge fluctuations between the CNT and the contacts going beyond the concept of sequential tunneling. In the second part, we report on wave interference patterns in the Fabry-Perot regime (red circle). The interference of modes from the different channels in the CNT reveals details on the geometrical structure of the specimen. Although covering only a small part of the phase diagram we hope to provide a glimpse on the rich variety of electronic transport in CNTs.

Part II

Tunneling magneto-resistance in a carbon nanotube quantum dot

Chapter 1

Introduction to quantum dot transport in the Coulomb blockade regime

The term "quantum dot" was first introduced to describe semiconductor microcrystals which host spatially confined excitons [23]. The absorption spectra of the cavities are related directly to the quantum mechanical confinement of the exciton states in the quantum dot. Similarly, an electron can be confined in all spatial dimensions, such that the energy required to overcome the confining potential is large with respect to the quantum confinement energy ε. When ε, in turn, is large with respect to the kinetic energy of the electron, it is considered to be in a quantum dot. The single particle energy spectrum of the quantum dot is then restricted to discrete levels n with energies $\varepsilon_n(L)$. Quantum dot behavior can be observed at room temperature for dots with extensions of a few nanometer [24, 25]. At temperatures of a few hundred millikelvin, contrarily, the electron is sensitive to barriers separated by micrometers.

One well established setup to study quantum dot systems is by means of electronic transport spectroscopy. We couple two separate metallic reservoirs *source* and *drain* with electrochemical potentials μ_s and μ_d to the quantum dot. The coupling strength is described by coupling parameters Γ_j, $j \in \{\mathrm{s}, \mathrm{d}\}$. For a finite current to flow, we apply a potential difference between the reservoirs, see Fig. 1.1(a). The potential of the electrons on the quantum dot can be controlled by a capacitively coupled gate reservoir.

By correctly tuning the effective couplings Γ_j, and the reservoir potentials, electrons can traverse the quantum dot by subsequent tunneling between the source reservoir, the quantum dot and the drain reservoir. The current across the system can be calculated by applying the Landauer-Büttiker

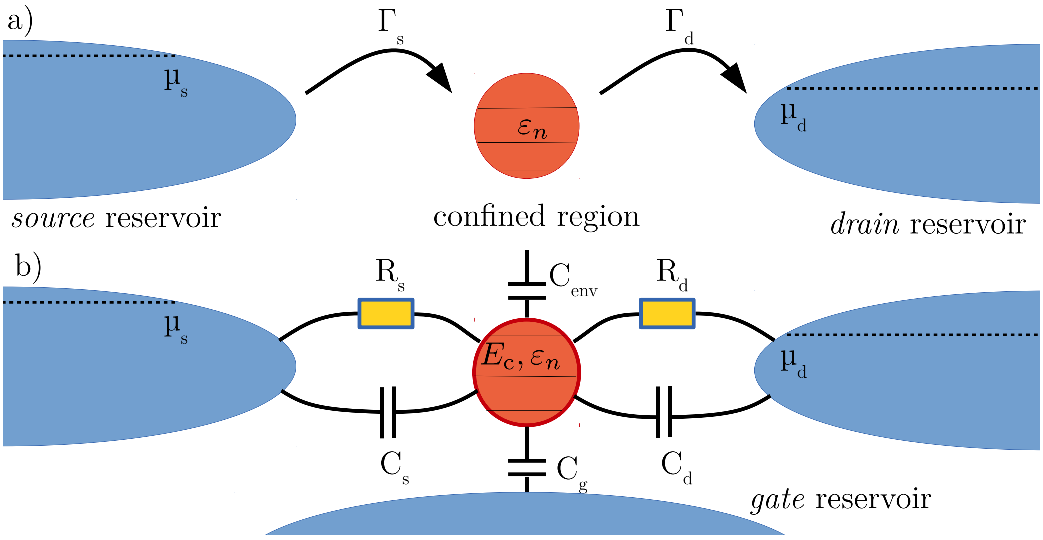

Figure 1.1: Schematic drawing of a quantum dot setup. (a) In a classical transport measurement, electrons tunnel from the source reservoir on the left to the confined region in the center at a rate Γ_s. The single particle states in the confined region are restricted to energies $\varepsilon_n(L)$. The out-tunneling to the drain reservoir takes place at a rate Γ_d. (b) The interactions of the electrons on the dot with the electrons in the leads, in the gate and in the environment can be modeled by capacitances in a replacement circuit. The energy E_c required to charge the dot with a single electron is determined by the capacitances. The rates Γ_j correspond to resistances in the replacement circuit.

formalism [26],

$$I = \frac{2e}{h} \int \mathrm{d}E\, \mathcal{T}(E)[f_\mathrm{s}(E) - f_\mathrm{d}(E)], \tag{1.1}$$

where $\mathcal{T}$ is the transmission function which includes the couplings Γ_j and the Fermi function $f_j(E) = (1 + \exp((E - \mu_j)/k_\mathrm{B}T))^{-1}$ describes the continuum of states in the source and drain reservoirs.

In a measurement, the situation is complicated by the inevitable presence of other electrons on the quantum dot, the leads and the gate reservoir. Within a first approximation, a replacement circuit can be used where capacitances to the leads, C_j, to the gate, C_g and to the environment, C_env capture the effects of the electronic Coulomb interaction of the electrons on the dot with its surroundings, see Fig. 1.1(b). In the same spirit, the couplings Γ_j to source and drain can be viewed as resistors R_j parallel to the capacitances C_j. In terms of resistivities, a more concise definition of the spatial confinement of electrons on a coupled quantum dot can be given: The resistance between the quantum dot and the lead reservoirs has to exceed the resistance quantum $R_\mathrm{K} \simeq 25.8\,\mathrm{k}\Omega$, otherwise quantum fluctuations between the dot and the reservoirs would dominate transport [27] and no single integer charges can be distinguished in electron transport experiments.

An in tunneling electron has to overcome an electrostatic charging energy $E_\mathrm{c} = e^2/2C_\Sigma$, where $C_\Sigma = C_\mathrm{s} + C_\mathrm{d} + C_\mathrm{g} + C_\mathrm{env}$. When the transport across the quantum dot is blocked because the charging energy is to large for incident electrons, the quantum dot is termed to be in the Coulomb blockade. This effect has been observed first in metallic islands in thin metallic films [28], a classical system where the energy quantization due to spatial confinement does not play a role but the capacitance of the islands is small enough for the charging energy to dominate. In the *quantum* Coulomb blockade, on the other hand, the confinement energy is comparable to the charging energy. Thus, depending on the charging energy E_c, the confinement energy ε_n, the thermal energy $k_\mathrm{B}T$ and the couplings Γ_j, we distinguish parameter regimes where either the classical or the quantum Coulomb blockade dominates, or neither is present.[1] We summarize the presented arguments in Tab. 1.1.

1.1 Quantum dot spectroscopy

In the transport experiments described here we can control the potential drop between source and drain reservoir – the bias voltage $-eV_\mathrm{b} = \mu_\mathrm{s} - \mu_\mathrm{d}$

---

[1] For this distinction we restrict ourselves to transport at low bias voltage V_b, i.e., $\mathrm{e}V_\mathrm{b}$ is one of the small energy scales in our system.

(Ia)	$k_\mathrm{B}T \gg E_\mathrm{c}, \varepsilon_n$	no blockade (large temperature)
(Ib)	$R_{\mathrm{s}/d} < R_\mathrm{K}$	no blockade (no confinement)
(II)	$E_\mathrm{c} \gg k_\mathrm{B}T \gg \varepsilon_n, \min(\Gamma_j)$	classical Coulomb blockade (CB)
(IIIa)	$E_\mathrm{c} > \varepsilon_n \gg k_\mathrm{B}T > \min(\Gamma_j)$	quantum CB, thermal broadening
(IIIb)	$E_\mathrm{c} > \varepsilon_n \gg \min(\Gamma_j) > k_\mathrm{B}T$	quantum CB, lifetime broadening

Table 1.1: Different electron transport regimes. From top to bottom, the temperature decreases. (Ia) At high temperature, the thermal energy of the electrons in large enough to overcome Coulomb blockade. (Ib) Confinement is also absent if the contact resistances are small. (II) If the electrostatic charging energy is larger than the temperature, current is blocked due to Coulomb repulsion. (III) As an additional scale, the quantum mechanical confinement energy becomes relevant for sufficiently small structures. In this regime of quantum Coulomb blockade, the electron transport at low bias voltages can either be dominated by the thermal energy (IIIa) or by the inverse lifetime energy scale Γ_j (IIIb).

– and the potential on the dot via a capacitively coupled gate reservoir at an electrochemical potential V_g. In the following we keep the drain contact grounded and modify the potential of the source reservoir by V_b. The other parameters of the system, namely the coupling between the dot and the lead reservoirs that determine the rates Γ_j or the capacitive coupling to the gate reservoir are specific to the sample in question and can not be changed independently in the course of a measurement. In a typical characterization measurement of a quantum dot in the quantum Coulomb blockade regime (compare Tab.1.1), we measure the differential conductance as a function of gate and bias voltages, $G \equiv \mathrm{d}I\ /\mathrm{d}V_\mathrm{b}\ (V_\mathrm{g}, V_\mathrm{b})$. A typical result of such a measurement is sketched in Fig. 1.2(a).

The electro-chemical potential of the quantum dot is the minimum energy for adding the Nth electron to the dot, i.e., $\mu_\mathrm{dot}(N) = U(N) - U(N-1)$, where $U(N)$ is the total ground state energy for N electrons on the dot at zero temperature [29]. Under the assumptions given above, namely that the electron-electron interaction between electrons on the dot and in the reservoirs can be modeled capacitively and under the additional assumption that these capacitances are independent of N, the electro-chemical potential of the quantum dot reads [29]

$$\mu_\mathrm{dot}(N, V_\mathrm{g}) = \varepsilon_N + \frac{e^2}{C_\Sigma}(N + 1/2) - \alpha e V_\mathrm{g}, \tag{1.2}$$

where the capacitive influence of the gate reservoir is incorporated in $\alpha = \frac{C_\mathrm{g}}{C_\Sigma}$.

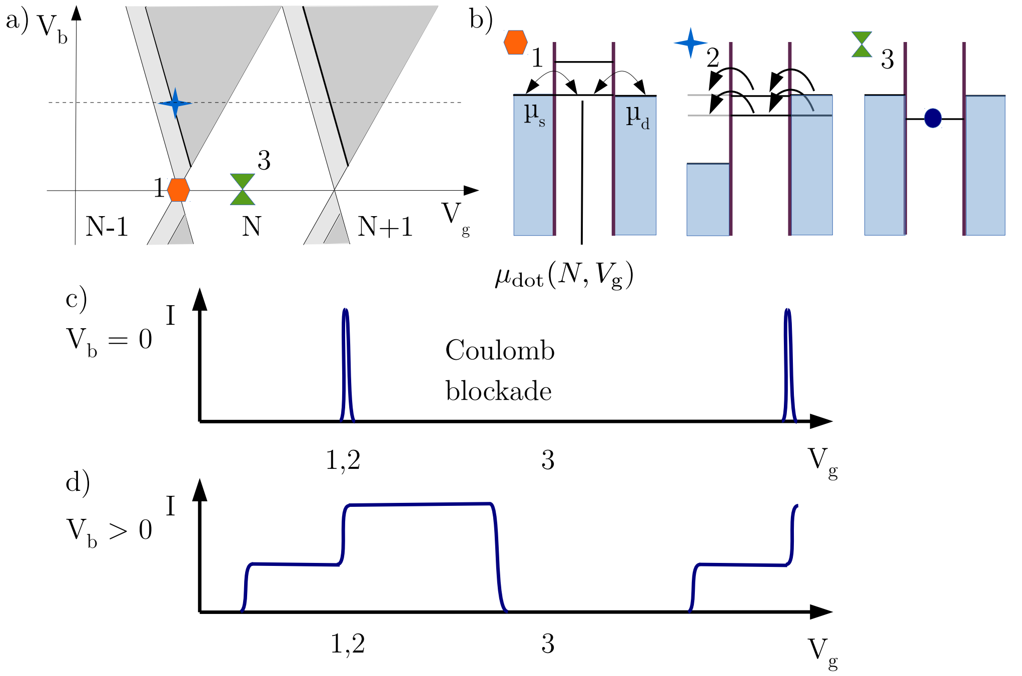

Figure 1.2: A short review on transport spectroscopy in the Coulomb blockade regime. (a) Schematic drawing of a current measurement as a function of gate and bias voltage. In the white region, the current is blocked and the number of electrons (given below the x-axis) is constant. (b) Electrochemical potentials for three specific value-pairs of bias and gate voltage highlighted in (a). In 1, transport takes place through the ground state while in 2, a transition through an excited state contributes to the current. In 3, the current is blocked and the electron number on the dot is fixed to N. (c) Current plotted as a function of gate voltage at zero bias. When the potentials of the dot and of the leads are aligned a peak is visible in the current signal. (d) At finite bias, we observe steps when additional states contribute to the transport.

In Eq. (1.2), the first term is the *chemical* potential, $\mu_{\mathrm{ch}} = \varepsilon_N$, while the other terms belong to the *electrostatic* potential $e\phi_N$. The addition energy, i.e., the energy difference between two charging states with N and $N+1$ electrons is given by

$$\Delta\mu_N = \mu_{\mathrm{dot}}(N) - \mu_{\mathrm{dot}}(N-1) = \varepsilon_0 + \frac{e^2}{C_\Sigma}, \tag{1.3}$$

where we replaced the difference between the single particle energy states by a constant, $\varepsilon_N - \varepsilon_{N-1} = \varepsilon_0$. Note that we thereby assume that the single particle energies increase linearly with N.

At low bias and low temperature, i.e., $eV_{\mathrm{b}}, k_{\mathrm{B}}T \ll E_{\mathrm{c}}$, the condition for electron transport reads $\mu_{\mathrm{s}} = \mu_{\mathrm{dot}}(N) = \mu_{\mathrm{d}}$. This situation is shown in Fig. 1.2(b) and marked by a hexagon in the stability diagram in Fig. 1.2(a). Sweeping the gate voltage we thus expect a series of peaks in the current signal, separated by regions of the size $\Delta\mu_N/\alpha$, where the tunneling is blocked by the Coulomb repulsion, see Fig. 1.2(c).

At finite bias, the situation is slightly different. The electro-chemical potential of the quantum dot with N electrons is modified by the capacitance to the reservoirs, i.e.,

$$\mu_{\mathrm{dot}}(N, V_{\mathrm{g}}, V_{\mathrm{b}}) = \varepsilon_N + \frac{e^2}{C_\Sigma}(N+1/2) + e(\alpha_{\mathrm{s}}V_{\mathrm{b}} - \alpha V_{\mathrm{g}}) \tag{1.4}$$

where $\alpha_{\mathrm{s}} = C_{\mathrm{s}}/(C_{\mathrm{s}} + C_{\mathrm{d}})$ describes the capacitive influence of the source reservoir on the quantum dot in relation to the drain reservoir [30].

At $eV_{\mathrm{b}} > k_{\mathrm{B}}T, \min(\Gamma_j)$, the condition $\mu_{\mathrm{s}} \leq \mu_{\mathrm{dot}} \leq \mu_{\mathrm{d}}$ and $\mu_{\mathrm{d}} > E_{\mathrm{d}}^{\mathrm{i}}$ defines a range of V_{g} values where tunneling from drain to source is possible. Sweeping the gate voltage we observe steps in the current signal, Fig. 1.2(d), and, consequently, peaks in the conductance signal (not shown). Note that electrons can also tunnel through states of higher energy, e.g., the next state with $\mu^*_{\mathrm{dot}}(N) = \mu_{\mathrm{dot}}(N) + \varepsilon_0$, if the bias window is large enough. Such a situation is highlighted by a blue star in Fig. 1.2(a) and depicted in the second level scheme in (b). If the conditions $\mu_{\mathrm{s}} < \mu^*_{\mathrm{dot}}(N)$ and $\mu_{\mathrm{d}} > \mu^*_{\mathrm{dot}}(N)$ is met, the excited state contributes to the transport and we observe an additional step in the current Fig. 1.2(d) and a line in $G = dI/dV_{\mathrm{b}}$ (not shown).

In Fig. 1.2(c), the finite width of the peaks is determined by the temperature of the Fermi liquid in the lead reservoirs, compare Eq. (1.1). From this consideration the condition $E_{\mathrm{c}} \gg k_{\mathrm{B}}T$ arises naturally as a requirement to observe a Coulomb blockade signature similar to the one sketched in (c).

1.2 A carbon nanotube quantum dot

To this point, we did not touch the specific nature of the quantum dot. We assumed that the dot is a region that is confined in all spatial dimensions and this confinement determines the allowed electronic states by imposing boundary conditions on the solutions to the Schrödinger equation, $\Psi_n(\vec{k}, \vec{r})$. This implies a quantization of the wavevector $\vec{k}$ and a discretization of the energy spectrum. The relation between electron energy and wave vector on the quantum dot is given by the potential landscape that is set by the molecular arrangement of the quantum dot material.

In our case, the quantum dot under consideration is made up by a section of a carbon nanotube. The electron wavefunction forms a standing wave similar to the free particle-in-the-box textbook case, see Fig. 1.3. However, due to the particular nature of the graphene lattice, the relation between the wave vector and the quantization energy is linear in carbon nanotubes[2] and, hence, such is the relation between the quantization energy and the tube length. We can understand most of the properties of a nanotube by considering the properties of a graphene sheet and taking into account the additional boundary conditions that are imposed by wrapping the sheet. This approach is termed the "zone-folding approximation" [31].

1.2.1 The graphene dispersion relation

Graphene is an atomically thin layer of graphite. Its peculiar electronic properties arise from the perfect honeycomb lattice that is formed by the carbon atoms. The sp^2-hypridized orbitals of the carbon atoms form σ-bonds at 120° angles in the plane, see Fig. 1.4(a). The unit cell is spanned by two vectors

$$\vec{a}_1 = \left(\frac{\sqrt{3}a}{2}, \frac{a}{2}\right) \qquad \text{and} \qquad \vec{a}_2 = \left(\frac{\sqrt{3}a}{2}, -\frac{a}{2}\right),$$

and contains two atoms attributed to sublattices A and B. The lattice constant (common to both lattices) is given by

$$a = |\vec{a}_1| = |\vec{a}_2| = a_{\mathrm{cc}}\sqrt{3} = 2.46\text{Å},$$

where $a_{\mathrm{cc}} = 1.42\,\text{Å}$ is the inter atomic distance of the carbon atoms, see Fig. 1.4(a). Correspondingly, the *reciprocal* lattice can be constructed with two symmetry points $\vec{K}$ and $\vec{K}'$ (also called Dirac points) in the first Brouillon

---

[2] The CNT dispersion is approximately linear for states with energies $\varepsilon \lesssim 1\,\mathrm{eV}$.

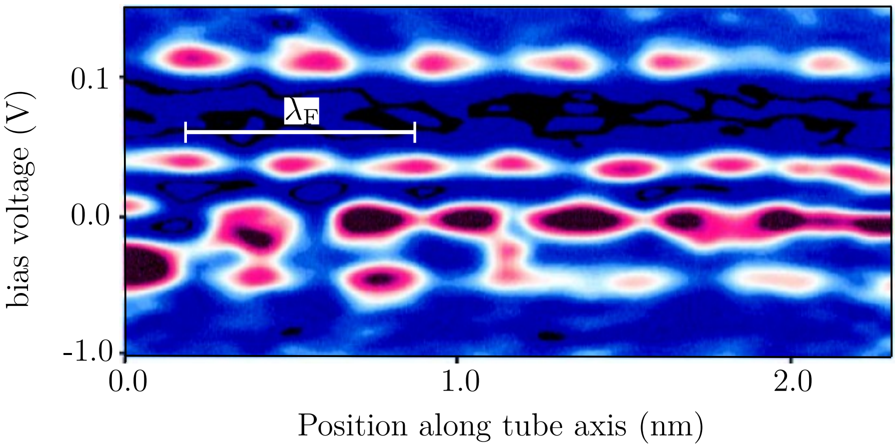

Figure 1.3: Conductance from an STM tip to a CNT as a function of the position along the CNT and the applied bias voltage, adapted from Ref. [32]. The modulation of the conductance is interpreted as a modulation of the electron wavefunction in the CNT quantum dot where it forms a standing wave with a wavelength close to $\lambda_F = 0.74\,\text{nm}$, the Fermi wavelength in carbon nanotubes.

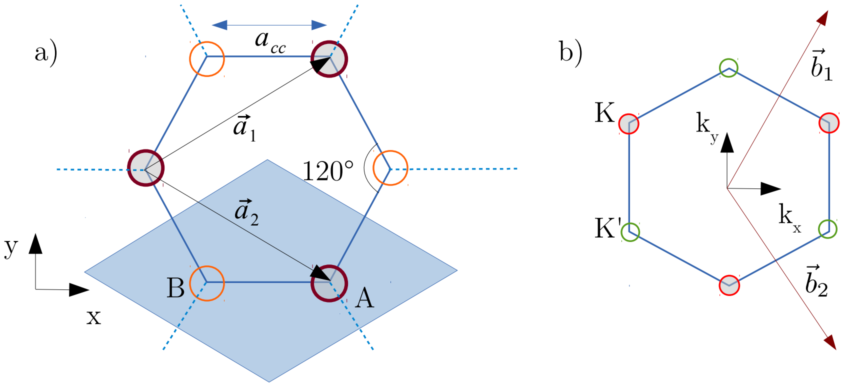

Figure 1.4: (a) A segment of the graphene lattice. The small circles represent carbon atoms, the lines between them represent σ-bonds. Note that the graphene sheet can be built from two identical sublattices A and B with common unit lattice vectors $\vec{a}_1$ and $\vec{a}_2$. The blue shaded region highlights a unit cell of the graphene lattice. (b) The first Brouillon zone of the graphene lattice with lattice vectors $\vec{b}_1$ and $\vec{b}_2$. Corresponding to the sublattices A and B we find points $\vec{K}$ and $\vec{K}'$ in the reciprocal space.

zone,

$$\vec{K} = \left(-\frac{2\pi}{3a}, \frac{2\pi}{3\sqrt{3}a}\right) \qquad \text{and} \qquad \vec{K}' = \left(-\frac{2\pi}{3a}, -\frac{2\pi}{3\sqrt{3}a}\right). \tag{1.5}$$

We denote the length of these vectors by $|\vec{K}| = |\vec{K}'| = 4\pi/3\sqrt{3}a \equiv K$. The unit cell in the reciprocal lattice is spanned by unit vectors

$$\vec{b}_1 = \left(\frac{2\pi}{\sqrt{3}a}, \frac{2\pi}{a}\right) \qquad \text{and} \qquad \vec{b}_2 = \left(\frac{2\pi}{\sqrt{3}a}, -\frac{2\pi}{a}\right). \tag{1.6}$$

The overlapping wave functions of the sp^2-hybridized electrons in the bonds form bands σ and σ^* away from the Fermi energy which do not contribute to electronic transport. The remaining p_z orbitals are oriented perpendicular to the honeycomb lattice and constitute bonding π and anti-bonding π^* bands. Electrons within these bands can move freely across the lattice and are responsible for the ballistic electron transport observed in graphene [33].

The dispersion relation of the valence (π^*) and conduction (π) bands can be calculated by a tight-binding approach considering states on a graphene lattice with nearest neighbor overlap [34]. The dispersion relation reads [31]

$$\varepsilon_{\pm}^{\mathrm{2D}}(\vec{k}) = \pm t \sqrt{1 + 4\cos\left(\frac{\sqrt{3}k_x a}{2}\right)\cos\left(\frac{k_y a}{2}\right) + 4\cos^2\left(\frac{k_y a}{2}\right)}, \tag{1.7}$$

where the plus sign applies to the π^* and the minus sign to the π band, and the overlap energy is $t = 2.6 \pm 0.1\,\mathrm{eV}$ [31]. The energy surface defined by this relation is plotted in Fig. 1.5 for $t = 2.7\,\mathrm{eV}$. In the vicinity of the $\vec{K}$ and $\vec{K}'$ points the dispersion can be linearized. For a wave vector $\vec{q} = \vec{k} - \vec{K}$, with $\vec{q} \ll \vec{k}_{\mathrm{F}}$, we obtain

$$\varepsilon_{\pm}^{\mathrm{2D}}(\vec{q}) \approx \pm v_{\mathrm{F}}|\vec{q}| + O[(|\vec{q}|/K)^2], \tag{1.8}$$

a linear function of $|\vec{q}|$ resembling the energy-momentum relation of a massless particle as a solution of the Dirac equation ($\vec{q}$ is measured from the Dirac points). From Eq. (1.7) it follows that $v_{\mathrm{F}} = \sqrt{3}at/2 \approx 8\cdot 10^5\,\mathrm{m/s}$ for $t = 2.5\,\mathrm{eV}$. In Fig. 1.5, a zoom-in shows one of the Dirac cones, i.e., the linear dispersion relation in the direct vicinity of a Dirac point.

1.2.2 The carbon nanotube dispersion relation

Conventionally, the structure of the rolled graphene sheet that forms a carbon nanotube is characterized by its vector around the circumference in the basis

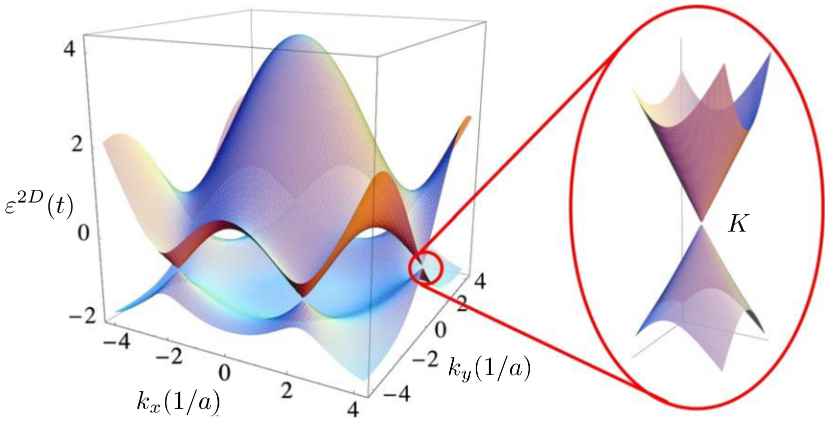

Figure 1.5: The electronic dispersion relation in graphene plotted as a surface in $\vec{k}$-space. Clearly visible are the touching points between conductance and valence bands, the Dirac points. A zoom to one of these points highlights the linear evolution of the particle energy with the absolute value of $\vec{q}$ in the vicinity of the Dirac points. Adapted from Ref. [35].

of the graphene lattice vectors $\vec{a}_1$ and $\vec{a}_2$, i.e., $\vec{C} = n\vec{a}_1 + m\vec{a}_2 = (n, m)$. This vector forms an angle θ with the vector $\vec{a}_1$,

$$\cos(\theta) = \frac{\vec{C} \cdot \vec{a}_1}{|\vec{C}||\vec{a}_1|} = \frac{2n+m}{2\sqrt{n^2+m^2+nm}}, \tag{1.9}$$

where the hexagonal lattice symmetry restricts the *chiral angle* θ to $0° \leq \theta \leq 30°$ and the values of m to $0 \leq m \leq n$. The diameter of a CNT is $d = |\vec{C}|/\pi$. In Fig. 1.6(A), examples are given for possible wrappings of the graphene sheet that form carbon nanotubes with $\vec{C} = (11, 0)$ and $\vec{C} = (11, 7)$. The atomic structure of the latter is shown in the STM image in Fig. 1.6(B). The special cases $m = 0$ and $m = n$ are named according to the shape of the graphene “edge” along the vector C. Nanotubes where $m = 0$ are classified as *zig-zag* nanotubes while CNTs with $m = n$ belong to the *armchair* class. The vast majority of possible geometries that do not fall into these two categories are called *chiral* tubes [31]. The smallest lattice vector $\vec{T}$ perpendicular to $\vec{C}$ determines the translational period $t = |\vec{T}|$ of the tube. In the basis of the graphene lattice vectors, $\vec{T} = t_1\vec{a}_1 + t_2\vec{a}_2$, the components read

$$t_1 = \frac{2m+n}{\gcd(2m+n, 2n+m)} \qquad \text{and} \qquad t_2 = -\frac{2n+m}{\gcd(2m+n, 2n+m}, $$

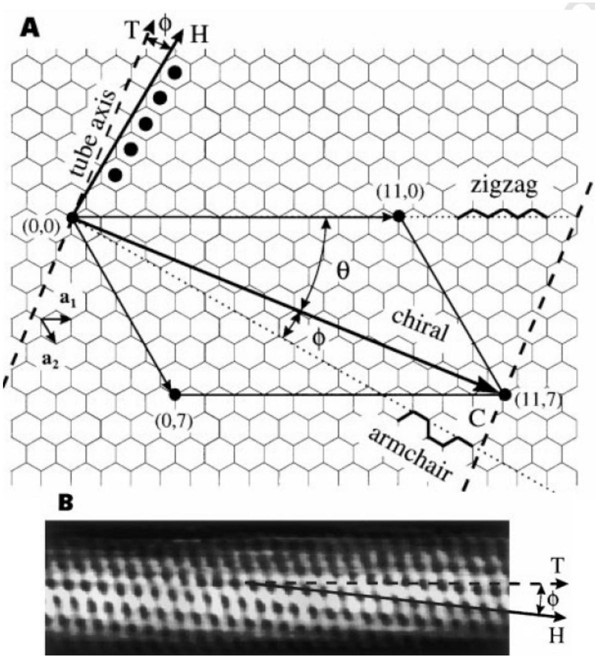

Figure 1.6: (A) Characterization of the carbon nanotube geometry. A nanotube is formally constructed by rolling a graphene sheet along the vector $\vec{C}$. The translational vector $\vec{T}$ points along the tube axis. The angle between $\vec{C}$ and $\vec{a}_1$ is denoted by the chiral angle θ. A CNT with $\theta = 0°$ is called a *zigzag* CNT, a CNT with $\theta = 30°$ is called an *armchair* CNT. (B) Atomically resolved STM images of a *armchair-like* CNT with a chiral angle of $\theta = 27°$ and a diameter of $d = 1.3\,\text{nm}$, corresponding to the $(11, 7)$ nanotube whose chiral vector is shown in (A). Adapted from Ref. [36].

where $\gcd(n_1, n_2)$ is the greatest common divisor of n_1 and n_2. $\vec{C}$ and $\vec{T}$ span the *translational* unit cell of the CNT. We can also define a CNT unit cell using elementary *helical* chains. From the *helical* model, the distinction between different bands due to their crystal angular momentum $\mathfrak{m}$ arises naturally. Please refer to Ref. [37] for a presentation of the *helical* model.

The most prominent effect of the wrapping on the dispersion relation $E^{\mathrm{g}}_{\pm}$ of graphene is the restriction of the wave vector perpendicular to the nanotube axis to values spaced by $\Delta k_{\perp} = 2\pi/|\vec{C}|$. The quantum mechanical confinement energy due to the radial confinement is of the order of eV (e.g., 1.1 eV for the nanotube in Fig. 1.6), so the dispersion relation is effectively restricted to the lowest subband in the bias and gate voltage ranges of the experiments presented in this work. Within a first approximation, we can deduce the carbon nanotube dispersion from the graphene dispersion by restricting the values of the wave vector to the one-dimensional subbands, i.e.,

$$\varepsilon(k_{||}, \mu) = \varepsilon^{\mathrm{2D}}_{\pm} \left(k_{||} \frac{\vec{K}_2}{|\vec{K}_2|} + \mu \vec{K}_1 \right), \tag{1.10}$$

where $\mu = 1, 2, \ldots, N$ is an integer counting the subbands up to the number of carbon atom pairs in the translational unit cell N and

$$\vec{K}_1 = \frac{-t_2 \vec{b}_1 + t_1 \vec{b}_2}{N} \qquad \text{and} \qquad \vec{K}_2 = \frac{m \vec{b}_1 - n \vec{b}_2}{N}.$$

From Eq. (1.10) we can distinguish metallic and semi-conducting nanotubes. If for some μ the vector $k_{||} \frac{\vec{K}_2}{|\vec{K}_2|} + \mu \vec{K}_1$ is equal to $\vec{K}$ or $\vec{K}'$, the valence band touches the conduction band and the tube is metallic, otherwise it is semi-conducting. It is straightforward to derive the condition for a metallic nanotube using Eq. (1.5),

$$n - m = 3q,$$

where q is an integer number [38].

Classification of CNTs in terms of crystal angular momentum

We can further subdivide the large number of different chiral CNT geometries by the crystal angular momentum quantum number $\mathfrak{m}$ of the electrons in the lowest lying one-dimensional subbands, i.e., the bands crossing the Dirac point in the $\vec{k}$-plane. Note that the assignment of $\mathfrak{m}$ to a band is possible only in the *helical* picture [39]. The crystal angular momentum in the *armchair-like* class CNTs in these bands is always zero which can be expressed by

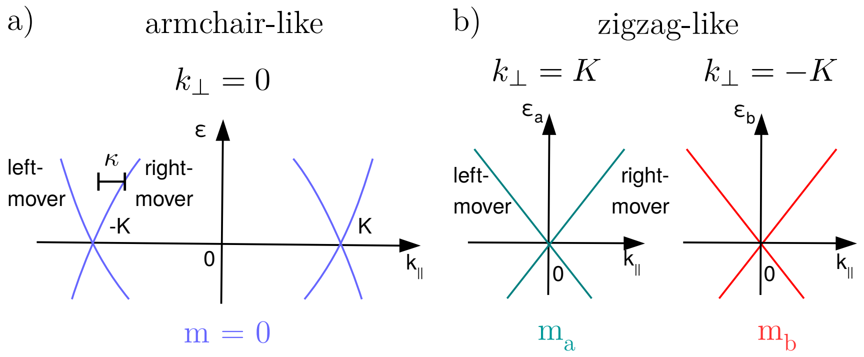

Figure 1.7: Dispersion of the lowest lying band(s) in metallic CNTs. (a) In *armchair-like* CNTs, all states on the lowest lying conduction band share the same angular momentum, $m = 0$. The wave vector component perpendicular to the CNT axis is proportional to the angular momentum, $k_\perp = 0$. The branch to the left of the $\vec{K}$ or $\vec{K}'$ point in each valley is denoted the *left-mover* branch, the right branch is denoted the *right-mover* branch. The distance to the closest Dirac point is measured by κ. (b) *zigzag-like* CNTs host states with different angular momenta in the vicinity of the two Dirac points. Here, $k_\perp = \pm K$ in the two valleys, respectively.

the relation $(n-m)/\mathfrak{n}|_{\mathrm{mod}\,3} = 0$, where $\mathfrak{n} = \gcd(n, m)$ [37], see Fig. 1.7(a). Note that metallic *armchair* tubes with $n = m$ are a special case within this class. All other metallic tubes have non-zero angular momentum $\mathfrak{m}_a = (2n+m)/3|_{\mathrm{mod}\,\mathfrak{n}}$ and $\mathfrak{m}_b = (2m+n)3_{\mathrm{mod}\,\mathfrak{n}}$ in the bands crossing the $\vec{K}$ and $\vec{K}'$ points, respectively [39]. Since the angular momentum is defined mod $\mathfrak{n}$, we can always choose $\mathfrak{m}_a$ and $\mathfrak{m}_b$ with $\mathfrak{m}_a = -\mathfrak{m}_b$ which is required by time-reversal symmetry. The CNTs with different angular momentum for the states in the two valleys fall into the *zigzag-like* class, see Fig. 1.7(b). Again, *zigzag* CNTs with $m = 0$ are a special case within this class. In terms of the indices (n, m) we can distinguish *armchair-like* (and *armchair*) CNTs that satisfy $(n-m)/\mathfrak{n}|_{\mathrm{mod}3} = 0$, and *zigzag-like* (and *zigzag*) CNTs where $(n-m)/\mathfrak{n}|_{\mathrm{mod}3} \neq 0$.

In the CNT dispersion relation $\varepsilon(k)$, see Fig. 1.7, we distinguish between right- and left-moving branches for states with positive and negative wave vectors measured from the Dirac point, respectively. In *zigzag* and *zigzag-like* CNTs, the distance is measured by k with the corresponding sign and in *armchair* and *armchair-like* CNTs the distance is measured by κ.

CNT curvature

This straightforward analysis neglects effects due to the curvature of the nanotube. From tight-binding calculations it can be seen that the nonzero curvature causes a shift in the $\vec{k}$-plane [34]. More specifically, the allowed values of $k_\perp$ are shifted such that a finite gap opens in all nominally metallic CNTs except *armchair* CNTs. The size of the gap is given by [40]

$$E_{\text{gap}} = \frac{3ta_{\text{cc}}^2}{16R^2}\cos(3\theta) = \frac{\xi}{R^2}\cos(3\theta), \tag{1.11}$$

where $R = d/2$ is the nanotube radius and $\xi \simeq 1\,\text{eV}/\text{Å}^2$ can be used to estimate the size of the bandgap for a tight-binding hopping parameter $t = 2.6\,\text{eV}$ [40]. According to Eq. (1.11), values for the size of the bandgap range from zero for armchair CNTs to 60 meV for $(10,0)$ zigzag CNTs.[3]. Note, however, that typical single-wall CNTs have radii above 10 Å [42]. The model agrees with experimental observations [43]. More recently, larger bandgaps, up to 200 meV for the $(10,0)$ CNT are predicted within a non-orthogonal tight-binding model [44].

1.2.3 The single electron transport spectrum of a carbon nanotube quantum dot

When we want to observe quantum Coulomb blockade in a carbon nanotube quantum dot, we have to provide a lateral confinement such that the conditions in Tab. 1.1 are satisfied. In the CNT transport setup, a confinement of the quantum dot is naturally given by the metallic leads which act as electrochemical potential barriers. However, we still have to take care to satisfy $\hbar\Gamma < k_\text{B}T$. Depending on the material of the contacts and other fabrication parameters, it turns out that the tunnel coupling between the CNT and the leads can be too strong to observe Coulomb blockade [21]. These systems are better described in terms of ballistic electron wave-guides; a subject that we discuss in the second part of this work.

But not only the coupling between the nanotube and the electrode material is crucial. The coupling of the Fermi liquid reservoirs in the leads to the quantum dot on the carbon nanotube section between the contacts heavily depends on the electronic band structure that is modified by the gating potential. In Fig. 1.8 we plot current as a function of backgate voltage for a CNT suspended between two Rhenium contacts at a distance of 700 nm at $T = 300\,\text{mK}$. We can clearly observe distinct Coulomb blockade peaks for

---

[3] $R \simeq 4\,\text{Å}$ for a $(10,0)$ CNT, CNTs with $R < 4\,\text{Å}$ are not considered stable [41].

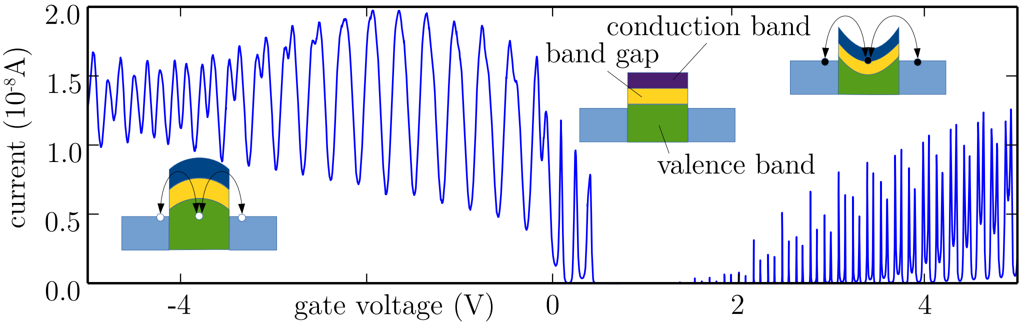

Figure 1.8: Current plotted as a function of gate voltage (gatetrace) for sample CB3224 recorded at $T = 300\,\mathrm{mK}$ and $V_\mathrm{b} = 50\,\mu\mathrm{V}$. On the left, for values $V_\mathrm{g} < 0.5\,\mathrm{V}$, we observe high currents and no Coulomb blockade. In this regime, no p-n-junction separates the quantum dot from the leads, as displayed by a schematic drawing in the left bottom corner. In the band-gap, no current can flow because the potential of the leads lies between valence and conduction band. On the right, for $V_\mathrm{g} > 1.5\,\mathrm{V}$, distinct peaks are a clear signature for Coulomb blockade behavior. The transmittance of the interfaces is decreased by a p-n-junction induced by the highly deformed bands on both sides of the quantum dot.

positive values of the gate voltage beyond the band gap. In this region, a p-n-junction separates the leads from the quantum dot, creating an effective tunnel barrier with high opacity. For higher values of the gate voltage, the effective barrier width decreases and the Coulomb blockade peaks are broadened. For hole conduction through the valence band on the side with negative gate voltage, we observe high current values without a signature of Coulomb blockade.

The lateral confinement due to the contacts or the p-n-junctions restricts the available $k_{||}$-bands, i.e., the continuous bands introduced in the previous section, to discrete levels, see Fig. 1.9(a), in the following called shells. In the fully degenerate case, a single shell can host up to four electrons with equal energy but different spin or $\vec{k}$ vector. In CNTs of the *zigzag* class, the states in the vicinity of the two Dirac points $\vec{K}$ and $\vec{K}'$ are distinguished by the “valley” quantum number $\tau = \pm 1$.

Kramers pairs At this point, all states in one shell are degenerate in energy, occupying the lowest lying states on the two Dirac cones in the vicinity of the $\vec{K}$ and $\vec{K}'$ points. When the time-reversal symmetry of the system is not broken, e.g., by a magnetic field, each state can be transformed into one of

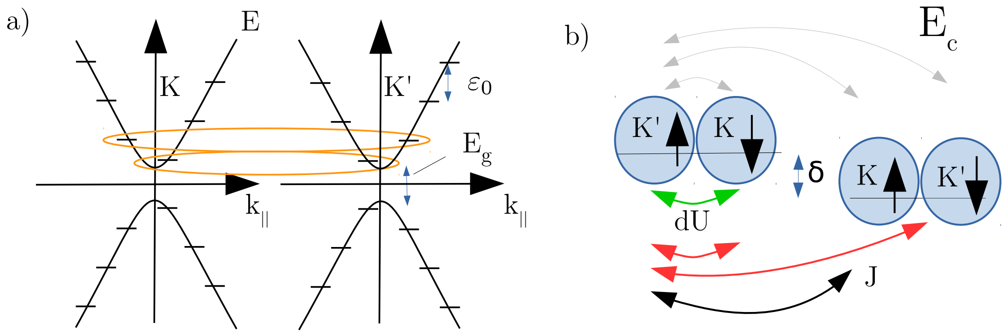

Figure 1.9: The quantum dot spectrum in the constant interaction model. (a) The dispersion relation of a carbon-nanotube with lifted degeneracy of the two Kramers pairs, due to, e.g., spin-orbit coupling. The longitudinal confinement imposes a restriction to discrete values of $k_{||}$. (b) Interaction of one electron (on the left) with the other electrons on the quantum dot on a mean-field level in the Oreg model. Thereby, J denotes the spin exchange interaction which has a different sign for parallel (black arrow) and anti-parallel spin (red arrows). dU denotes the interaction between electrons in the same spin-degenerate state (green arrow) and E_c is related to the inter-electronic Coulomb repulsion (grey arrows).

the other states by applying the time-reversal operation. The time-reversal operation flips the spin and the valley quantum numbers and thereby maps a state on its Kramers partner. Thus, the Kramers pairs in one CNT shell are given by $|K,\uparrow\rangle|K',\downarrow\rangle$ and $|K,\downarrow\rangle|K',\uparrow\rangle$.

Analysis in terms of the constant interaction model

A first analysis of traces obtained at low bias voltage by varying the gate potential (e.g., the data shown in Fig. 1.8) can be done in terms of a mean field description of the interaction on the quantum dot [45].

We are interested in the addition energy spectrum, i.e., the spectrum of energies $\Delta\mu_N = \mu(N) - \mu(N-1)$ at zero bias. In Eq. (1.2) we included the charging energy to account for the Coulomb repulsion between the electrons. In principle, a careful analysis of the multi-electron ground states even at a mean field level yields a multitude of parameters describing different interactions between the electrons on the CNT quantum dot, see Fig. 1.10(b). These include, e.g., the excess interaction between two electrons with opposite spin within one Kramers pair, dU, or the spin exchange interaction J [46, 47]. In the following we neglect the parameters dU and J, which are usually small compared to ε_0, see Ref. [48].

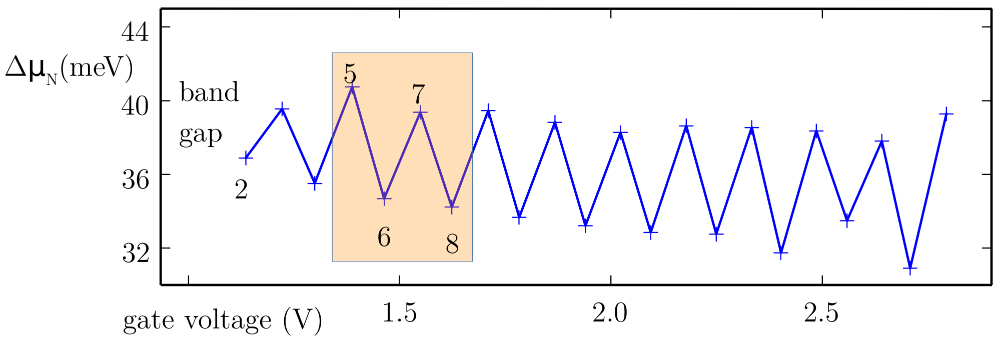

Figure 1.10: Addition energies as a function of gate voltage for the sample CB3224 extracted from the gatetrace in Fig. 1.8. The numbers close to the crosses denote the electron number on the dot. The second shell is highlighted. For this shell, the analysis in terms of the constant interaction model is performed.

The addition energies of the four electronic states in one shell n can then be written as [46, 47, 49]

$$\Delta\mu_{4n+1} = E_\mathrm{c} + \varepsilon_0 \tag{1.12}$$

$$\Delta\mu_{4n+3} = E_\mathrm{c} + \delta \tag{1.13}$$

$$\Delta\mu_{4(n+2)} = \Delta\mu_{4n+4} = E_\mathrm{c}, \tag{1.14}$$

where δ denotes an energy shift between the two Kramers pairs, see Fig. 1.9(a). This shift is introduced as a *subband mismatch* to fit experimental data, e.g., in Ref. [49]. More recent works strongly suggest that it can be identified with the spin-orbit coupling strength in CNTs [16]. From the gatetrace in Fig. 1.8 we can extract the addition energy spectrum and estimate the parameters.[4]

In Fig. 1.10 we plot the distance between two peaks in gate voltage, corrected by a gate conversion factor $\alpha = 0.46$ for sample CB3224. The first point in the plot corresponds to the energy required to add the second electron to the quantum dot. The addition energy for the first electron can not be resolved due to the band gap. Let us now focus on electron numbers $N = 5$ to $N = 8$. From the addition energies we extract the parameters of Eq. (1.12 - 1.14). We obtain $E_\mathrm{c} = 34\,\mathrm{meV}$, $\delta = 5\,\mathrm{meV}$ and $\varepsilon_0 = 11.5\,\mathrm{meV}$. The value for ε_0 corresponds to a lateral extension of the CNT quantum dot of 150 nm where we used $L = \pi\hbar v_\mathrm{F}/\varepsilon_0$ [31]. Compared to the distance between the contacts (700 nm), $L(\varepsilon_0)$ is considerably smaller. However, the lateral

---

[4] The values of the difference in gate voltage to add one electron have to be multiplied by the lever arm $\alpha = C_\mathrm{g}/C_\Sigma$.

quantum dot size can be reduced significantly by the p-n-junctions [50]. The value of the valley splitting δ is found to be rather large compared to previous observations [16]. Please note that this model is heavily simplified and the parameters of the constant interaction model can not be directly mapped to microscopic parameters of the CNT. From Fig. 1.10 it is evident that the addition energies and thus the parameters of the model are not equal for the five shells that are visible, contrarily to the model predictions.

Single particle state spectroscopy of the one-electron state

We focus on the quantum dot state with one electron on the dot. Thereby we are confident that the effects of electron-electron interaction are subleading and we can treat the system within a single-particle approach. As a spectroscopic tool we apply a magnetic field B_p along the nanotube axis. The field induces a magnetic flux through the tube cross-section which changes the component of the wavevector which is perpendicular to the CNT axis, $k_\perp$ [51]. This shifts the energy of the (discrete) states labeled by spin σ and valley τ by

$$E_{\sigma,\tau}(B) = \frac{1}{2} g_\mathrm{s} \mu_\mathrm{B} B_\mathrm{p} \sigma + g_\mathrm{orb} \mu_\mathrm{orb} B_\mathrm{p} \tau .$$

Adjusting the gate voltage to a value close to the first Coulomb peak to the right of the band gap, we can map the resonances that correspond to excited states within a finite bias voltage window,[5] see Fig. 1.11(a). When we tune the magnetic field, we trace out the evolution of the four possible single particle states in the first two shells, see Fig. 1.11(b).

We analyze the data[6] in this low-field ($B_{||} = 0 - 2\,\mathrm{T}$) regime using a linearized Hamiltonian in the spin and valley basis, i.e., $\{|K\uparrow\rangle$, $|K\downarrow\rangle$, $|K'\uparrow\rangle$

---

[5] The measurement was performed together with Daniel Schmid and published in his thesis, Ref. [52].

[6] The modeling that is presented in this section was performed by M. Marganska from the group of M. Grifoni. The results are published in Ref. [52]

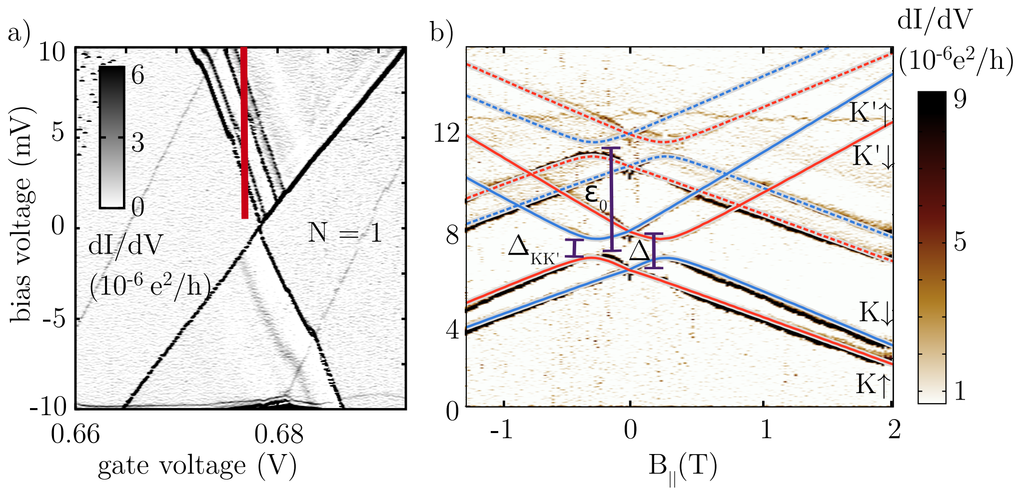

Figure 1.11: (a) Conductance as a function of bias and gate voltages in the vicinity of the first charging state ("diamond"). We can clearly observe the four lines corresponding to the two Kramers pairs of the first longitudinal quantization state (shell) and two Kramers pairs of the second shell. The lines are pointing towards the first charging state on the right. (b) Evolution of the Kramers pairs with an increasing magnetic field along the nanotube axis. Within each shell, the Kramers pairs at zero magnetic field are split by Δ (cf. δ in the Oreg model). The degeneracy of the constituents of the pairs is lifted with magnetic field as indicated by the labels on the right. The excited state energy is denoted by ε_0. Note that K and K' states show an anti-crossing at $V_g = \pm 0.2\,\mathrm{V}$ with an energy scale $\Delta_{KK'}$. Colored lines present a fit to Eq. (1.15).

$,|K' \downarrow\rangle\}$:

$$H_{\text{lin}} = \frac{1}{2} g_{\text{s}}\mu_{\text{B}}B_{||}\begin{pmatrix} 1 & 0 & 0 & 0 \\ 0 & -1 & 0 & 0 \\ 0 & 0 & 1 & 0 \\ 0 & 0 & 0 & -1 \end{pmatrix} + \frac{1}{2}\begin{pmatrix} \Delta_{\text{SO}} & 0 & \Delta_{\text{KK}'} & 0 \\ 0 & -\Delta_{\text{SO}} & 0 & \Delta_{\text{KK}'} \\ \Delta_{\text{KK}'} & 0 & -\Delta_{\text{SO}} & 0 \\ 0 & \Delta_{\text{KK}'} & 0 & \Delta_{\text{SO}} \end{pmatrix}$$
$$+ B_{||}g_{\text{orb}}\begin{pmatrix} \mu_{\text{orb}}^{\text{p}} & 0 & 0 & 0 \\ 0 & \mu_{\text{orb}}^{\text{ap}} & 0 & 0 \\ 0 & 0 & -\mu_{\text{orb}}^{\text{ap}} & 0 \\ 0 & 0 & 0 & -\mu_{\text{orb}}^{\text{p}} \end{pmatrix} + a|B_{||}|\begin{pmatrix} 1 & 0 & 0 & 0 \\ 0 & 1 & 0 & 0 \\ 0 & 0 & 1 & 0 \\ 0 & 0 & 0 & 1 \end{pmatrix} \tag{1.15}$$

We recognize the first and the third term as being the Zeeman and the Aharonov-Bohm type energy dependence. The magnetic moments associated with the Aharonov-Bohm interaction are different for the two Kramers pairs. The moment $\mu_{\text{orb}}^{\text{p}}$ is associated to the pair $|K \uparrow\rangle$, $|K' \downarrow\rangle$ and the moment $\mu_{\text{orb}}^{\text{ap}}$ to the pair $|K' \uparrow\rangle$, $|K \downarrow\rangle$. The second term in Eq. (1.15) contains the *spin-orbit* coupling Δ_{SO}, and $\Delta_{\text{KK}'}$, a mixing amplitude between the K and K' orbital. The former is a consequence of the nanotube geometry and can be obtained from a careful derivation of the full dispersion relation [53]. The latter can be attributed to disorder [54] or arise due to scattering at the ends of the nanotube in the armchair-like geometry class [37], while it is absent in the pure armchair CNTs where mode mixing is prohibited by the parity symmetry.[7] The origin of the last term in Eq. (1.15), which is proportional to a and to the modulus of the field is not clear. At the time of this writing, a is a fitting parameter in the ongoing analysis of the one-electron spectrum .

In Tab. 1.2 we show the parameters that correspond to the fit presented in Fig. 1.11(b) together with the parameters from the constant interaction model of the previous section. The two Kramers pairs are shifted apart by an energy $\Delta = \sqrt{\Delta_{\text{SO}}^2 + \Delta_{\text{KK}'}^2}$ at zero magnetic field, see Fig. 1.11(b). Δ can be compared to δ from the Oreg model. However, the two values deviate by one order of magnitude. Note that the shell spacing $\varepsilon_0 = 1.4\,\text{meV}$ extracted from the fit to the one electron spectroscopy data corresponds to an effective dot extension of $1.2\,\mu\text{m}$, almost two times larger than the distance between the contacts. In the vicinity of the band-gap, however, the finite curvature of the band reduces the energy spacing between two allowed values of $k_{||}$.

---

[7] This will be discussed in more detail in Ch. 3.

	shell 1	shell 2	CI
$\mu_{\mathrm{orb}}^{\mathrm{ap}}$	$0.89\,\mathrm{meV/T}$	$0.77\,\mathrm{meV/T}$	-
$\mu_{\mathrm{orb}}^{\mathrm{p}}$	$0.88\,\mathrm{meV/T}$	$0.69\,\mathrm{meV/T}$	-
a	$0.17\,\mathrm{meV/T}$	$0.05\,\mathrm{meV/T}$	-
Δ_{SO}	$0.48\,\mathrm{meV}$	$0.41\,\mathrm{meV}$	-
$\Delta_{\mathrm{KK'}}$	$0.28\,\mathrm{meV}$	$0.21\,\mathrm{meV}$	-
Δ/δ	$0.56\,\mathrm{meV}$	$0.46\,\mathrm{meV}$	$5\,\mathrm{meV}$
ε_2	$1.4\,\mathrm{meV}$		$11.5\,\mathrm{meV}$

Table 1.2: Parameters of the linearized Hamiltonian, Eq. (1.15), for the first two shells extracted from the one electron spectroscopy. The values are compared to the previous analysis in terms of the constant interaction model.

Chapter 2

Modeling a CNT quantum dot coupled to ferromagnetic leads

The considerations presented in the previous chapter are based on the assumption that the recorded transport data is solely determined by the energy spectrum of the quantum dot and the interaction of the electrons. The transport problem is treated as a sequence of single electron tunneling events with rates $\Gamma \ll k_{\mathrm{B}}T$ that are given by an effective, energy independent coupling between the CNT and the leads, and the temperature.

In the experimental data discussed in this section,[1] we observe a broadening of the Coulomb blockade peaks that can not be attributed to temperature. Further on, this broadening is sensitive to the magnetic properties of the contacts. To correctly interpret the data, we have to go beyond the sequential tunneling description and present a model where the coupling is still smaller, but of the order of the temperature, i.e., $\Gamma \leq k_{\mathrm{B}}T$. Approaching this regime we have to take into account charge fluctuations between the quantum dot and the leads. To this end, we apply a transport framework based on the Liouville-von-Neumann equation [55], incorporating the quantum mechanical nature of the problem and allowing us to go beyond the considerations of Sec. 1.1.

The Liouville-von-Neumann equation describes the time evolution of the density matrix of the quantum mechanical problem fully taking into account the system under consideration and its surroundings. In general, the system has less degrees of freedom than the environment and its time evolution can sometimes be calculated exactly when it is decoupled from the environment. Within the framework of the reduced density matrix theory we can start with

---

[1] The data has been recorded by Daniel Steininger and Andreas Prüfling from the University of Regensburg.

the exact solution for the decoupled system and perturb it by the coupling to the environment in a controlled way. Thereby we arrive at the *quantum master equation* (QME), which, in principle, describes the full dynamics of the weakly coupled system, see Ref. [56] for a review. The transport properties of the system are readily calculated from the QME. We follow the lines of Ref. [57] and present the so-called “dressed second order” (DSO) framework. Eventually we apply this framework to the problem of a carbon nanotube quantum dot coupled to ferromagnetic leads and compare the results to the experimental data. The results presented in this chapter have been published in Ref. [58].

Note that there are numerous other frameworks to approach this problem, e.g., the non-equilibrium Green’s function technique [17], the Wigner function method [59], the Kubo [60] and the Boltzmann equation approach [61] or the equation-of-motion technique [62]. An approach that reaches beyond the DSO with a different summation scheme is the “resonant tunneling approximation”(RTA) [63]. For a spinless single electron transistor the RTA exactly describes the density matrix and thus the current in the intermediate regime $\Gamma \leq k_{\mathrm{B}}T$. A comparison shows that the DSO predicts the same current as the RTA in this case and thus captures the relevant diagrammatic contributions [57]. For more complicated systems as is the CNT quantum dot the RTA is increasingly difficult to handle while the DSO can be applied to more complex systems straightforwardly.

2.1 Introduction to the reduced density matrix approach

In the following, we give a short introduction to the basic concepts of the reduced density matrix approach to quantum transport. The reader that is familiar with the construction of the quantum master equation for the reduced density matrix might as well skip the following section and continue with the introduction of the dressed second order approach in Sec. 2.2.

2.1.1 Statistical mixtures

The largest set of mutually commuting independent observables provides the maximum available information about a quantum mechanical system. A state Ψ specified solely by the eigenvalues of these observables is a pure state

$$\Psi = \sum_n a_n |\phi_n\rangle.$$

The choice of the set of observables is not unique. When the state of the system is not known, i.e., one can not provide a pure state, it is convenient to describe the system in terms of multiple possible states

$$|\Psi_n\rangle = \sum_{m'} a_{m'}^{(n)} |\phi_{m'}\rangle,$$

and define a density matrix

$$\hat{\rho} = \sum_n W_n |\Psi_n\rangle\langle\Psi_n|, \tag{2.1}$$

where W_n are real positive numbers and $\sum_n W_n = 1$. In the basis $\{|\phi\rangle\}$ the density operator takes the form

$$\hat{\rho} = \sum_{nmm'} W_n a_{m'}^{(n)} a_m^{(n)*} |\phi_{m'}\rangle\langle\phi_m|,$$

or equivalently, in terms of matrix components:

$$\langle\phi_i|\,\hat{\rho}\,|\phi_j\rangle = \sum_n W_n a_i^{(n)} a_j^{(n)*}. \tag{2.2}$$

The significance of this operator can be understood by the observation that the probability of finding the system in the state $|\Psi_n\rangle$ is W_n and that of selecting a certain eigenvector in this state, say $|\phi_m\rangle$, is $|a_m^{(n)}|^2$. The diagonal elements,

$$\hat{\rho}_{mm} = \sum_n W_n |a_m^{(n)}|^2,$$

denote thus the probability to find the system in the eigenstate $|\Psi_m\rangle$, summed over all possible basis states of the system. Analogously, the probability to find the system in the arbitrary state $|\Psi\rangle$ is given by

$$P(\Psi) = \sum_n W_n |\langle\Psi_n|\Psi\rangle|^2.$$

The expectation value of an observable $\hat{Q}$ can be calculated by tracing over the product with the density operator,

$$\langle Q\rangle = \mathrm{Tr}\{\rho Q\}. \tag{2.3}$$

This relation reflects the crucial capability of the density matrix. If we can predict the evolution of the density matrix, the expectation values of physical quantities can readily be calculated.

2.1.2 Time evolution of statistical mixtures

We define the time evolution operator $\hat{\mathrm{U}}$ via its action on the wave function

$$|\psi(t)\rangle = \hat{\mathrm{U}}(t, t_0)|\psi(t_0)\rangle, \tag{2.4}$$

and insert this expression in the Schrödinger equation,

$$\mathrm{i}\hbar\frac{\partial}{\partial t}\,\hat{\mathrm{U}}(t) = \hat{\mathrm{H}}(t)\,\hat{\mathrm{U}}(t), \tag{2.5}$$

where we omit $t_0 = 0$. According to Eq. (2.1) and Eq. (2.4), the time evolution of the density operator acquires the form

$$\hat{\rho}(t) = \hat{\mathrm{U}}(t)\,\hat{\rho}(0)\,\hat{\mathrm{U}}^{\dagger}(t). \tag{2.6}$$

Differentiating this equation with respect to time yields

$$\mathrm{i}\hbar\frac{\partial}{\partial t}\,\hat{\rho}(t) = [\hat{\mathrm{H}}(t), \hat{\rho}(t)]. \tag{2.7}$$

Note that the operators in this equation are written in the Schrödinger picture. It is often possible to decompose the Hamilton operator in a time independent part and a time-dependent perturbation,

$$\hat{\mathrm{H}} = \hat{\mathrm{H}}_0 + \hat{\mathrm{H}}_{\mathrm{p}}(t). \tag{2.8}$$

Now let $\hat{\mathrm{U}}_0$ be the time evolution operator that satisfies Eq. (2.5) where $\hat{\mathrm{H}}$ is replaced by $\hat{\mathrm{H}}_0$ and define

$$|\psi(t)\rangle = \hat{\mathrm{U}}_0(t)|\psi(t)\rangle_{\mathrm{I}}. \tag{2.9}$$

Furthermore let

$$\hat{\mathrm{U}}_{\mathrm{I}}(t) := \hat{\mathrm{U}}_0(t)^{\dagger}\,\hat{\mathrm{U}}(t) \tag{2.10}$$

and

$$\hat{\mathrm{H}}_{\mathrm{p,I}}(t) := \hat{\mathrm{U}}_0^{\dagger}(t)\,\hat{\mathrm{H}}_{\mathrm{p}}(t)\,\hat{\mathrm{U}}_0(t)$$

so that we can write

$$\mathrm{i}\hbar\frac{\partial}{\partial t}\,\hat{\mathrm{U}}_{\mathrm{I}}(t) = \hat{\mathrm{H}}_{\mathrm{p,I}}(t)\,\hat{\mathrm{U}}_{\mathrm{I}}(t). \tag{2.11}$$

We can now combine Eq. (2.1), Eq. (2.9) and Eq. (2.10) to arrive at the Liouville equation in the interaction picture, i.e.,

$$\mathrm{i}\hbar\frac{\partial}{\partial t}\,\hat{\rho}_{\mathrm{I}}(t) = [H_{\mathrm{p,I}}(t), \hat{\rho}_{\mathrm{I}}(t)]. \tag{2.12}$$

We integrate over time on both sides of this equation,

$$\hat{\rho}_{\mathrm{I}}(t) = \rho_{\mathrm{I}}(0) - \int_0^t \mathrm{d}t' \, \frac{\mathrm{i}}{\hbar}[\hat{\mathrm{H}}_{\mathrm{p,I}}(t'), \hat{\rho}_{\mathrm{I}}(t')], \tag{2.13}$$

and insert the expression back in Eq. (2.12). Repeating these steps we obtain a recursive, non-perturbative expansion for $\hat{\rho}_{\mathrm{I}}(t)$.

2.1.3 The reduced density matrix

We consider two interacting quantum mechanical systems. One system, say S, is of special interest and we label the eigenstates of the system $|s_i\rangle$ and the states of the other system, E, $|e_i\rangle$. We will refer to S as the *system* and to E as the *environment* or *reservoir* in the following. We calculate the expectation value of an operator $\hat{Q}$ acting solely on S according to Eq. (2.3),

$$\langle \hat{Q} \rangle = \mathrm{Tr}\{\hat{\rho}(t)\hat{Q}\} = \sum_{ij} \left[\sum_k \langle e_k s_j | \, \hat{\rho}(t) | e_k s_i \rangle \right] \langle s_i | \hat{Q} | s_j \rangle. \tag{2.14}$$

We introduce the *reduced density matrix (RDM)*,

$$\hat{\rho}_{\mathrm{red}} \equiv \mathrm{Tr}_E\{\hat{\rho}\} := \sum_k \langle e_k | \, \hat{\rho}(t) | e_k \rangle, \tag{2.15}$$

to rewrite Eq. (2.14),

$$\langle Q \rangle = \mathrm{Tr}_S\{\hat{\rho}_{\mathrm{red}} \, \hat{Q}\}. \tag{2.16}$$

To this point, no approximation has been made; Eq. (2.14) is still exact. However, the direction is clear: We separate the part of the (whole) system where the trace in Eq. (2.15) can be calculated more easily. As soon as we are working with the RDM to describe S, we loose all information on the correlations in the environment E and we call S an *open system*. The time evolution of an open system can not be described by a Liouville equation. We perform the trace over the states in the environment on the Liouville equation, Eq. (2.12), and obtain

$$\mathrm{i}\hbar \frac{\partial}{\partial t} \, \hat{\rho}_{\mathrm{red}} = \mathrm{Tr}_E\{[\hat{\mathrm{H}}, \hat{\rho}(t)]\}. \tag{2.17}$$

Suppose the system S was originally separated from the reservoir E and we switch on interaction between S and E at time $t = 0$. We suppose that a decomposition according to Eq. (2.8) exists. Then the boundary condition to Eq. (2.17) can be stated as

$$\hat{\rho}(0) = \hat{\rho}_S(0) \otimes \hat{\rho}_E(0).$$

If the reservoir E is large compared to the size of the system in terms of volume and particle number, the interaction with the system will not change E measurably. Let E be a large reservoir in thermal equilibrium at $t = 0$. Then it follows that E can be described by a time-independent density matrix.

We proceed by integrating Eq. (2.17) and reinserting the result,

$$\dot{\hat{\rho}}_{\mathrm{red}}(t) = -\mathrm{i}\,\mathrm{Tr}_E\left\{\hat{\mathcal{L}}(t)\,\hat{\rho}_S(0)\otimes\hat{\rho}_E\right\} - \int\limits_0^t \mathrm{d}t'\,\mathrm{Tr}_E\left\{\hat{\mathcal{L}}(t)\,\hat{\mathcal{L}}(t')\,\hat{\rho}_{\mathrm{I}}(t')\right\}, \quad (2.18)$$

where we introduce the Liouville operator,

$$\hat{\mathcal{L}}(t)\hat{X} = \frac{1}{\hbar}\left[\hat{\mathrm{H}}_{\mathrm{p}}(t), \hat{X}\right].$$

Eq. (2.18) is a simplified form of the *Nakajima-Zwanzig* equation exact to all orders in $\hat{\mathrm{H}}_{\mathrm{p}}$ [64].

Second order expansion

With the assumptions from the previous section the density matrix at $t \neq 0$ in the interaction picture simplifies to

$$\hat{\rho}_{\mathrm{I}}(t) = \hat{\rho}_{\mathrm{red,I}}(t) \otimes \hat{\rho}_E\,. \quad (2.19)$$

We further specify the perturbation $\hat{\mathrm{H}}_{\mathrm{p}}$ to be a bilinear form in the operators acting on S and E, i.e.,

$$\hat{\mathrm{H}}_{\mathrm{p}} \equiv \hat{\mathrm{H}}_{\mathrm{T}} = \sum_{i,p} \hat{\mathrm{S}}_i^p \hat{\mathrm{E}}_i^{\bar{p}}$$

where we used the label T to refer to the associated tunneling process between system and bath. The index $p \in \{+,-\}$ refers to an addition or removal of a particle to or from the system or bath respectively. We rewrite this operator in the interaction picture,

$$\begin{aligned}\hat{\mathrm{H}}_{\mathrm{T,I}}(t) = \hat{\mathrm{U}}_0^\dagger(t)\,\hat{\mathrm{H}}_{\mathrm{T}}\,\hat{\mathrm{U}}_0(t) &= \sum_{ip} \hat{\mathrm{U}}_S^\dagger(t)\hat{\mathrm{S}}_i^p\,\hat{\mathrm{U}}_S(t)\,\hat{\mathrm{U}}_E^\dagger(t)\hat{\mathrm{E}}_i^{\bar{p}}\,\hat{\mathrm{U}}_E(t)\\ &= \sum_{i,p} \hat{\mathrm{S}}_i^p(t)\hat{\mathrm{E}}_i^{\bar{p}}(t),\end{aligned}$$

and insert this expression together with Eq. (2.19) into Eq. (2.18). We end up with a second order expansion of Eq. (2.18) in $\hat{\mathrm{H}}_{\mathrm{T,I}}$,

$$\begin{aligned}\dot{\hat{\rho}}_{\mathrm{red,I}} = -\sum_{ij,p} \frac{1}{\hbar^2} \int_0^t \mathrm{d}t' \Big\{ &[\hat{\mathrm{S}}_i^p(t), \hat{\mathrm{S}}_j^{\bar{p}}(t')\, \hat{\rho}_{\mathrm{red}}(t')] \Big\langle\, \hat{\mathrm{E}}_i^{\bar{p}}(t)\, \hat{\mathrm{E}}_j^p(t') \Big\rangle_E \\ &- [\hat{\mathrm{S}}_i^{\bar{p}}(t), \hat{\rho}_{\mathrm{red}}(t')\, \hat{\mathrm{S}}_j^p(t')] \Big\langle\, \hat{\mathrm{E}}_j^p(t')\, \hat{\mathrm{E}}_i^{\bar{p}}(t) \Big\rangle_E \Big\}, \qquad (2.20)\end{aligned}$$

where we used the notation $\langle ... \rangle_A = \mathrm{Tr}_A\{ ...\, \hat{\rho}_A \}$ and omitted the label for the interaction picture on the right side. We will henceforth do so whenever the context clearly specifies the picture. Note that the first term in the expansion vanished under the trace. As a consequence of the thermal equilibrium property of the reservoir we can write

$$[\hat{\mathrm{U}}_E(t), \hat{\rho}_E] = 0, \qquad (2.21)$$

from which we obtain

$$\Big\langle\, \hat{\mathrm{E}}_i^p(t')\, \hat{\mathrm{E}}_j^{\bar{p}}(t) \Big\rangle_E = \Big\langle\, \hat{\mathrm{E}}_i^p(t-t')\, \hat{\mathrm{E}}_j^{\bar{p}} \,\Big\rangle_E .$$

The correlations in a reservoir at thermal equilibrium thus decay independently of the history of the reservoir.

Remark: The integro-differential Eq. (2.18) can be rewritten in terms of a superoperator $\mathcal{K}^{(2n)}$ including terms of order $2n$ in H_{T}. For example at lowest order it reduces to

$$\dot{\hat{\rho}}_{\mathrm{red,I}}(t) = \frac{1}{\hbar^2} \int_0^t \mathrm{d}t'\, \mathcal{K}_{\mathrm{I}}^{(2)}(t,t')\, \hat{\rho}_{\mathrm{red,I}}(t'). \qquad (2.22)$$

where by comparison with Eq. (2.20) we obtain

$$\begin{aligned}\mathcal{K}_{\mathrm{I}}^{(2)}(t,t') \ldots = \sum_{ij,p} \Big\{ &[\hat{\mathrm{S}}_{i,\mathrm{I}}^p(t), \hat{\mathrm{S}}_{j,\mathrm{I}}^{\bar{p}}(t') \ldots] \Big\langle\, \hat{\mathrm{E}}_{i,\mathrm{I}}^{\bar{p}}(t-t')\, \hat{\mathrm{E}}_{j,\mathrm{I}}^p \,\Big\rangle_E \\ &- [\hat{\mathrm{S}}_{i,\mathrm{I}}^{\bar{p}}(t), \ldots \hat{\mathrm{S}}_{j,\mathrm{I}}^p(t')] \Big\langle\, \hat{\mathrm{E}}_{j,\mathrm{I}}^p(t-t')\, \hat{\mathrm{E}}_{i,\mathrm{I}}^{\bar{p}} \,\Big\rangle_E \Big\}. \qquad (2.23)\end{aligned}$$

In Eq. (2.22) and Eq. (2.23) we put the label for the interaction picture as an explicit reminder.

Diagrammatics In perturbative expansions such as Eq. (2.20) it is often convenient to introduce a diagrammatic representation of the expressions in the series. From the diagrammatic representation the analytical expression for the elements of the density matrix can be readily compiled. To demonstrate this technique, we present Eq. (2.20) in a matrix element form, i.e.,

$$\begin{aligned}\langle b|\,\dot{\hat{\rho}}_{\mathrm{red}}\,|b'\rangle = &-\sum_{ij,p}\frac{1}{\hbar^2}\sum_{aa'}\\ &\times\int_0^t \mathrm{d}t'\,\Big\{\langle b|\,\hat{\mathrm{S}}_i^p(t)\,\hat{\mathrm{S}}_j^{\bar{p}}(t')|a\rangle\langle a|\,\hat{\rho}_{\mathrm{red}}(t')|a'\rangle\langle a'|b'\rangle\Big\langle\,\hat{\mathrm{E}}_i^{\bar{p}}(t-t')\,\hat{\mathrm{E}}_j^p\,\Big\rangle_E\\ &\qquad-\langle b|\,\hat{\mathrm{S}}_j^{\bar{p}}(t')|a\rangle\langle a|\,\hat{\rho}_{\mathrm{red}}(t')|a'\rangle\langle a'|\,\hat{\mathrm{S}}_i^p(t)|b'\rangle\Big\langle\,\hat{\mathrm{E}}_i^{\bar{p}}(t-t')\,\hat{\mathrm{E}}_j^p\,\Big\rangle_E\\ &\qquad-\langle b|\,\hat{\mathrm{S}}_i^p(t)|a\rangle\langle a|\,\hat{\rho}_{\mathrm{red}}(t')|a'\rangle\langle a'|\,\hat{\mathrm{S}}_j^{\bar{p}}(t')|b'\rangle\Big\langle\,\hat{\mathrm{E}}_j^p(t-t')\,\hat{\mathrm{E}}_i^{\bar{p}}\,\Big\rangle_E\\ &\qquad+\langle b|a\rangle\langle a|\,\hat{\rho}_{\mathrm{red}}(t')|a'\rangle\langle a'|\,\hat{\mathrm{S}}_j^{\bar{p}}(t')\,\hat{\mathrm{S}}_i^p(t)|b'\rangle\Big\langle\,\hat{\mathrm{E}}_j^p(t-t')\,\hat{\mathrm{E}}_i^{\bar{p}}\,\Big\rangle_E\Big\}.\end{aligned} \tag{2.24}$$

The rules for the construction of the diagrams out of the perturbative expansion are enumerated below.

1. Each diagram consists of an upper and lower contour representing the evolution of states $a \to b$ and $b' \to a'$ (compare Eq. (2.24)), respectively.

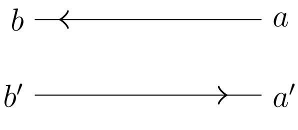

2. Throughout all diagrams, time evolves from right to left. a and a' are initial states, b and b' are final states.

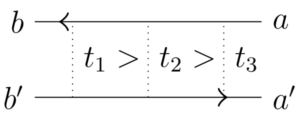

3. Every operator acting on the system standing to the left of the RDM creates a vertex at a given time on the upper contour. Every operator on the right creates a vertex on the lower contour. At each vertex the particle number on the dot changes by ±1.

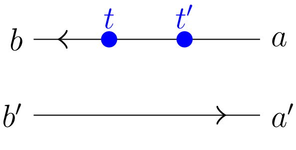

$\hat{\mathrm{S}}_i^p(t)\,\hat{\mathrm{S}}_j^{\bar{p}}(t')\,\hat{\rho}_{\mathrm{red}}(t')$

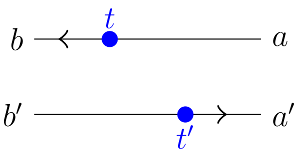

$\hat{\mathrm{S}}_i^p(t)\,\hat{\rho}_{\mathrm{red}}(t')\,\hat{\mathrm{S}}_j^{\bar{p}}(t')$

4. The vertices of two dot operators which are related via two reservoir operators, $\hat{\mathrm{E}}_j$, have to be connected by a fermion line.

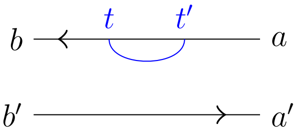

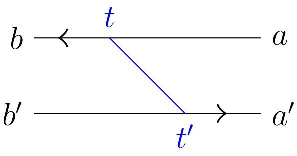

5. The fermion line points toward the vertex representing the operator creating an electron on the dot, $\hat{\mathrm{S}}^+$ (specified by the index $p = \pm$, in the example below $p = -$).

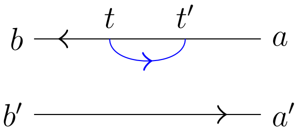

$\hat{\mathrm{S}}_i^p(t)\,\hat{\mathrm{S}}_j^{\bar{p}}(t')\,\hat{\rho}_{\mathrm{red}}(t')\big\langle\hat{\mathrm{E}}_i^{\bar{p}}(t)\,\hat{\mathrm{E}}_j^p(t')\big\rangle$

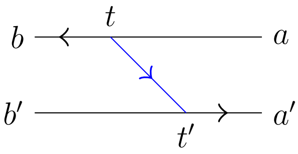

$\hat{\mathrm{S}}_i^p(t)\,\hat{\rho}_{\mathrm{red}}(t')\,\hat{\mathrm{S}}_j^{\bar{p}}(t')\big\langle\hat{\mathrm{E}}_j^p(t')\,\hat{\mathrm{E}}_i^{\bar{p}}(t)\big\rangle$

Note that the hermitian conjugation of a diagram is equivalent to flipping the diagram with respect to the horizontal axis plus inverting the arrows on the contours and the fermion line. Before we specify p or consider the hermitian conjugate of a diagram, i.e., in Num. 4, the diagram can be used as a placeholder for all diagrams that can be constructed out of it. All second order diagrams can be constructed from the two "generic" diagrams in Num. 4.

For the next steps, we require a time-convolutive form of the right-hand side in Eq. (2.22). This form is obtained by a transformation to the Schrödinger picture, shown in the supplement, Sec. 2.A. We obtain

$$\lim_{t\to\infty}\dot{\hat{\rho}}_{\mathrm{red,S}}(t) = -\frac{\mathrm{i}}{\hbar}[\hat{\mathrm{H}}_S, \hat{\rho}_{\mathrm{red,S}}(\infty)] - \lim_{t\to\infty}\int_0^t \mathrm{d}t'\,\mathcal{K}_{\mathrm{S}}(t')\,\hat{\rho}_{\mathrm{red,S}}(t-t'). \tag{2.25}$$

Eigenbasis of the system: Let us express Eq. (2.25) in the eigenbasis of the system. We know from the definition of the interaction picture how the operators in the bath evolve in time, namely

$$\frac{\partial}{\partial t}\,\hat{\mathrm{E}}_i^p(t) = \frac{\mathrm{i}}{\hbar}[\hat{\mathrm{H}}_0, \hat{\mathrm{E}}_i^p(t)]. \tag{2.26}$$

When the particle number is conserved by the reservoir, i.e., only pairs $\hat{\mathrm{E}}_j^p\,\hat{\mathrm{E}}_i^{\bar{p}}$ or their hermitian conjugates appear in $\hat{\mathrm{H}}_E$, and no dissipation occurs, we arrive at

$$\frac{\partial}{\partial t}\,\hat{\mathrm{E}}_i^p(t) = \frac{\mathrm{i}}{\hbar}p\epsilon_i\,\hat{\mathrm{E}}_i^p(t),$$

where ϵ_i is defined with respect to Eq. (2.26). Next we have to evaluate the elements of the integrand in Eq. (2.25) (cf. Eq. (2.63) in the appendix) in the basis of the energy eigenstates of the system. The time evolution operator $\hat{\mathrm{U}}_0$ in the energy basis is given by

$$\langle m|\,\hat{\mathrm{U}}_0(t)\Big|n\rangle = \delta_{mn}\mathrm{e}^{-\frac{\mathrm{i}}{\hbar}E_n t/\hbar}.$$

where E_n denotes the energy eigenvalue of $|n\rangle$. The matrix elements of the time derivative of the reduced density matrix are thus

$$\begin{aligned}\Big(\dot{\hat{\rho}}_{\mathrm{red,S}}(s)\Big)_{mn} = {} & -\frac{\mathrm{i}}{\hbar}[\hat{\mathrm{H}}_S, \hat{\rho}_{\mathrm{red,S}}(t)]_{mn} - \frac{1}{\hbar^2}\sum_{kl,ij,p} \\ & \int_0^t \mathrm{d}t' \Big\{ \Big(\hat{\mathrm{S}}_{i,\mathrm{S}}^p\Big)_{mk}\Big(\hat{\mathrm{S}}_{j,\mathrm{S}}^{\bar{p}}\Big)_{kl}\Big(\hat{\rho}_{\mathrm{red,S}}(t-t')\Big)_{ln}\langle\hat{\mathrm{E}}_i^{\bar{p}}\,\hat{\mathrm{E}}_j^p\,\mathrm{e}^{-\frac{\mathrm{i}}{\hbar}(E_{kn}-\bar{p}\epsilon_i)t'}\rangle \\ & + \Big(\hat{\mathrm{S}}_{j,\mathrm{S}}^p\Big)_{mk}\Big(\hat{\rho}_{\mathrm{red,S}}(t-t')\Big)_{kl}\Big(\hat{\mathrm{S}}_{i,\mathrm{S}}^{\bar{p}}\Big)_{ln}\langle\hat{\mathrm{E}}_i^{\bar{p}}\,\hat{\mathrm{E}}_j^p\,\mathrm{e}^{-\frac{\mathrm{i}}{\hbar}(E_{ml}-\bar{p}\epsilon_i)t'}\rangle \\ & + \Big(\hat{\mathrm{S}}_{i,\mathrm{S}}^p\Big)_{mk}\Big(\hat{\rho}_{\mathrm{red,S}}(t-t')\Big)_{kl}\Big(\hat{\mathrm{S}}_{j,\mathrm{S}}^{\bar{p}}\Big)_{ln}\langle\hat{\mathrm{E}}_j^{\bar{p}}\,\hat{\mathrm{E}}_i^p\,\mathrm{e}^{-\frac{\mathrm{i}}{\hbar}(E_{kn}-p\epsilon_i)t'}\rangle \\ & - \Big(\hat{\rho}_{\mathrm{red,S}}(t-t')\Big)_{mk}\Big(\hat{\mathrm{S}}_{j,\mathrm{S}}^p\Big)_{kl}\Big(\hat{\mathrm{S}}_{i,\mathrm{S}}^{\bar{p}}\Big)_{ln}\langle\hat{\mathrm{E}}_j^{\bar{p}}\,\hat{\mathrm{E}}_i^p\,\mathrm{e}^{-\frac{\mathrm{i}}{\hbar}(E_{ml}-p\epsilon_i)t'}\rangle. \end{aligned} \tag{2.27}$$

This representation will be useful when we calculate the Laplace transform.

The stationary limit

We are interested only in the stationary limit of the time evolution to derive the transport features of our system. In order to proceed, we assume that the stationary limit exists in the *first* place, i.e.,

$$\lim_{t\to\infty}\hat{\rho}_{\mathrm{red}}(t) \overset{\mathrm{(I)}}{=} \hat{\rho}_{\mathrm{red}}(\infty) \overset{\mathrm{(II)}}{=} \lim_{\lambda\to 0^+}\lambda\mathcal{L}\{\hat{\rho}_{\mathrm{red}}(t)\}, \tag{2.28}$$

where $\mathcal{L}\{f(t)\}$ denotes the Laplace transform of $f(t)$ and should not be confused with the Liouville operator $\hat{\mathcal{L}}$. The validity of the stationary limit, (I), is ensured by the coupling to the thermal equilibrium bath. We can be confident that the correlations in the bath vanish in the long time limit [65],

$$\lim_{t\to\infty}\langle \hat{\mathrm{E}}_i^{\bar{p}}(t)\,\hat{\mathrm{E}}_j^{p}\rangle = \lim_{t\to\infty}\langle \hat{\mathrm{E}}_i^{\bar{p}}\,\hat{\mathrm{E}}_j^{p}\,\mathrm{e}^{-\frac{\mathrm{i}}{\hbar}(E_{ml}-\bar{p}\epsilon_i)t}\rangle = 0,$$

in the Kernel, Eq. (2.23). Technically this can be ensured by adding an infinitesimal imaginary part to the energy difference. This part reflects the finite lifetime of the electronic states due to all relevant interaction mechanisms [66]. (I) is the prerequisite to equality (II) in Eq. (2.28) which is known as the final value theorem.

We are now in the position to perform the Laplace transform of the integral on the right in Eq. (2.25),

$$\begin{aligned}\lim_{t\to\infty}\int_0^t \mathrm{d}t'\,\mathcal{K}_\mathrm{S}(t')\,\hat{\rho}_{\mathrm{red,S}}(t-t') &= \lim_{\lambda\to 0^+}\lambda\mathcal{L}\{\mathcal{K}_\mathrm{S}\}(\lambda)\mathcal{L}\{\hat{\rho}_{\mathrm{red,S}}\}(\lambda)\\ &= \lim_{\lambda\to 0^+}\mathcal{L}\{\mathcal{K}_\mathrm{S}\}(\lambda)\,\hat{\rho}_{\mathrm{red,S}}(\infty).\end{aligned} \tag{2.29}$$

Here, we used the final value theorem twice. Note that the Laplace transform can also be performed as a first step, the limits $t\to\infty$ and $\lambda\to 0^+$ are formally equivalent.

Eventually, after we performed the steady state limit and substituted it by the limit $\lambda\to 0^+$ in front of the Laplace transform of the Kernel we obtain

$$\dot{\hat{\rho}}_{\mathrm{red}}(\infty) = -\frac{\mathrm{i}}{\hbar}[\hat{\mathrm{H}}_S, \hat{\rho}_{\mathrm{red}}(\infty)] + \lim_{\lambda\to 0^+}\int_0^\infty \mathrm{d}t'\,\mathrm{e}^{-\lambda t'}\mathcal{K}(t')\,\hat{\rho}_{\mathrm{red}}(\infty). \tag{2.30}$$

This is a stationary form of the *Redfield equation* [67]. After we switched on the interaction between the system and the bath, the time evolution of the system eventually does not depend on its previous state anymore. This is a consequence of the bath being unaffected by the coupling to the system ($\hat{\rho}_\mathrm{E}$ satisfying Eq. (2.21)) and the requirement that the steady state limit exists. Note that, under theses assumptions, Eq. (2.30) is exact. Contrarily, the derivation of the *time-local* Redfield equation from the full Nakajima-Zwanzig equation, Eq. (2.18), requires the *Born-Markov approximation* [68].

2.1.4 The Laplace transform of the Kernel

With all previous ingredients we can readily perform the integral over t' which can be identified as the Laplace transform of the superoperator $\mathcal{K}$. The integral of, e.g., the second term in Eq. (2.27) thus evaluates to

$$\lim_{\lambda\to 0^+} \mathrm{Tr}_E\left\{ \int\limits_0^\infty \mathrm{d}t'\ \hat{\mathrm{E}}_i^{\bar{p}}\,\hat{\mathrm{E}}_j^{p}\,\mathrm{e}^{-\frac{\mathrm{i}}{\hbar}(E_{kn}-\bar{p}\epsilon_i-\mathrm{i}\lambda)t'} \right\} = \mathrm{i}\hbar \lim_{\lambda\to 0^+} \mathrm{Tr}_E\left\{ \frac{\hat{\mathrm{E}}_i^{\bar{p}}\,\hat{\mathrm{E}}_j^{p}}{E_{nk}+\bar{p}\epsilon_i-\mathrm{i}\lambda} \right\}. \tag{2.31}$$

It is convenient to label the elements of the kernel $\mathcal{K}$ by the transition the element is related to. Suppose there is a transition from states $a, a' \to b, b'$. We then select the matrix element $\langle a|\,\hat{\rho}_{\mathrm{red}}\,|a'\rangle$ and use the superoperator $\mathcal{K}$ to project the element on the states b, b':

$$\begin{aligned}\lim_{t\to\infty}\Big(\dot{\hat{\rho}}_{\mathrm{red}}(t)\Big)_{bb'} &= -\frac{\mathrm{i}}{\hbar}\sum_{a,a'}\delta_{ab}\delta_{a'b'}\Big(\hat{\rho}_{\mathrm{red}}\Big)_{aa'}(E_a-E_{a'}) + \sum_{aa'}\mathcal{K}_{bb'}^{aa'}\Big(\hat{\rho}_{\mathrm{red}}\Big)_{aa'}\\ &= 0,\end{aligned} \tag{2.32}$$

where

$$\mathcal{K}_{bb'}^{aa'} := \langle b|\mathcal{K}\Big[|a\rangle\langle a'|\Big]|b'\rangle.$$

Eq. (2.32) is referred to as the *Lindblad form* of the quantum master equation. The first term on the right in Eq. (2.32) is non-zero for off-diagonal elements of the RDM that are non-degenerate. We clearly see from Eq. (2.32) that these so-called *secular* components have to vanish in the steady-state limit. In other words, if a model includes secular components, a description in terms of a steady-state RDM is not suitable.

The single elements of the kernel that relate the entries of the density matrix are called the *rates*,

$$K_{bb}^{aa} = \sum_l \Gamma_{l,ba}^{p},$$

where $p = \pm$ depends on whether $|a\rangle \to |b\rangle$ denotes an in- or an out-tunneling process, respectively. We recall that the diagonal elements of the density matrix $\hat{\rho}_{\mathrm{red}}$ are subject to normalization,

$$\sum_a \Big(\hat{\rho}_{\mathrm{red}}\Big)_{aa} = 1,$$

from which it follows that the kernel $\mathcal{K}$ obeys

$$\sum_a \mathcal{K}_{bb}^{aa} = 0. \tag{2.33}$$

We will refer to this statement later as the *current conserving* property of the kernel.

The role of coherences Coherences are off-diagonal elements of the density matrix. They describe quantum mechanical oscillations between states that differ by quantum numbers that are *not conserved* within the *full* Hamiltonian. Here, i.e., in the derivation of Eq. (2.32), we assume that the particle number is conserved in the whole system. As a consequence, coherences that relate states with different occupation numbers N are 0. The density matrix thus acquires a block-diagonal form and within each block, N is the same [69]. On the other hand, if we are interested in spin transport through a quantum dot attached to magnetized leads while allowing for spin-flip processes on the quantum dot, coherences can occur between states with the same N but with different spin [70].

We distinguish between coherences that relate states which are degenerate in energy, called *non-secular* components, and coherences that relate states with different energies – the *secular* components mentioned above. In Eq. (2.32), we dropped the secular components in the steady state limit. Non-secular components, on the other hand, have to be treated with care as they can affect transport properties considerably also in the steady state limit [70]. In the problem discussed in this thesis, all quantum numbers are assumed to be conserved within the whole system and no coherences are needed.

A Pauli-like master equation If we can neglect coherences, the QME is reduced to a fully diagonal operator in the occupation number basis,

$$0 = \sum_{aa} \mathcal{K}_{bb}^{aa} \left(\hat{\rho}_{\text{red}} \right)_{aa}, \tag{2.34}$$

resembling the *Pauli master equation* [68], but with rates that are, in general, defined to all orders in the coupling to the reservoirs. This equation is the starting point for the calculations in the main part, Sec. 2.2.

2.1.5 Electronic transport

We are interested in the transport properties of the system. The most prominent characteristic is the current through the system. We define the current as the time derivative of the electron number in one of the leads in the interaction picture,

$$\hat{\mathrm{I}}_l = -\mathrm{i}\frac{e}{\hbar}\left[\hat{\mathrm{H}}_{\mathrm{T},l}, \hat{\mathrm{N}}_l \right],$$

and calculate the average of this operator by tracing over the product with the reduced density matrix as shown in Eq. (2.14). We end up with the following expression for the current,

$$I_l(t) = \mathrm{Tr}_\mathrm{S}\left\{ \int_0^t \mathrm{d}t'\, \mathcal{K}_{I_l}(t-t')\, \hat{\rho}_\mathrm{red}(t') \right\}, \tag{2.35}$$

where $\mathcal{K}_{I_l}$ is the current kernel for lead l. In general, the order of this expression in the coupling to the leads is determined by the order of $\hat{\rho}_\mathrm{red}$, i.e., an expression obtained from the exact representation in Eq. (2.18) by limiting the number of recursions. The current to second order in the tunneling Hamiltonian can be expressed as

$$I_l(t) = -e\mathrm{i}\, \mathrm{Tr}_S \left\{ \int_0^t \mathrm{d}\tau\, \mathrm{Tr}_E \left\{ \hat{\mathrm{I}}_l(t)\, \mathcal{L}_l(\tau)\, \hat{\rho}_\mathrm{red}(\tau)\, \hat{\rho}_E \right\} \right\}. \tag{2.36}$$

We employ the diagrammatic language from the previous section to write down the Laplace transform of the current kernel, i.e.,

$$\lim_{t\to\infty} I_l(t) = \sum_{aa'} \sum_{b} \left(\mathcal{K}_l^\mathrm{c} \right)_{bb}^{aa'} (\hat{\rho}_\mathrm{red})_{aa'}. \tag{2.37}$$

The kernel $\mathcal{K}_l^\mathrm{c}$ contains a subset of diagrams from $\mathcal{K}$. When we can neglect coherences, the current can be written in terms of rates $\Gamma_{ba,l}^{c}$,

$$I_l(V_\mathrm{b}, V_\mathrm{g}) = \sum_N \sum_{a,c\in C_a^+} \left[P_a(V_\mathrm{b}, V_\mathrm{g}) \Gamma_{ca,l}^{+}(V_\mathrm{b}, V_\mathrm{g}) - P_c(V_\mathrm{b}, V_\mathrm{g}) \Gamma_{ac,l}^{-}(V_\mathrm{b}, V_\mathrm{g}) \right], \tag{2.38}$$

where the sum over a includes all states with N particles, C_a^+ is the set of states that can be reached by in-tunneling from state a and $P_a = (\hat{\rho}_\mathrm{red})_{aa}$ are the diagonal elements of the density matrix. Note that the current kernel contains only operators from *one* specific lead l. Without coherences, the kernel is constructed from rates $\Gamma_{l,ba}^{p}$, used also in the density matrix kernel, and from the diagonal elements of the density matrix, the populations. We can therefore calculate the current directly from the solution of the Pauli-like master equation.

2.1.6 Remarks on the reduced density matrix approach

We started with the Hamiltonian operator of a system coupled to one or multiple baths. We then calculated the time-evolution of the reduced density matrix of the system perturbatively to the second (and first non-trivial) order in the coupling to the bath. At this stage, the perturbative series is comfortably represented in a diagrammatic language. Eventually we perform a Laplace transform on the expression for the time derivative of the density matrix. For the sake of clarity, this is done manually. In the next section we will show how the expression for the rates can be obtained directly from the *diagrammatic* expansion.

In the derivation of the quantum master equation, we require that all parts of the Hamiltonian conserve the particle number. This is a choice that allows us to discriminate states by their occupation, the *populations*. Furthermore, we are only interested in the stationary regime. This implies that the reservoir is in a stationary thermal equilibrium. We replaced the limit $t \to \infty$ by the limit $\lambda \to 0^+$ for the Laplace transformed version of the Kernel. To be consistent, the limit $\eta \to 0$, performed as a last step in the calculations, must not change the results. When we apply the framework to a model, we have to check if *secular* components drop in the construction of the RDM, since this is required in the steady-state limit. Finally, the current can be derived directly from the solution of the quantum master equation.

2.2 The dressed second order approach applied to a CNT quantum dot

We apply the density matrix transport framework to a CNT quantum dot attached to ferromagnetic leads. In particular, we study the conductance in the Coulomb blockade regime through a quantum dot attached to leads that can be switched from a state with parallel magnetization (G_p) to a state with anti-parallel magnetization (G_ap). G_p and G_ap define the so-called tunneling magneto-resistance (TMR) [71, 72]:

$$\mathrm{TMR} = G_\mathrm{p}/G_\mathrm{ap} - 1.$$

As elucidated in Sec. 1.1, the conductance in the Coulomb blockade regime has a pronounced resonant structure. This leads to large TMR values if the positions and widths of the resonances depend on the magnetization configurations p and ap.

In Fig. 2.1(a) we show TMR data recorded across four conductance resonances at $V_\mathrm{g} = 8.13\,\mathrm{V}$, $8.15\,\mathrm{V}$, $8.17\,\mathrm{V}$ and $8.19\,\mathrm{V}$ (not shown). In the strong variations in the TMR we observe two distinct patterns. In the first two signatures, at $V_\mathrm{g} \sim 8.13\,\mathrm{V}$ and $V_\mathrm{g} \sim 8.15\,\mathrm{V}$, a dip is followed by a peak while for $V_\mathrm{g} \sim 8.17\,\mathrm{V}$ and $V_\mathrm{g} \sim 8.19\,\mathrm{V}$, a dip-peak-dip structure can be observed. How can we capture this behavior in our model? First of all, the commonly used perturbative description of the Coulomb resonances, which is similar to the second order approach of the last section, predicts temperature broadened peaks and maxima whose positions are solely determined by the isolated quantum dot spectrum implying a constant, positive TMR [70].

Our goal is to extend the second order result in such a way that it reproduces the observed signatures but the complexity of the model remains manageable. To this end we need to clarify the necessary ingredients to produce TMR signatures as those shown in Fig. 2.1(a).

On a qualitative level, the occurrence of the signatures can be understood from properties of the conductance peaks in the parallel and anti-parallel configurations of the contacts. In Fig. 2.1(b), the peak in the conductance G_p in presence of leads with parallel spin polarization is shifted with respect to the one in G_ap, the conductance in the anti-parallel case. This shift yields a dip-peak feature in the TMR signal as shown in (d). This signature has also been observed in Ref. [73]. In Fig. 2.1(c), a change of the resonance line-width between the two configurations yields a dip-peak-dip sequence in the TMR, shown in (e). This signature, too, has been observed previously [74].

The extension of the second-order transport framework thus has to account for a shift and for a broadening of the conductance peak in the Coulomb blockade regime depending on the magnetization of the contacts. In Ref. [75], a transport theory has been developed which accounts for a shift of the quantum dot energy levels in a multi-level quantum dot depending on the magnetization configuration of the leads. The model includes charge fluctuations between the dot and the contacts non-perturbatively. Within an extension of this theory, the "dressed second order" (DSO) framework, J. Kern et al. [57] showed that the charge fluctuations can also be responsible for a broadening of the conductance peak in the single impurity Anderson model with normal metal leads. It correctly captures the crossover from thermally broadened conductance peaks to peaks that are broadened by tunneling processes. Here, we combine the two works and apply the DSO to the CNT quantum dot with ferromagnetic leads.

In the following we will present the Hamiltonian of the CNT quantum dot, review briefly the second order result for this model and extend it to account for broadening and renormalization effects. Following the lines of Ref. [57] we use a specific selection of terms from Eq. (2.18), i.e., terms that describe charge fluctuations in the Kernel and solve the QME.

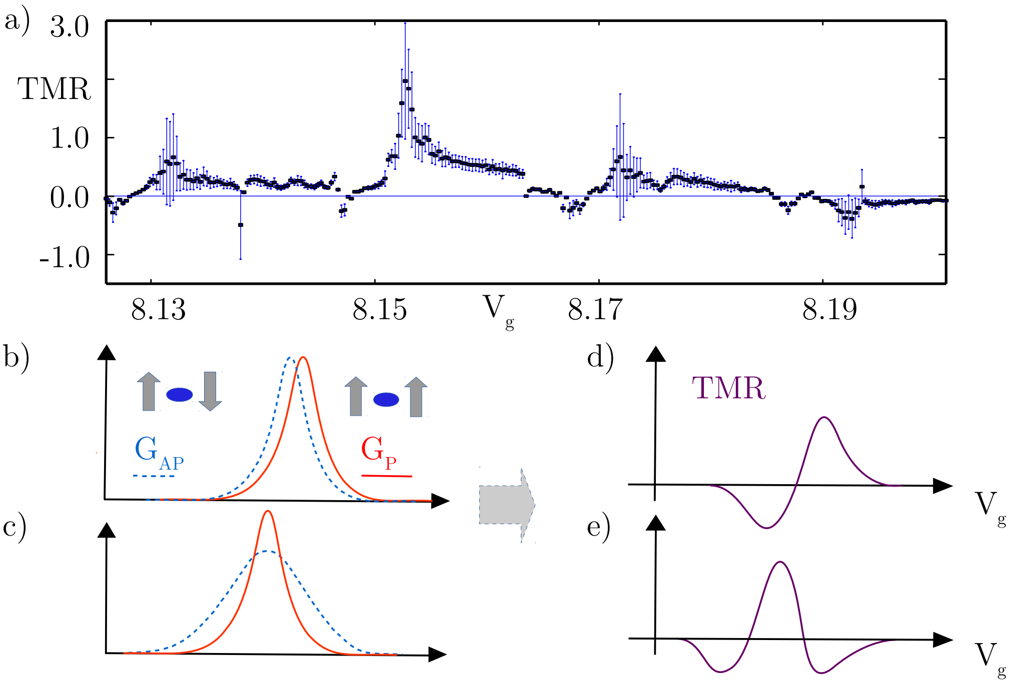

Figure 2.1: (a) TMR measured across four conductance resonances. The first two resonances show clear dip-peak signatures, in the last two resonances a second dip follows after the first dip. (b,c) Schematic drawing of the lead induced, polarization dependent, modification of position (b) and width (c) of a peak in the conductance across a quantum dot as a function of the gate voltage. (d,e) As a consequence of the level shift (b) and level broadening (c) in the conductance resonances, the corresponding TMR signal exhibits a characteristic dip-peak (d), or dip-peak-dip (e) feature as they can both be observed in (a).

2.2.1 The Hamiltonian of the system

We treat the system as an isolated quantum dot coupled to metallic leads. The Hamiltonian of such a system reads $\hat{\mathrm{H}} = \hat{\mathrm{H}}_{\mathrm{R}} + \hat{\mathrm{H}}_{\mathrm{D}} + \hat{\mathrm{H}}_{\mathrm{T}}$. Here,

$$\hat{\mathrm{H}}_{\mathrm{R}} = \sum_{l\sigma\mathbf{k}} \epsilon_{l\sigma\mathbf{k}} \hat{c}^{\dagger}_{l\sigma\mathbf{k}} \hat{c}_{l\sigma\mathbf{k}}$$

is the Hamiltonian of an ensemble of non-interacting electrons in the leads $l = \mathrm{s/d}$ with wave vector $\mathbf{k}$ and spin σ. The operator $\hat{c}_{l\sigma\mathbf{k}}$ ($\hat{c}^{\dagger}_{l\sigma\mathbf{k}}$) annihilates (creates) an electron with energy $\epsilon_{l\sigma\mathbf{k}}$. The second part,

$$\hat{\mathrm{H}}_{\mathrm{D}} = \frac{1}{2} E_c \hat{\mathrm{N}}^2 + \sum_{n\tau\sigma} \left[\varepsilon(n) + \tau\sigma \frac{\Delta_{\mathrm{SO}}(n)}{2} \right] \hat{\mathrm{N}}_{n\tau\sigma} - e\alpha V_{\mathrm{g}} \hat{\mathrm{N}} + \hat{\mathrm{H}}^{\mathrm{P/A}}_{\mathrm{ext}} , \tag{2.39}$$

describes the electrons on the CNT quantum dot in terms of the quantum numbers n (shell), spin σ and valley τ. Here we used $\hat{\mathrm{N}}_{n\tau\sigma} = \hat{d}^{\dagger}_{n\tau\sigma} \hat{d}_{n\tau\sigma}$, with the fermionic dot operator $\hat{d}_{n\tau\sigma}$ and $\hat{\mathrm{N}} = \sum_{n\tau\sigma} \hat{\mathrm{N}}_{n\tau\sigma}$, the total dot occupation. For our purposes, it is sufficient to account for Coulomb interaction effects in terms of a capacitive charging energy E_{c}. Short range exchange contributions are neglected here. The symbols τ and σ represent the eigenvalues ± 1 of the states with quantum numbers K, K' and $\uparrow$,$\downarrow$, respectively. In the CNT, a non-zero spin-orbit coupling Δ_{SO} can lead to the formation of two non-degenerate Kramers pairs [17]. Notice that, for simplicity, a valley mixing contribution is not included in Eq. (2.39). Hence, the valley degree of freedom is a good quantum number to classify the CNT's states [37]. The next to last part of the Hamiltonian $\hat{\mathrm{H}}_{\mathrm{D}}$ models the effect of an electrostatic gate voltage V_{g} scaled by the conversion factor α, see Sec. 1.1. Finally, $\hat{\mathrm{H}}^{\mathrm{p/a}}_{\mathrm{ext}}$ accounts for external influences on the dot potential, e.g., stray fields from the contacts and the external magnetic field used to switch the contact polarization.

The ground states of shell n have $4n + a$ ($0 \leq a \leq 3$) electrons and will in the following be characterized by the quantum numbers of the excess electrons with respect to the highest filled shell $n - 1$. For instance, the quantum dot state labeled by $|K\uparrow; n\rangle$ contains $4n$ electrons plus one additional electron in the (K,$\uparrow$) state. Including states with $4n - 1$ and $4n + 5$ electrons we end up with 6 ground states with different degeneracies (see Tab. 2.1, left column). In total we consider a Fock space of dimension 24 if the four-fold degeneracy is not lifted by a sufficiently large spin-orbit coupling Δ_{SO}. The extra states with occupation $4n-1$ and $4n+5$ are included to allow for charge fluctuations in and out of the shell n under consideration. Conversely, for large enough spin-orbit coupling the dimension of the Fock space is reduced to 10, see Tab. 2.1, right column. For a compact notation, the shell number will in the following be neglected from the state ket if not necessary.

$N_{\rm rel}$	$\Delta_{\rm SO} \leq \max\{k_{\rm B}T, \gamma_0\}$	$\Delta_{\rm SO} \gg \max\{k_{\rm B}T, \gamma_0\}$
-1	$\vert K\uparrow, K\downarrow, K'\uparrow; n-1\rangle$	$\vert K\uparrow, K\downarrow, K'\uparrow; n-1\rangle$
	$\vert K\uparrow, K\downarrow, K'\downarrow; n-1\rangle$	$\vert K\uparrow, K\downarrow, K'\downarrow, n-1\rangle$
	$\vert K\uparrow, K'\uparrow, K'\downarrow; n-1\rangle$	
	$\vert K\downarrow, K'\uparrow, K'\downarrow, n-1\rangle$	
0	$\vert n\rangle$	$\vert n\rangle$
1	$\vert K\uparrow; n\rangle$ $\vert K\downarrow; n\rangle$	$\vert K\uparrow; n\rangle$ $\vert K\downarrow; n\rangle$
	$\vert K'\uparrow; n\rangle$ $\vert K'\downarrow; n\rangle$	
2	$\vert K\uparrow, K\downarrow; n\rangle$ $\vert K\uparrow, K'\uparrow; n\rangle$	$\vert K\uparrow, K\downarrow, n\rangle$
	$\vert K\uparrow, K'\downarrow; n\rangle$ $\vert K\downarrow, K'\uparrow; n\rangle$	
	$\vert K\downarrow, K'\downarrow; n\rangle$ $\vert K'\uparrow, K'\downarrow; n\rangle$	
3	$\vert K\uparrow, K\downarrow, K'\uparrow; n\rangle$	$\vert K\uparrow, K\downarrow, K'\uparrow; n\rangle$
	$\vert K\uparrow, K\downarrow, K'\uparrow; n\rangle$	$\vert K\uparrow, K\downarrow, K'\downarrow; n\rangle$
	$\vert K\uparrow, K'\uparrow, K'\downarrow; n\rangle$	
	$\vert K\downarrow, K'\uparrow, K'\downarrow; n\rangle$	
4	$\vert n+1\rangle$	$\vert n+1\rangle$
5	$\vert K\uparrow; n+1\rangle$ $\vert K\downarrow; n+1\rangle$	$\vert K\uparrow; n+1\rangle$ $\vert K\downarrow; n+1\rangle$
	$\vert K'\uparrow; n+1\rangle$ $\vert K'\downarrow; n+1\rangle$	

Table 2.1: The set of allowed electronic ground states C of the CNT with N electrons for large (right) and small (left) spin-orbit coupling $\Delta_{\rm SO}$. The degeneracy of the configuration depends on the magnitude of $\Delta_{\rm SO}$ as compared to $k_{\rm B}T$ or the coupling strength γ_0. In the first column, the excess electron number $N_{\rm rel} = N - 4n$ is reported with respect to the number $4n$ of electrons in the filled $(n-1)$-th shell.

Quantum dot and metallic leads are coupled perturbatively by a tunneling Hamiltonian

$$\hat{\mathrm{H}}_{\mathrm{T}} = \sum_{l\mathbf{k}n\sigma\tau} T_{l\mathbf{k}n\sigma\tau}\, \hat{\mathrm{d}}^{\dagger}_{n\sigma\tau}\, \hat{\mathrm{c}}_{l\mathbf{k}\sigma} + \mathrm{h.\,c.}, \tag{2.40}$$

with a tunnel coupling $T_{l\mathbf{k}n\sigma\tau}$ generally dependent on the quantum numbers of both leads and quantum dot. In the following, for simplicity, we assume that $T_{l\mathbf{k}n\sigma\tau} = T_l$.

We identify the operators introduced in Sec. 2.1.3,

$$\hat{\mathrm{S}}^{+}_{i}\, \hat{\mathrm{E}}^{-}_{i} = T_l\, \hat{\mathrm{d}}^{\dagger}_{n\sigma\tau}\, \hat{\mathrm{c}}_{l\mathbf{k}\sigma} \qquad \text{and} \qquad \hat{\mathrm{S}}^{-}_{i}\, \hat{\mathrm{E}}^{+}_{i} = T^{*}_{l}\, \hat{\mathrm{d}}_{n\sigma\tau}\, \hat{\mathrm{c}}^{\dagger}_{l\mathbf{k}\sigma}\,.$$

In the thermodynamic limit, the trace over the eigenstates of the reservoirs can be replaced by an integral over energies,

$$\mathrm{Tr}\left\{ \frac{\hat{\mathrm{c}}^{p}_{l\mathbf{k}\sigma}\, \hat{\mathrm{c}}^{\bar{p}}_{l\mathbf{k}\sigma}\, \hat{\rho}_l}{\cdots} \right\} = \int \mathrm{d}\epsilon\, \frac{2\pi \mathcal{D}_{l\sigma}(\epsilon) f^{p}_{l}(\epsilon)}{\cdots},$$

where f is the Fermi function and $\mathcal{D}_{l\sigma}(\epsilon)$ is the spin-dependent density of states. A Lorentzian provides a cut-off for the density of states at a bandwidth W. It is convenient to introduce a spin dependent linewidth for the transition $|a\rangle \to |b\rangle$,

$$\gamma^{ba}_{l}(\epsilon) = \gamma_{l\sigma(b,a)}(\epsilon) = |T_l|^2 \mathcal{D}_{l\sigma}(\epsilon).$$

The notation $\sigma(a, b)$ indicates that the spin σ of the electron tunneling out of/onto lead l depends on the spin configuration of the initial state a and the final state b of the quantum dot. Furthermore we introduce the spin-resolved density of states of lead l at the Fermi energy

$$\mathcal{D}_{l\sigma} = \mathcal{D}_{l\sigma}(\epsilon_{\mathrm{F}}) = D_0(1 + \sigma P_l)/2, \tag{2.41}$$

where $P_l = (\mathcal{D}_{l\uparrow} - \mathcal{D}_{l\downarrow})/(\mathcal{D}_{l\uparrow} + \mathcal{D}_{l\downarrow})$ is the polarization of lead l. The couplings $|T_l|^2$ we define in the same spirit as

$$|T_{s/d}|^2 = |T_0|^2 (1 \pm a)/2, \tag{2.42}$$

using the parameter a to tune the asymmetry in the coupling to the leads. We will in the following use the factorization

$$\gamma_{l\sigma(b,a)}(\epsilon_{\mathrm{F}}) = \gamma_0 \kappa_{l\sigma}, \tag{2.43}$$

where we collect the lead and spin independent prefactors in an overall coupling strength $\gamma_0 = D_0 |T_0|^2$ and include the dependence on spin and lead index in the dimensionless parameter $\kappa_{l\sigma}$, where $\sum_{l\tau\sigma} \kappa_{l\sigma} = 1$. Note that γ_0 is related to the level broadening Γ_0 by $\Gamma_0 = 2\pi\gamma_0$.

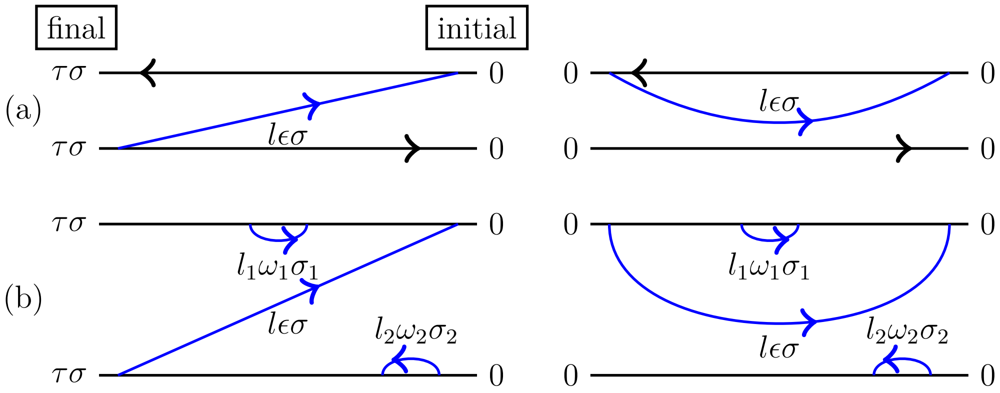

Figure 2.2: Diagrammatic representations of the contributions to the rate $\Gamma^{+}_{l,\tau\sigma 0}$ in second order (a), and an example of diagrams included in the DSO (b). In the latter case, the second order diagrams in (a) are "dressed" by charge fluctuation processes. The labels below the fermion lines denote energy and spin of the particle tunneling from/onto the lead. Note that the diagram is read from right to left, i.e., the initial state $|0\rangle$ can be found on the right and the final state $|\tau\sigma\rangle$ on the left.

2.2.2 Lowest (second) order in the coupling

Evaluating the kernel to the lowest order in the coupling Hamiltonian and expressing the result using the diagrammatic rules in Sec. 2.1.3 we end up with the two diagrams shown in Fig. 2.2(a). From this representations we can directly derive the Laplace transforms of the kernel elements. For a diagram of order $2n$ this can be done according to the following rules [69]:

1. To each of the n fermion lines assign an energy ϵ as well as the lead and spin indices l, σ, respectively.

2. To each section on the contours assign the energy of the corresponding state.

3. Between two consecutive times t and t', draw a vertical line that intersects both the fermion lines inside the diagram and the contours:

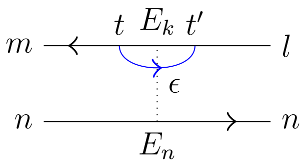

Each crossing of the dotted line with the fermion line and the contours corresponds to a summand in the denominator D of the Laplace transform. Whenever the fermion line or the contour intersects from left to right we choose a positive sign, otherwise the contribution is negative:

$$D = E_l - E_n - \epsilon$$

4. Determine a sign p for the fermion line which tells whether it belongs to an in-tunneling ($p = +$) or an out-tunneling ($p = -$) event:

vertices lie	line points	p
on the same contour	forward	-
on the same contour	backward	+
on different contours	upwards	+
on different contours	downwards	-

5. Determine q which accounts for the sign of the contribution: q is equal to the number of the vertices on the lower contour.

6. The integral part of the kernel thus reads

$$I^{(2)} = -(-1)^q \frac{\mathrm{i}}{\hbar} \lim_{\lambda \to 0^+} \int \mathrm{d}\epsilon \, \frac{f_l^p(\epsilon)}{D(\epsilon) + \mathrm{i}\lambda} \tag{2.44}$$

7. Assign to each vertex the coupling

$$\gamma_{l\sigma(b,a)}(\epsilon)$$

   where a is the state on the contour before the vertex, b is the state after the vertex and ϵ is the energy corresponding to the Fermion line. p is positive/negative for a fermion line pointing towards/away from the vertex.

Integrals like the one in Eq. (2.44) can be calculated by introducing a Lorentzian function to suppress values on the semi-circle over the imaginary half-plane. We write

$$Y_d^p(\Delta) = -\frac{\mathrm{i}}{\hbar} \lim_{w \to \infty} \lim_{\lambda \to 0^+} \int \mathrm{d}x \, \frac{f^p(x)}{d(x - \beta\Delta) + \mathrm{i}\lambda} \frac{w^2}{w^2 + x^2}$$

and convince ourselves that part of the path on the semi-circle vanishes. We are left with the residuals and obtain, after some manipulation [69],

$$Y_d^p(\Delta) = -\frac{\pi}{\hbar} f^{pd}(\beta\Delta) - \mathrm{i}pd \left(\operatorname{Re} \Psi^{(0)} \left(\frac{1}{2} + \mathrm{i}\frac{\beta\Delta}{2\pi} \right) - C \right). \tag{2.45}$$

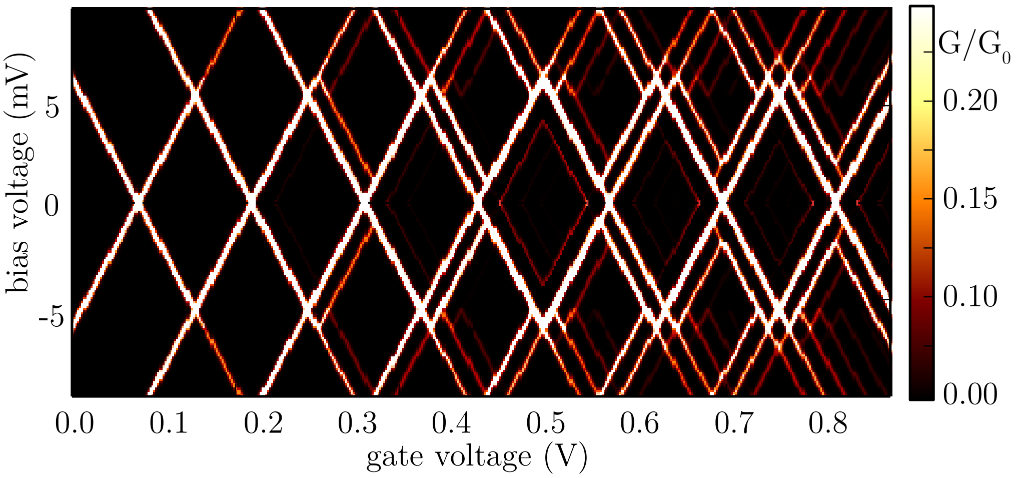

Figure 2.3: Conductance as a function of gate and bias voltage calculated in the sequential tunneling approximation using the Hamiltonian in Eq. (2.39). $G_0 = e^2/h$.

This yields for the second order rates

$$\Gamma^p_{l,ba} = \frac{2\pi}{\hbar}\gamma_{l\sigma(b,a)} f^p_l(E^b_a). \tag{2.46}$$

Note that the hermitian conjugate can be extracted by inverting the signs p and d for Y in Eq. (2.45). The energy difference $E^b_a = E_b - E_a = \tilde{E}_b - \tilde{E}_a - e\alpha V_\mathrm{g}(N_b - N_a)$ depends on the gate voltage V_g while the Fermi function f^p_l depends on the electrochemical potential of the leads and thus on the bias voltage V_b. Due to the apparent simplicity of Eq. (2.46), the second order model can be easily evaluated for larger ranges in V_g and V_b. In Fig. 2.3 the conductance through the QD as described by the Hamiltonian in Eq. (2.39) is shown. Note that at second order in the coupling the width of the peak in the conductance as a function of gate voltage only depends on temperature and the positions of the peaks depend on the energy levels of the quantum dot [75]. From this it follows that the ration $G_\mathrm{p}/G_\mathrm{ap}$ is constant as a function of the gate voltage and so is the TMR.

2.2.3 The dressed-second order series

In the DSO, we include all diagrams of the structure shown in Fig. 2.2(b) in addition to the lowest (second) order contributions. The selected diagrams contain arbitrary numbers of uncorrelated charge fluctuation processes (“bubbles” in Fig. 2.2(b)). Let us have a look at the example in Fig. 2.2(a) and

(b) for the transition from $|0\rangle$ to $|\tau\sigma\rangle$. During the charge fluctuation, the dot state on the upper contour has one charge less or more compared to that of the final state $|\tau\sigma\rangle$. Hence, the virtual state is either the state $|0\rangle$ or one of the many (see Tab. 2.1) doubly occupied states. On the lower contour, the fluctuations take place with respect to the initial state $|0\rangle$. Examples of charge fluctuations in the case of initial state $|0\rangle$ and final state $|K\uparrow\rangle$ are shown in Fig. 2.4. In Ref. [57], J. Kern et al. show that the sum of all diagrams of this type recovers a closed analytic form. We demonstrate this procedure by an example calculation for the transition $|0\rangle \to |\tau\sigma\rangle$.

Example calculation We recall the second order diagram in Fig. 2.2(a),

$$\Gamma^{+,(2)}_{l,|0\rangle|\tau\sigma\rangle} =$$

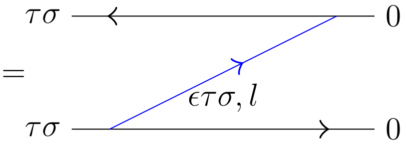

$$+ \text{ h. c.}$$

which we can translate to an analytic expression via the diagrammatic rules of Sec. 2.2.2. We obtain

$$\Gamma^{+,(2)}_{l,|0\rangle|\tau\sigma\rangle} = \frac{\mathrm{i}}{\hbar} \lim_{\lambda\to 0^+} \int \mathrm{d}\epsilon \, \frac{\gamma_{l\sigma}(\epsilon) f_l^+(\epsilon)}{E_0^{\tau\sigma} - \epsilon + \mathrm{i}\lambda} + \text{ h. c.}\,.$$

Let us now add a charge fluctuation. In the diagrammatic language, this is represented by a bubble. At fourth order in the coupling we thus obtain

$$\Gamma^{+,(4)}_{l,|0\rangle|\tau\sigma\rangle} =$$

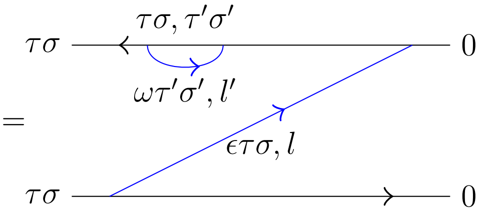

(i)

$$+\text{(ii)} + \text{(iii)} + \text{(iv)} + \text{ h. c..}$$

The labels (i-iv) distinguish four related diagrams: We can invert the blue arrow of the bubble and obtain an out-tunneling contribution or place the bubble on the lower contour where we again have two choices for the direction of the arrow. Note that we have to choose additional quantum numbers ω, τ' and σ' for the charge fluctuation state. The possibilities in choosing the quantum numbers for the charge fluctuation state are only restricted by the occupation of the quantum dot, since no two electrons can share the same set of quantum numbers. Following the diagrammatic rules we end up with the

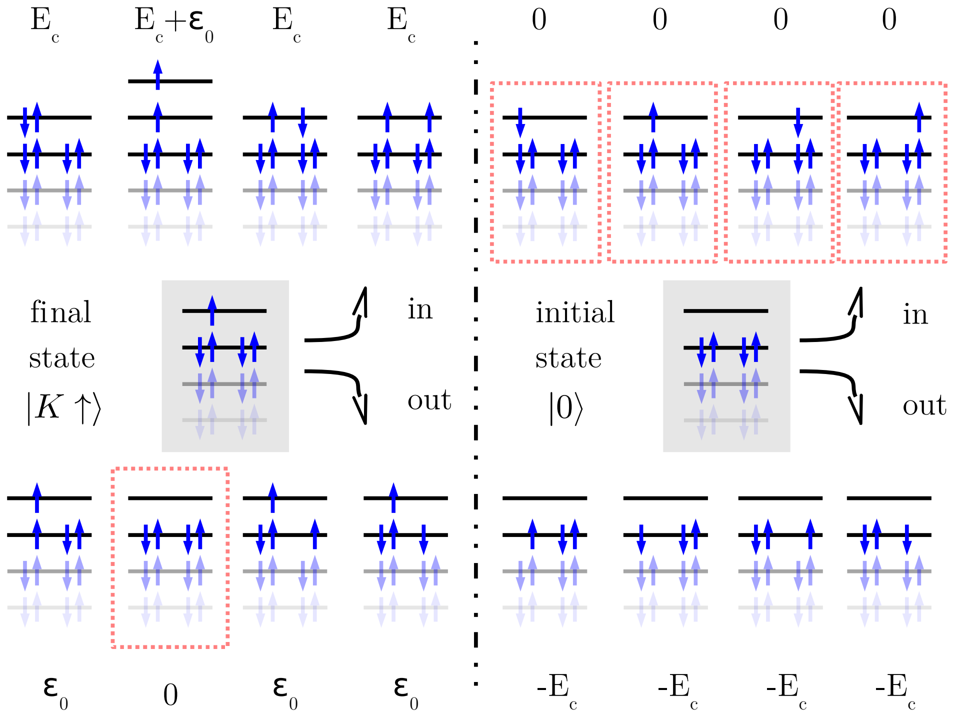

Figure 2.4: Example of possible charge fluctuations for a final state ($|K{\uparrow}\rangle$, left, shaded gray) with one extra electron and an initial state with zero electrons in the shell n ($|0\rangle$, right, shaded gray). This set corresponds to one specific diagram of the type shown in Fig. 2.2(b). States that can be reached by in-tunneling of an electron are shown on top, states that can be reached by out-tunneling of an electron are shown on the bottom. Dashed frames highlight resonant ($E_{a/c'}^{c'/b} = 0$) charge fluctuations. Above and below the level schemes, the energy difference between the virtual state and the state on the other contour is given: the energies of the states accessible from the initial (final) state are compared to the energy of the final (initial) state on resonance ($\tilde{E}_0^{K\uparrow} = e\alpha V_\mathrm{g}$). Note that the electron number of the states that can be reached by in-tunneling on the left and the number of electrons in the initial state on the right differ by two. The same situation occurs for the final state and the out-tunneling states on the right. The energy differences for this class of fluctuations is of the order of E_c. A comparison of the electron number of the final state with the in-tunneling states on the left and the initial state with the out-tunneling states on the right yields a difference of zero. These fluctuations have comparably low energy cost.

No.	diagram	
(i)	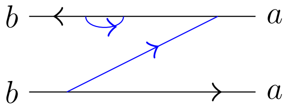	$\sum_l \int \mathrm{d}\omega \, \frac{\gamma_{l\sigma(c'b)}(\omega) f_l^+(\omega)}{\omega+\epsilon-E_a^{c'}+\mathrm{i}\eta}$
(ii)	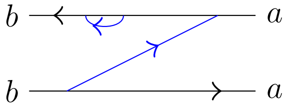	$\sum_l \int \mathrm{d}\omega \, \frac{\gamma_{l\sigma(c'b)}(\omega) f_l^-(\omega)}{-\omega+\epsilon-E_a^{c'}+\mathrm{i}\eta}$
(iii)	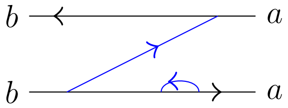	$\sum_l \int \mathrm{d}\omega \, \frac{\gamma_{l\sigma(c'a)}(\omega) f_l^+(\omega)}{\omega+\epsilon-E_{c'}^{b}+\mathrm{i}\eta}$
(iv)	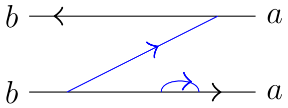	$\sum_l \int \mathrm{d}\omega \, \frac{\gamma_{l\sigma(c'a)}(\omega) f_l^-(\omega)}{-\omega+\epsilon-E_{c'}^{b}+\mathrm{i}\eta}$

Table 2.2: Fourth order contributions considered in the dressed second order summation. The integral representation is given on the right side.

Laplace transform

$$(\mathrm{i}) = \frac{\mathrm{i}}{\hbar}\times$$
$$\lim_{\lambda\to 0^+} \int \mathrm{d}\epsilon \, \frac{\gamma_{l\sigma}(\epsilon) f_l^+(\epsilon)}{E_0^{\tau\sigma}-\epsilon+\mathrm{i}\lambda}\left(\frac{-1}{E_{\sigma 0}^{\tau\sigma}-\epsilon+\mathrm{i}\lambda}\right)\left[\sum_{l'}\int \mathrm{d}\omega \, \frac{\gamma_{l'\sigma'}(\omega) f_{l'}^+(\omega)}{E_0^{\tau\sigma,\tau'\sigma'}-\epsilon-\omega+\mathrm{i}\lambda}\right]$$

omitting the hermitian conjugate. To shorten the notation a bit, we will in the following use the labels $a=|0\rangle$, $b=|\tau\sigma\rangle$ and c' for the state that can be reached by a charge fluctuation. Using this notation, the other diagram types that are considered within the DSO and the associated innermost integral are given in Tab.2.2. Stringing together additional bubbles on the two contours produces additional terms (i-iv). Let us add n charge fluctuations of types (i-iv), i.e.,

$$\Gamma_{l,ba}^{+,(n)} =$$
$$\mathrm{Re}\left\{\frac{1}{\hbar}\int \mathrm{d}\epsilon \, \frac{\gamma_{l\sigma(ba)}(\epsilon)}{\lambda+\mathrm{i}(\epsilon-E_a^b)}\left(\frac{-1}{\lambda+\mathrm{i}(\epsilon-E_a^b)}\right)^n\Big[(\mathrm{i})+(\mathrm{ii})+(\mathrm{iii})+(\mathrm{iv})\Big]^n\right\}. \tag{2.47}$$

For $n\to\infty$, the series converges [57] and Eq. (2.47) is transformed into

$$\Gamma_{l,ba}^{+} = \frac{1}{2\pi\hbar}\int \mathrm{d}\epsilon \, \nu_l^{ba}(\epsilon) f_l^+(\epsilon). \tag{2.48}$$

Similarly, the out-tunneling rate reads

$$\Gamma^{-}_{l,ab} = \frac{1}{2\pi\hbar}\int \mathrm{d}\epsilon\, \nu_l^{ba}(\epsilon) f_l^{-}(\epsilon) \tag{2.49}$$

for an out-tunneling process $b \to a$. We introduced a tunneling-like density of states (TDOS)

$$\nu_l^{ba}(\epsilon) = \frac{\gamma_l^{ba}(\epsilon)\,\mathrm{Im}(\Sigma^{ba}(\epsilon))}{[\mathrm{Im}(\Sigma^{ba}(\epsilon))]^2 + [\epsilon - E_a^b + \mathrm{Re}(\Sigma^{ba}(\epsilon))]^2}. \tag{2.50}$$

The contributions from Tab.2.2 are collected in the self energy $\Sigma^{ba}(\epsilon)$ in the denominator. Explicitly,

$$\Sigma^{ba}(\epsilon) = \text{(i)} + \text{(ii)} + \text{(iii)} + \text{(iv)} = \sum_{\substack{c\in\{b,a\}\\ c'\in C_c^{\pm}}} a_{ba}^{c'c}(\epsilon), \tag{2.51}$$

with the sets $C^{\pm}_{b/a}$ given by

$$C^{\pm}_{b/a} \coloneqq \{c' : N_{c'} = N_{b/a} \pm 1 \wedge 4n - 1 \leq N_{c'} \leq 4n + 5\}. \tag{2.52}$$

The sets are shown in Fig. 2.4 for the states $|a\rangle = |0\rangle$ and $|b\rangle = |K\uparrow\rangle$. The rate equations Eq. (2.48) and Eq. (2.49) describe the transition between arbitrary states a and b in the state space given in Tab. 2.1. The summand

$$a_{ba}^{c'(b/a)}(\epsilon) = \sum_l \int \mathrm{d}\omega\, \frac{\gamma_l^{c'(b/a)}(\omega) f_l^p(\omega)}{\pm p\omega + \epsilon - E_{a/c'}^{c'/b} + \mathrm{i}\eta}$$

accounts for a transition from b or a to a state c', with $c' \in C^p_{b/a}$. Performing the integral, we arrive at an analytic expression for the contributions to the self energy, i.e.,

$$\begin{aligned} a_{ba}^{c'(b/a)}(\epsilon) = \sum_l \gamma_l^{c'(b/a)}(\epsilon)\Bigg\{ &\mathrm{i}\pi f_l^p(\pm p(E_{a/c'}^{c'/b} - \epsilon)) \\ &\pm \Big[\bar{\Psi}^{(0)}(W) - \mathrm{Re}\Big[\bar{\Psi}^{(0)}\Big(\mathrm{i}\,(\mu_l \pm p(E_{a/c'}^{c'/b} - \epsilon))\Big)\Big]\Big]\Bigg\}, \end{aligned} \tag{2.53}$$

where $\bar{\Psi}^{(0)}(x) = \Psi^{(0)}(0.5 + x/2\pi k_{\mathrm{B}}T)$ and $\Psi^{(0)}$ is the digamma function. Note that the dependence on the bandwidth drops out due to the alternating sign of the contributions from the upper and lower contour in the summation in Eq. (2.51). Having calculated the self energy, we are now able to collect all rates according to the transitions in our state space, and solve the stationary

Eq. (2.28) to obtain the occupation probabilities $\rho_{aa} = P_a$. Within the steady state limit we can neglect off-diagonal entries ρ_{ba} if they are among non-degenerate states [75]. According to Tab. 2.1, the CNT spectrum can be spin and valley degenerate. However, the tunneling Hamiltonian (2.40) conserves the spin during tunneling, and thus spin coherences are not present in the dynamics. Here, for simplicity, orbital coherences are neglected as well.[2]

Current within the DSO

The current through the terminal l can be written in terms of the difference of in- and out-tunneling contributions at the junction, see Eq. (2.38):

$$I_l(V_\mathrm{b}) = \frac{e}{2\pi\hbar} \sum_{\substack{a\in C\\ c\in C_a^+}} \int \mathrm{d}\epsilon\ \Big[P_a(V_\mathrm{b}) f_l^+(\epsilon) - P_c(V_\mathrm{b}) f_l^-(\epsilon)\Big]\, \nu_l^{ca}(\epsilon, V_\mathrm{b}), \tag{2.54}$$

where V_b is the bias voltage applied between the two contacts, and C is the set of all possible configurations (see Tab. 2.1). In general, the populations can be expressed in terms of rates via Eq. (2.32) and a closed form for the current and, consequently, for the conductance can be found. This is straightforward if two states are connected by pairwise gain-loss relations [76]. For the case of the single impurity Anderson model, for example, a compact notation of the conductance can be given [57]. In this work, the conductance data from the model is calculated numerically. The source code for the numerical calculation can be found on `https://github.com/Loisel/tmr3`.

The width of a resonance in conductance with respect to the gate potential is determined by the populations, the TDOS which has a form similar to a Lorentzian, and by the derivative of the Fermi functions. Note that the populations are themselves a function of the rates and therefore are also governed by the resonance conditions of the rates. The DSO theory has been proven to be quantitatively valid down to temperatures $4k_\mathrm{B}T \sim \gamma_0$ in the single electron transistor [57]. Upon decreasing of the temperature below $\gamma_0/4$, a quantitative description of the transition rate Γ_l^{ac} would require to calculate Σ beyond the lowest order in γ_0. In the regime where temperature and coupling are of comparable magnitude, the width and position of the Coulomb blockade peaks in a gate trace are strongly influenced by the TDOS and, more precisely, by the self energy Σ. The role of $\mathrm{Re}(\Sigma)$ is to influence

---

[2] For CNTs of the zigzag type, coherences are not expected to contribute to the dynamics for tunneling processes which conserve the crystal angular momentum, i.e., for which the perpendicular component $k_\perp$ of the momentum $\mathbf{k}$ is conserved during tunneling. This is because in zigzag type CNTs the two valleys correspond to different values of the crystal angular momentum.

the positions of the Coulomb blockade peaks: In the rate for the transition a to b, the real part appears next to the energy difference E_a^b of the transition in the denominator. Hence, due to this contribution the resonant level is shifted depending on the configuration of the leads.

Renormalization of excited states

Let us analyze the effect of the DSO on the position of excited state lines in the stability diagram. The condition for a resonant transition between states a and b is given by

$$\epsilon \pm eV_\mathrm{b}/2 + e\alpha V_\mathrm{g} - \tilde{E}_a^b + \mathrm{Re}(\Sigma^{ba}) = 0, \tag{2.55}$$

where ϵ is the energy of the tunneling electron with respect to the chemical potential of the contact it originates from, i.e., of the source contact ($+eV_\mathrm{b}$) or of the drain contact ($-eV_\mathrm{b}$). We assume here a symmetric voltage drop across the two contacts, $\alpha_\mathrm{s} = 1/2$, compare Eq. (eq:intro-left-energy). Note that the condition in Eq. (2.55) can be fulfilled for different transitions at the same time, a situation that occurs at any point where two lines in a stability diagram intersect. In order to interpret a shift of the excited state line in the differential conductance it is illuminating to study the contribution from $\mathrm{Re}(\Sigma)$ at points $(V_{\mathrm{g}1}, V_{\mathrm{b}1})$ and $(V_{\mathrm{g}2}, V_{\mathrm{b}2})$ marked by a dot and a circle, respectively, in Fig. 2.5. We consider an exemplary set of states $0 = |0; n\rangle$, $1 = |K\!\uparrow; n\rangle$, $1'_1 = |[K\!\uparrow]; n\rangle$, $1'_2 = |K\!\uparrow, K\!\downarrow, (K'\!\uparrow); n\rangle$ and $2 = |K\!\uparrow, K\!\downarrow; n\rangle$. A similar analysis can be carried out for other states with $4n+1$ and $4n+2$ electrons. The quantum numbers in round brackets denote a missing electron of shell $n-1$ whereas the square brackets indicate a state of shell $n+1$. For each of the highlighted points in Fig. 2.5, two conditions in the form of Eq. (2.55) can be given. Subtracting them pairwise we are left with

$$eV_{\mathrm{b}1} - E_1^{1'} + [\mathrm{Re}(\Sigma^{1',0}) - \mathrm{Re}(\Sigma^{1,0})] = 0, \tag{2.56}$$

$$eV_{\mathrm{b}2} - E_1^{1'} + [\mathrm{Re}(\Sigma^{2,1}) - \mathrm{Re}(\Sigma^{2,1'})] = 0, \tag{2.57}$$

where the self energy contributions depend on bias and gate voltage. To lowest order in γ_0 we analyze the differences in $\mathrm{Re}(\Sigma)$ using $eV_{\mathrm{b}1/2} = E_1^{1'}$ and $\alpha eV_\mathrm{g}^{1/2} = \tilde{E}_{0/1}^{1/2} \pm eV_\mathrm{b}$ at $\epsilon = 0$. In order to calculate $\mathrm{Re}(\Sigma)$ we have to analyze the contributions from all accessible states in Eq. (2.51). In principle there are arbitrarily many states that can be reached by a charge fluctuation. However, we assert that the available energy interval for charge fluctuation processes is given by $\max(eV_\mathrm{b}, \Gamma_0, 3 - 4k_\mathrm{B}T)$ and contributions beyond this scale are suppressed. Numerical results using a larger bandwidth can be found in Sec. 2.C of the appendix.

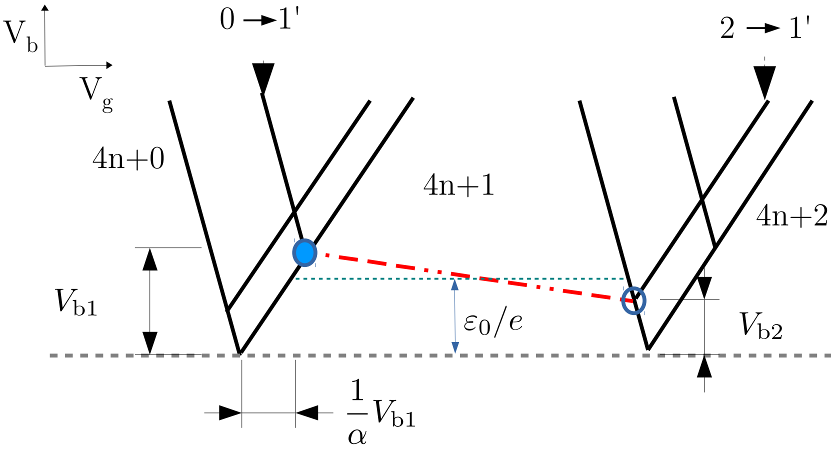

Figure 2.5: Schematic drawing of the conductance lines in the vicinity of the charging state with $4n+1$ electrons. The transition corresponding to the first excitation is shifted upwards in energy on the left and downwards on the right side of one charging diamond by $e(V_{b1}-V_{b2}) = -\delta_1$. For our analysis we choose bias and gate voltages close to the filled dot for the first transition $0 \to 1'$ and to the empty circle for the second transition $2 \to 1'$.

For our considerations we assume that the spin orbit coupling of our CNT quantum dot is small, i.e., $\Delta_{\rm SO} < \max(k_{\rm B}T, \Gamma)$. The other important scales - charging energy, shell spacing and linewidth - are related in the way $E_{\rm c} > \varepsilon_0 \gg \max(k_{\rm B}T, \gamma_0)$. Within this choice of parameters the difference of the self energy corrections for the resonant transition can be calculated by (2.56)−(2.57)= 0, i.e.,

$$\begin{aligned}\delta_1 &\equiv \left[\mathrm{Re}(\Sigma^{1'0}) - \mathrm{Re}(\Sigma^{10})\right] - \left[\mathrm{Re}(\Sigma^{21}) - \mathrm{Re}(\Sigma^{21'})\right] \\ &\simeq \gamma_0 \left\{-1 + 2\bar{\kappa}_{\rm s} - \bar{\kappa}_{\rm d} + \bar{\kappa}_{\uparrow} - \bar{\kappa}_{\downarrow}\right\} \bar{\Psi}^0_{\rm R}(\varepsilon_0/2) \qquad (2.58)\end{aligned}$$

where we used the abbreviation $\bar{\Psi}^0_{\rm R}(\epsilon) = \mathrm{Re}[\Psi^0(1/2 + \mathrm{i}\epsilon/2\pi k_{\rm B}T)]$ and a bar denotes a summation over indices, e.g., $\bar{\kappa}_l = \sum_\sigma \kappa_{l\sigma}$. A detailed derivation of these quantities is given in the appendix, Sec. 2.D. Similar calculations are performed for the excited states in the $n+2$ and $n+3$ diamonds, yielding

$$\begin{aligned}\delta_2 &\simeq \gamma_0 \left\{\bar{\kappa}_{\rm s} - \bar{\kappa}_{\rm d} + \kappa_{{\rm s}\downarrow} - \kappa_{{\rm d}\uparrow}\right\} \bar{\Psi}^0_{\rm R}(\varepsilon_0/2), \\ \delta_3 &\simeq \gamma_0 \left\{1 + \bar{\kappa}_{\rm s} - 2\bar{\kappa}_{\rm d} + \bar{\kappa}_{\downarrow} - \bar{\kappa}_{\uparrow}\right\} \bar{\Psi}^0_{\rm R}(\varepsilon_0/2),\end{aligned}$$

where the states with three electrons are chosen to be electron-hole symmetric with respect to the state with one electron. Note that for the case of symmetric couplings the shifts reflect the electron-hole symmetry of the system while a choice of $a \neq 0$ (Eq. (2.42)) breaks this symmetry. For highly asymmetric couplings $|a| \sim 1$ the shifts are comparable to those in Ref. [77].

2.2.4 Effects of magnetization on resonance width

Corrections to the conductance peak width are given by $\mathrm{Im}(\Sigma)$. Because $\mathrm{Re}(\Sigma)$ and $\mathrm{Im}(\Sigma)$ both depend on the different magnetic properties of the source and drain leads as well as on the dot's configuration, the resulting impact on the TMR is quite intricate. Thus we analyze the contributions to the self energy in the light of different configuration of the lead's polarizations. We focus on the transitions $|0, n+1\rangle \rightleftarrows \{|(\sigma\tau), n+1\rangle\}$. The back-gate voltage is tuned such that

$$\epsilon + e\alpha V_{\mathrm{g}} - \tilde{E}^0_{(\tau\sigma)} + \mathrm{Re}(\Sigma^{0,(\tau\sigma)}) = 0,$$

and the quantum numbers in round brackets $(\tau\sigma)$ denote a missing electron of shell $n+1$. At lowest order in the tunnel coupling γ_0 we approximate $e\alpha V_{\mathrm{g}} = \tilde{E}^0_{(\tau\sigma)}$ when we calculate $\mathrm{Re}(\Sigma^{0,(\tau\sigma)})$. From Eq. (2.53) we list the imaginary part of the self energy for this transition, i.e.,

$$\begin{aligned}\mathrm{Im}(\Sigma^{0,(\tau\sigma)}) = \pi\gamma_0 \sum_l \Bigg\{ & \sum_{c\in C_0^+} \kappa_{l\sigma(c)} f_l^+(E^c_{(\tau\sigma)} - \epsilon) + \sum_{c'\in C_0^-} \kappa_{l\sigma(c')} f_l^-(\epsilon - E^{c'}_{(\tau\sigma)}) \\ & + \sum_{c\in C^+_{(\tau\sigma)}} \kappa_{l\sigma(c)} f_l^+(\epsilon - E^0_c) + \sum_{c'\in C^-_{(\tau\sigma)}} \kappa_{l\sigma(c')} f_l^-(E^0_{c'} - \epsilon) \Bigg\}.\end{aligned}$$

The magnitude of the energy difference of the virtual state with respect to the state on the other contour determines whether a possible charge fluctuation contributes to the renormalization of the self energy or not: a contribution $f_l^+(E_{\mathrm{c}} - \epsilon)$, e.g., is exponentially suppressed in the vicinity of the resonance.

Therefore, knowing the arguments in the step functions $f^\pm$, we can simplify the result significantly. Close to the resonance where $|\epsilon| < \max(k_{\mathrm{B}}T, \gamma_0)$, the fluctuations with an energy cost of the charging energy E_{c} or of the shell spacing ε_0, e.g., the states that can be reached by out-tunneling from the state $|(\tau\sigma)\rangle$ can be neglected. Focusing on the resonant contributions, we are left with

$$\frac{\mathrm{Im}(\Sigma^{0,(\tau\sigma)})}{\pi\gamma_0} \simeq \sum_l \left\{ \kappa_{l\sigma} f_l^+(\epsilon) + \sum_{\tau'\sigma'} \kappa_{l\sigma'} f_l^-(\epsilon - E^{(\sigma')}_{(\sigma)}) \right\}. \qquad (2.59)$$

It is clear from this result that the broadening of the TDOS peak does depend on the lead configuration $\{\kappa_{l\sigma}\}$. Let the majority spins be polarized such that

$\sigma = +1$ in the layout with parallel lead polarization. The sum over the leads is then given by $\sum_l \kappa^{\mathrm{p}}_{l\sigma} = (1+\sigma P)/4$ and $\sum_l \kappa^{\mathrm{ap}}_{l\sigma} = (1+\sigma Pa)/4$ for parallel and anti-parallel polarizations, respectively. Let us first consider the case of zero effective Zeeman splitting, i.e., $E^{\sigma}_{\bar{\sigma}} = E^{(\bar{\sigma})}_{(\sigma)} = 0$. The difference of $\mathrm{Im}(\Sigma)$ for the two configurations then reads

$$\mathrm{Im}\left[\Sigma^{0,(\tau\sigma)}_{\mathrm{p}} - \Sigma^{0,(\tau\sigma)}_{\mathrm{ap}}\right] = \delta^{\mathrm{Im}} = \pi\frac{\gamma_0}{4}\sigma P(1-a)f^{+}(\epsilon). \tag{2.60}$$

Note that the validity of this result depends on the ratio of linewidth and level spacing, namely that $\gamma_0 \ll \varepsilon_0$ such that only the selected small set of charge fluctuations contribute. The sign of the difference in Eq. (2.60) is determined by σ, a result which is intuitively clear since the sum over the couplings will be greater for the spin-up transition ($\sigma = 1$) in the parallel case and for the spin-down transition in the anti-parallel one ($\sigma = -1$), as shown schematically in Fig. 2.6(a). The sum over the couplings determines the charge-fluctuation induced broadening of the peak that is associated with the given transition. Thus, for zero energy splitting $E^{(\bar{\sigma})}_{(\sigma)}$ we would expect a broadening of the peak associated with the transition $0 \rightleftarrows (\uparrow)$ for the parallel configuration and a broadening of the peak in G^{ap} for the transition $0 \rightleftarrows (\downarrow)$. Note, however, that the second effect will not be visible since the effective peak width and thus also the TMR ratio will be dominated by the spin up transition, i.e., by the prefactor of the rate in Eq. (2.48), irrespective of the broadening due to the charge fluctuations. Hence, we will observe a TMR signal as depicted in Fig. 2.6(b).

Now let us assume a non-zero effective Zeeman splitting $E^{\uparrow}_{\downarrow} = E_{\uparrow} - E_{\downarrow} = g\mu_{\mathrm{B}}h_{\mathrm{p/ap}}$ of states with quantum numbers $\sigma = \uparrow / \downarrow$. This splitting also depends on the magnetization state p (parallel) or ap (anti-parallel) of the contact electrodes. The energy difference is expressed in terms of the effective magnetic fields $g\mu_{\mathrm{B}}h_{\mathrm{p}}$ and $g\mu_{\mathrm{B}}h_{\mathrm{ap}}$. We assume that this field is non-zero for both polarizations. $\mathrm{Im}(\Sigma)$ as well as the TMR are very sensitive to the choice of the shifts, the couplings and the polarization.

We try to shed light on the double dip-like feature in the TMR graph, see Fig. 2.6(c). It can be observed for different parameter regimes, but for the sake of the argument it is sufficient to present one possible set. In our model the drain lead switches polarization upon interaction with external magnetic field while the density of states in the weakly coupled source contact remains unaltered. Given that the spin transport is more sensitive to the bottleneck (source) contact, it is plausible to assume that the shifts are such that the majority spins tunnel first on the quantum dot, namely spin up electrons in both configurations. These considerations favor a choice of negative shifts $g\mu_{\mathrm{B}}h_{\mathrm{ap}}, g\mu_{\mathrm{B}}h_{\mathrm{p}} < -k_{\mathrm{B}}T$. The second pair of resonances

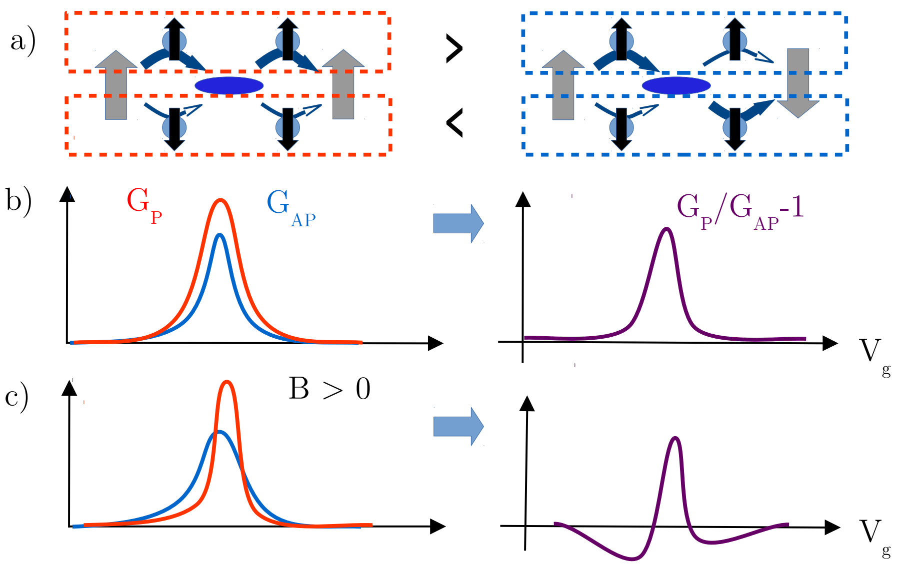

Figure 2.6: The influence of $\mathrm{Im}(\Sigma)$ on the TMR. a) Large gray arrows symbolize the majority spin in the left or right contact. The contributions to the self energy for one spin species are summed for each configuration of magnetized leads (parallel on the left, anti-parallel on the right) as indicated by the dashed frames. Weak (strong) coupling to the dot (blue ellipse) is given by thin (thick) arrows. Note that for the spin down species the sum over the leads yields a greater contribution in the configuration with anti-parallel polarization (as indicated by the signs between the dashed frames). b) On the left, we depict schematically the conductance peaks for one resonance in both parallel and anti-parallel configurations and the resulting TMR (right). The broadening of G_p is typically larger than for G_ap in the absence of stray fields. c) Due to a magnetic stray field, the contribution to $\mathrm{Im}(\Sigma)$ in the parallel case can be reduced, giving rise to a double dip structure in the TMR.

is then dominated by spin down electrons and the respective contributions $f^-(\epsilon + g\mu_\mathrm{B} h_\mathrm{p/ap})$ in Eq. (2.59) are suppressed. Conversely, for spin up electrons $f^-(\epsilon - g\mu_\mathrm{B} h_\mathrm{p/ap}) = 1$. In the resonant case, $|\epsilon| \lesssim k_\mathrm{B} T$, the imaginary part of the self-energy for the $|0\rangle \leftrightarrows |(\sigma)\rangle$ then reads

$$\delta^\mathrm{Im} \simeq -\pi \frac{\gamma_0}{4}(1-a)P(1-\sigma f^-(\epsilon)). \tag{2.61}$$

The magnitude of the relative broadening of the peak related to the transition of a spin down electron in G_ap is thus increased for higher polarization and $a \to -1$. Although this estimate is only valid in the direct vicinity of the resonance, it describes the situation qualitatively as can be seen in Fig. 2.7. We show conductance and TMR nearby the resonance $|0, n+1\rangle \rightleftarrows \{|(\sigma\tau), n+1\rangle\}$ for fields $g\mu_\mathrm{B} h_\mathrm{p} = -40\,\mu\mathrm{eV}$ and $g\mu_\mathrm{B} h_\mathrm{ap} = -80\,\mu\mathrm{eV}$. In the panels on the left side, the polarization is varied keeping $a = -0.8$ fixed. We see that the right shoulder in the TMR curve (c) is lifted upwards with increasing polarization. On the right panels in Fig. 2.7 we increase the coupling to the source contact which is proportional to a. While the conductance is decreased for asymmetric choices of a in both configurations (see (d) and (e)), the magnitude of the peak in G_ap is not symmetric with respect to the coupling to source and drain. This can be understood from the following argument: The effective Zeeman splittings prefer one spin species for a selected transition. When the spin-down species is favored, the tunneling in the *ap* configuration is enhanced with respect to the *p* configuration. We can further increase this difference when we increase the coupling to the contact with a flipped magnetization in the *ap* configuration. This is the effect of the asymmetry parameter a in Eq. (2.61). This effect is also reflected in Fig. 2.7(c): the shoulders for $a = 0.8$ turn into dips approaching $a = -0.8$. Please keep in mind that this discussion is simplified since we do not account for the fact that the relative position of the peaks changes, too, as we vary the parameters a and P.

2.3 Application to experimental data: TMR of a CNT quantum dot

Let us use the presented transport framework to model TMR data measured in 2012 by A. Prüfling and D. Steininger in the group of C. Strunk. The TMR is sensitive to modifications of the Coulomb peak position and linewidth depending on the magnetization of the leads. As we have shown in the previous two sections, the DSO can describe both effects as a result of charge fluctuation processes. It is therefore a suitable candidate to model the experimental data.

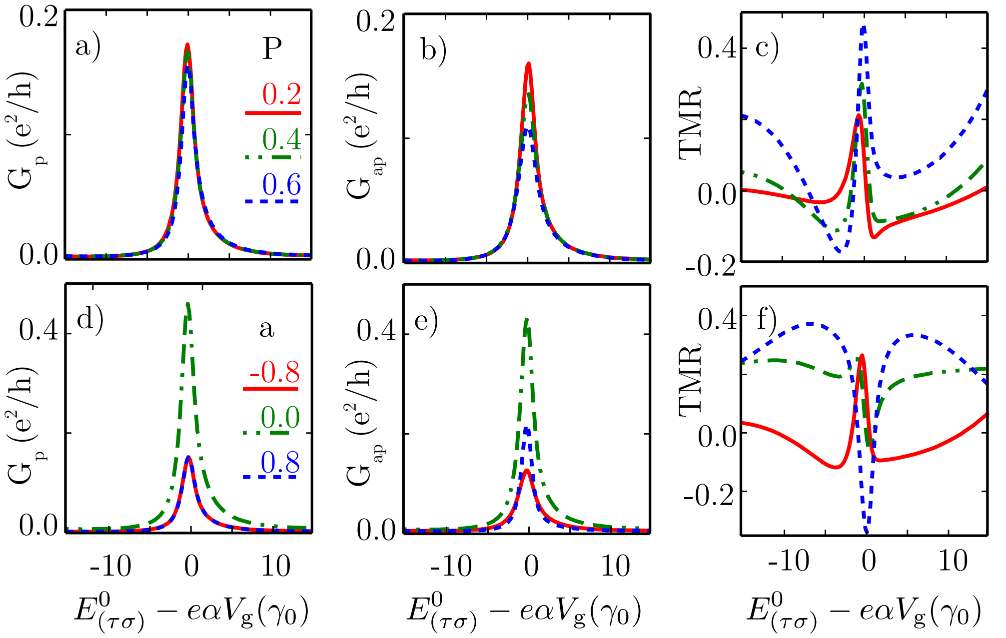

Figure 2.7: Conductance and TMR calculations in the vicinity of the resonance $|0, n+1\rangle \rightleftarrows \{|(\sigma\tau), n+1\rangle\}$ for different polarizations P (panels (a)-(c), $a = -0.8$) and coupling asymmetry a (panels (d)-(f), $P = 0.4$) applied in the parallel configuration for effective Zeeman splitting $g\mu_{\mathrm{B}}h_{\mathrm{p}} = -40\,\mu$eV and $g\mu_{\mathrm{B}}h_{\mathrm{ap}} = -80\,\mu$eV. (a),(b): Increasing the polarization reduces the peak width and height of both G_{p} and G_{ap}. (c): In the TMR curve, the shoulder on the left at $P = 0.2$ is shifted to the right for $P = 0.6$. (d),(e): The coupling asymmetry $a \neq 0$ (Eq. (2.42)) diminishes the peak heights of the conductance for both configurations of the leads. Note that in the anti-parallel case shown in (e) the symmetry between the contacts is broken and the peak height is sensitive to the variation of the dominating coupling. (f): The TMR curve exhibits a double dip feature for values $-1 \lesssim a < 0$. It is transformed to a double peak for $0 < a \lesssim 1$. All plots are calculated at a temperature corresponding to $40\,\mu$eV and a coupling $\gamma_0 = 160\,\mu$eV.

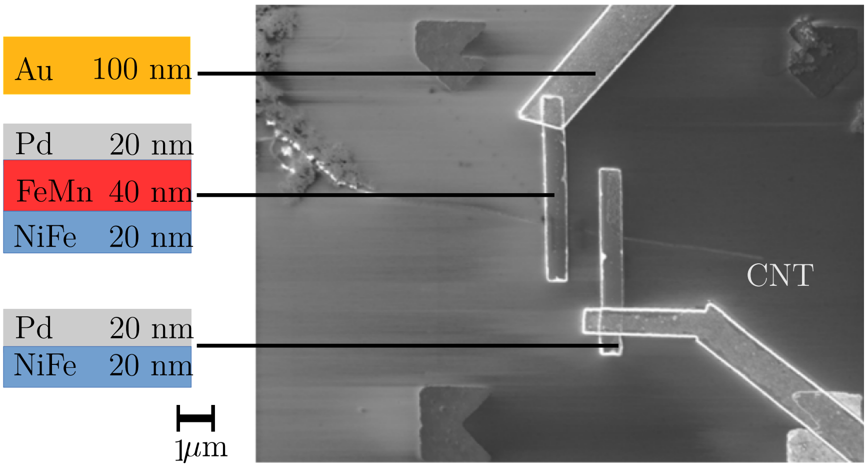

Figure 2.8: SEM picture of a chip structure similar to that of the measured device. A carbon nanotube on a positively doped silicon substrate capped with 500 nm SiO_2 is contacted by two permalloy (NiFe) stripes, one of which is exchange-biased by a FeMn layer. On top, the stripes are protected by palladium. Gold is used for the bond pads and the connections to the nanotube contacts.

2.3.1 Experiment

Sample preparation

For the purpose of measuring TMR in CNTs, one needs to interface the nanotube to two ferromagnetic contacts with a different switching field. The conductance, being sensitive to the magnetization in the leads, changes when the polarization of one of the contacts is reversed by an external magnetic field. It has been shown that NiFe is well suited as a material for the electrodes of CNT spin-valves [78]: the alloy shows a distinct switching behavior as a function of the applied magnetic field and the interface transparency between NiFe and the CNT is comparable to that of Pd. The structure of one of the devices we realized for this purpose is shown in Fig. 2.8. On an oxidized silicon substrate (500 nm SiO_2) a carbon nanotube is grown by chemical vapor deposition. The nanotube is located by atomic force microscopy and two NiFe (80:20) leads, 20 nm in thickness, are deposited at a distance of 1 μm on top of the nanotube by sputtering. On one of the two contacts, 40 nm of anti-ferromagnetic FeMn (50:50) is sputtered to bias the magnetization of the underlying NiFe contact. The hysteresis loop of this contact is expected to be shifted with respect to the pure NiFe contact by virtue of the exchange

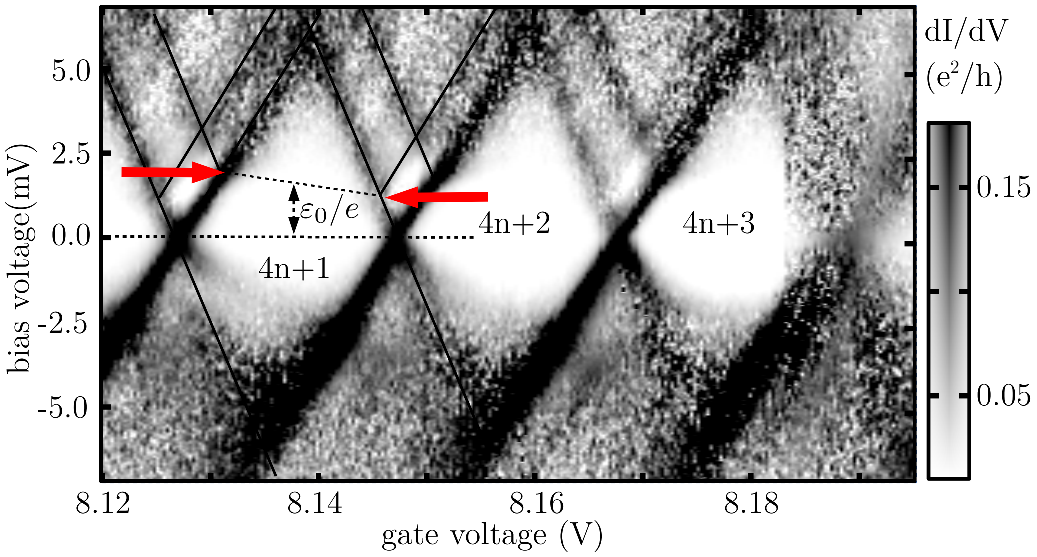

Figure 2.9: Differential conductance versus bias and gate voltage of a selected region measured at 300 mK and $B = 0$. The numbers in the Coulomb blockade regions denote the number of electrons in shell n on the quantum dot. Arrows indicate the first excited state crossing the source (left) and drain (right) lines in the vicinity of the state with one extra electron ($N = 4n + 1$). As guides to the eye, lines emphasize the lines in the stability diagram that correspond to the lines in Fig. 2.5.

bias effect [79]. A 20 nm protective layer (Pd) covers the leads from the top. The switching of the exchange biased contacts was confirmed independently prior to the measurement using SQUID and vibrating sample magnetometer techniques.

2.3.2 Measurement

An electronic characterization of the quantum dot at 300 mK and at zero magnetic field shows a regular Coulomb blockade behavior, see Fig. 2.9. From this data we extract the gate conversion factor $\alpha = 0.29$ and the charging energy $E_c = 6.1$ meV (see Eq. (2.39)). The sample does not exhibit a clear four-fold symmetry in the peak height or peak spacing as expected for a carbon nanotube quantum dot from its non-interacting single-particle spectrum. Consequently, we are not able to label the Coulomb blockade regions with a value of the electronic shell filling n in a definite way. The assignment of the number of electrons to the experimental data in Fig. 2.9 is done in agreement with the theoretical predictions.

Having a closer look at Fig. 2.9, we can identify an excited state transition at $eV_{\mathrm{b1}} \sim 1.8\,\mathrm{meV}$ parallel to the drain line (left arrow) and at $eV_{\mathrm{b2}} \sim 1.4\,\mathrm{meV}$ (cf. Fig. 2.5) parallel to the source line (right arrow). The value for the un-renormalized excitation energy is given by the mean value, $\varepsilon_0 \simeq 1.6\,\mathrm{meV}$. The energy scale of this excitation stays approximately constant over a range of at least six resonances, as can be seen from measurements over a broader gate range. From the mean level spacing ε_0 of the quantized levels $\varepsilon(n)$ we estimate the size of the quantum dot L, $\varepsilon_0 = \varepsilon(n+1) - \varepsilon(n) \propto \pi\hbar v_{\mathrm{F}}/L$. It is thus reasonable to identify the first excitation with the confinement energy ε_0 equivalent to a lateral confinement of $1\,\mu\mathrm{m}$ for a Fermi velocity of $800\,\mathrm{km/s}$ [38], a value that agrees with the contact spacing of $\sim 1\,\mu\mathrm{m}$. The asymmetry of the line spacing with respect to source and drain suggests a gate-dependent renormalization [77] of the CNT many-body addition energies in the presence of ferromagnetic contacts. We show in Sec. 2.2.3 that this can be a direct consequence of charge fluctuations in the presence of contact magnetization.

Electron transport measurements at $300\,\mathrm{mK}$ show a significant switching behavior. In Fig. 2.10(a) the conductance across the CNT quantum dot is plotted as a function of the gate voltage and the magnetic field directed parallel to the stripes, i.e., along their easy axis, as indicated in the inset to the figure. Note that the colorbar on the right only covers a small range of low conductance values to make the switching event visible as a step in the conductance (marked by the dotted grey line).

We focus on a single B-field trace, Fig. 2.10(b), marked by a red dashed line in (a). The step in the signal can be interpreted as the magnetization reversal of the contacts: Sweeping the magnetic field from negative ($-100\,\mathrm{mT}$) to positive values, one of the contacts switches at $B = B_{\mathrm{s,u}}$, resulting in a configuration with anti-parallel polarization of the majority spins of the two contacts. This results in a drop of the conductance signal. Upon increasing the field further, the second contact is supposed to switch and the conductance should recover. The second switching event was not observed in the present sample. Sweeping back from positive to negative field, the conductance recovers at $B_{\mathrm{s,d}}$. The two values $B_{\mathrm{s,d/u}}$ characterize a hysteresis loop with a coercive field $B_{\mathrm{c}} = B_{\mathrm{s,u}} - B_{\mathrm{s,d}}$ and an exchange bias $B_{\mathrm{ex}} = (B_{\mathrm{s,u}} + B_{\mathrm{s,d}})/2$. At $B = 0$ the two contacts are always in a parallel configuration, because the coercive field of the switching contact is smaller than the exchange bias.

Fast and slow measurements Measurements of the conductance performed at constant magnetic field require $\Delta t^{\mathrm{fast}} \sim 100\,\mathrm{ms}$ per data point

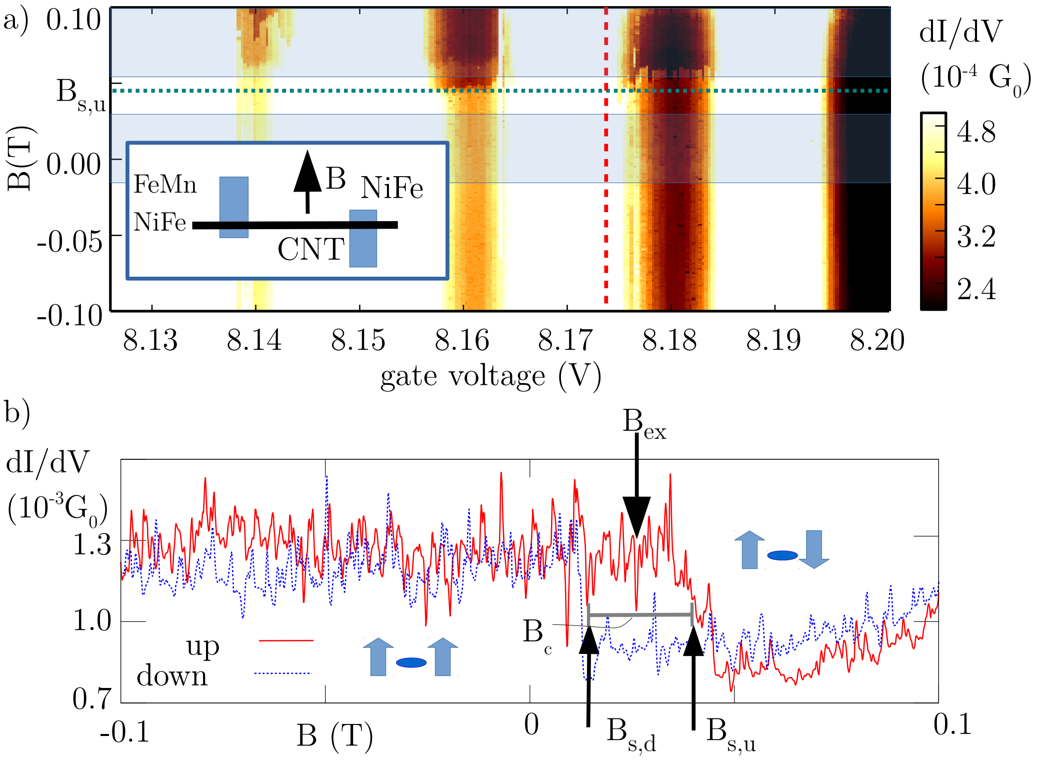

Figure 2.10: (a) Differential conductance as a function of gate voltage and magnetic field at $V_\mathrm{b} = 0$ and $T = 300\,\mathrm{mK}$. A dotted horizontal line highlights the switching of the conductance due to the reversal of the magnetization in the contacts. Note that the data is recorded for increasing magnetic field sweeps (up-sweeps). To extract the TMR, the conductance is averaged over parts of the magnetic field range indicated by the shaded areas below and above $B_\mathrm{s,u}$. Inset: Orientation of the external field B with respect to the CNT and the leads. (b) Differential conductance plotted versus magnetic field at $V_\mathrm{g} = 8.1737\,\mathrm{V}$ (marked by a dashed green line in (a)). The solid red curve was recorded with increasing field, the dashed blue curve with decreasing field. Small pictograms indicate possible orientations of the majority spins in the contacts. The switching of one of the two contacts at $B_\mathrm{s,u/d}$ is highlighted with arrows at the bottom for both sweep directions. The coercive field is indicated by B_c and the exchange bias by B_ex.

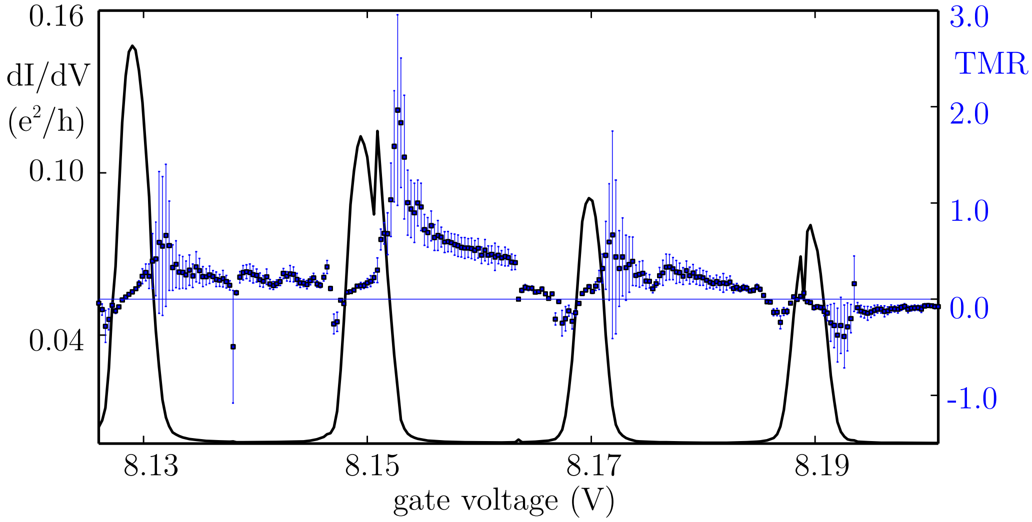

Figure 2.11: Differential conductance and TMR as a function of gate voltage measured over four resonances (*slow* measurement, see text). The conductance is measured at parallel polarization of the contacts. The TMR graph shows a dip-peak sequence over the first two resonances and a qualitatively different double-dip feature at the last two.

and will be called the *fast* measurements in the following. Contrarily, in *slow* measurements, each conductance data point is obtained from magnetic field sweeps with a duration of $\Delta t^{\mathrm{slow}} \sim 20$ minutes at constant gate voltage (compare Fig. 2.10(b)). We then identify B_{s} from a step in the conductance signal and take the average over 100 points on either side of the step to extract the conductance in the parallel and anti-parallel configuration, respectively. This is repeated for 250 values of the backgate potential in the range between 8.126 V and 8.201 V, see the shaded grey area in Fig. 2.10(a). In Fig. 2.11, the TMR as a function of gate voltage is shown together with the conductance at parallel contact polarization. In this *slow* measurement, we obtain conductance peaks with a height of $0.15e^2/h$ and a full width at half maximum (FWHM) of $\Gamma \sim 0.7$ meV. Comparing these values to a height of $0.3e^2/h$ and a width of 0.4 meV obtained from the *fast* measurement at $B = 0$ we conclude that the peak conductance in the data from the *slow* measurement is substantially suppressed. We will discuss this deviation in Sec. 2.3.3. It is remarkable that besides huge positive (180%) TMR values, negative regions occur prior to the peak in the TMR curve in the first two resonances while for the last two the value drops again, forming two dips in sequence. Again this will be discussed in more detail in Sec. 2.3.3.

2.3.3 Comparison between experiment and model output

Conductance in the experiment and in the model

In Fig. 2.12(a) (blue crosses) we show the conductance $G_{\mathrm{p}}^{\mathrm{fast}}$ obtained at $B = 0$ performing a *fast* measurement, i.e., sweeping the gate voltage V_{g} at zero bias voltage, see Sec. 2.3.2. Note that it provides only conductance data for the parallel configuration (compare Fig. 2.10). The data from this measurement yields conductance peaks that fit to Lorentzian curves with an average FWHM of 0.3 meV. Adapting our model parameters to the data of $G_{\mathrm{p}}^{\mathrm{fast}}$, we obtain the continuous lines in Fig. 2.12. The conductance data from the *slow* measurement (compare Sec. 2.3.2) for the two configurations, $G_{\mathrm{p}}^{\mathrm{slow}}$ and $G_{\mathrm{ap}}^{\mathrm{slow}}$, are also shown in Fig. 2.12 (green circles).

The shape of the conductance peaks turns out to be non-Lorentzian, with the peak height in the conductance data limited to $\sim 0.1\,\mathrm{e}^2/\mathrm{h}$. While the flanks of the peaks match for the first three resonances in the data from the slow and from the fast measurement[3], the maximum conductance values deviate by a factor of three. So far no full explanation for the suppression of the peak conductance was found.

Model parameters

A bare coupling of $\gamma_0 = 80\,\mu\mathrm{eV}$ is found to optimize the fit to $G_{\mathrm{p}}^{\mathrm{fast}}$. The thermal energy is chosen as $k_{\mathrm{B}}T = 40\,\mu\mathrm{eV}$ (460 mK), close to the base temperature (300 mK). For the quantum dot parameters we set $E_c = 6.1\,\mathrm{meV}$ and a shell spacing $\varepsilon_0 = 1.4\,\mathrm{meV}$ as inferred from Sec. 2.3.2. The shell number $n \sim 40$ is estimated from the distance to the band-gap. We assume asymmetric contacts with $a = -0.7$ and polarization $P = 0.4$. For the calculation of the charge fluctuations we include all states within an energy interval of $3\varepsilon_0$ (see Sec. 2.C in the appendix). The effective Zeeman shifts for the model output in Fig. 2.12 are $g\mu_{\mathrm{B}}h_{\mathrm{p}} = -0.12\,\mathrm{meV}$ and $g\mu_{\mathrm{B}}h_{\mathrm{ap}} = -0.16\,\mathrm{meV}$.

Discussion

The effective Zeeman splitting The conductance data in Fig. 2.11 does not reflect particle-hole symmetry. If only features of the leads density of states at the Fermi energy are included, compare Eq. (2.41), the DSO preserves particle-hole symmetry at zero bias by construction [57]. To break

---

[3] There is a deviation between $G_{\mathrm{p}}^{\mathrm{fast}}$ and $G_{\mathrm{p}}^{\mathrm{fast}}$ in Fig. 2.12(a) at the right flank of the second resonance at $V_{\mathrm{g}} = 8.15\,\mathrm{V}$ due to jump in the gate voltage during the measurement.

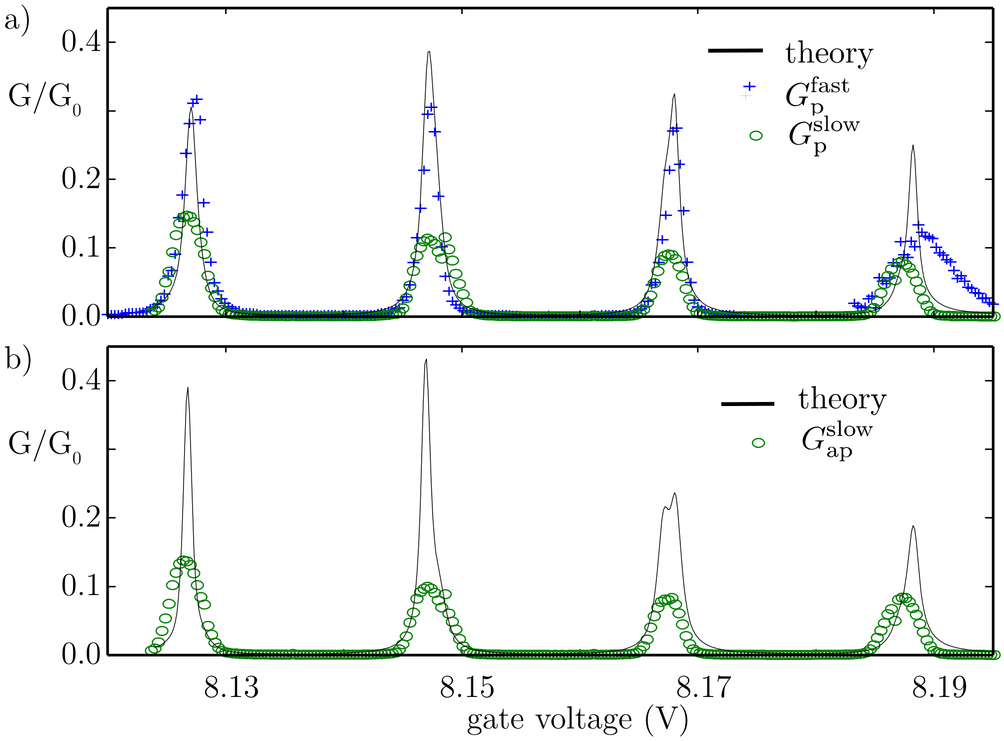

Figure 2.12: Conductance at zero bias as a function of gate voltage V_{g} plotted for (a) parallel and (b) anti-parallel polarization of the leads. In (a), a gate trace ($G_{\mathrm{p}}^{\mathrm{fast}}(V_{\mathrm{g}})$, blue circles) is shown together with conductance obtained during TMR measurements $G_{\mathrm{p}}^{\mathrm{slow}}(B, V_{\mathrm{g}})$ (green crosses, see also Fig. 2.11), and the calculated conductance for parallel lead polarization (continuous line, black) at $k_{\mathrm{B}}T = 40\,\mu\mathrm{eV}$, $\varepsilon_0 = 1.4\,\mathrm{meV}$, $E_c = 6.1\,\mathrm{meV}$, $a = -0.7$, $P = 0.4$, $g\mu_{\mathrm{B}}h_{\mathrm{ap}} = -0.16\,\mathrm{meV}$ and $g\mu_{\mathrm{B}}h_{\mathrm{p}} = -0.12\,\mathrm{meV}$. In the vicinity of the rightmost resonance, $G_{\mathrm{p}}^{\mathrm{fast}}$ shows a high noise level (compare also Fig. 2.9). (b) The conductance data measured for anti-parallel polarization of the contacts $G_{\mathrm{ap}}^{\mathrm{slow}}(B, V_{\mathrm{g}})$ (green crosses) is compared to the model output (continuous line, black) for the same parameters as in (a).

this symmetry effective Zeeman fields, $\hat{\mathrm{H}}_{\mathrm{ext}}^{\mathrm{P/A}} = \sigma g \mu_{\mathrm{B}} h_{p/ap}/2$ (cf. Eq. (2.39)) have to be included [75]. The labels p and ap refer to the parallel and anti-parallel configuration of the contact magnetization. Furthermore, the Zeeman splittings increase the magnitude of the TMR effect. The large TMR values observed in our experiment, Fig. 2.11, can not be reproduced without applying unrealistically high values for the polarization or extreme values for the contact asymmetry.

While it is evident that the splittings are a necessary ingredient in addition to the incorporation of the charge fluctuations to fit the experimental data, the origin of the splittings is not clear. A corresponding stray field would have to provide $\sim 1\,\mathrm{T}$. In Ref. [73], the effective Zeeman fields are used to model the effects of coherent reflections at the magnetic interfaces (SDIPS) in a double barrier systems [73]. This concept appears also In Ref. [80], where the effective Zeeman splittings are used in conjunction with the *equation of motion* technique to explain the experimental TMR data of Ref. [73]. The splittings used in Ref. [80], $g\mu_{\mathrm{B}} h_{\mathrm{p}} = 0.25\,\mathrm{meV}$ and $g\mu_{\mathrm{B}} h_{\mathrm{ap}} = 0.05\,\mathrm{meV}$, are of similar magnitude when compared to our values.

The renormalization of the excited states The shift of the excited state line in the first diamond due to charge fluctuations described in Sec. 2.2.3 is of the order $2\gamma_0 \simeq 0.2\,\mathrm{meV}$ using the same parameters as for the fit in Fig. 2.12. This is a reasonable value when compared to the value extracted from the experiment, $eV_{\mathrm{b1}} - eV_{\mathrm{b2}} \simeq 0.4\,\mathrm{meV}$ (cf. Sec. 2.3.2).

TMR From the conductance traces calculated within our model, Fig. 2.12 (continuous lines), the TMR, Fig. 2.13, is obtained. The data and the model calculation agree in the decay of the TMR amplitude within a sequence of four charging states including the "double dip" feature in the last two resonances at $V_{\mathrm{g}} = 8.17\,\mathrm{V}$ and $V_{\mathrm{g}} = 8.19\,\mathrm{V}$. This indicates that the sequence in Fig. 2.12 represents one shell, i.e., charging states $4n+1$ to $4(n+1)$. We note that in the model output the last resonance is dominated by a peak while the dips are more prominent in the experimental data.

In the vicinity of all conductance peaks (at $V_{\mathrm{g}} = 8.13\,\mathrm{V}$, $V_{\mathrm{g}} = 8.15\,\mathrm{V}$, $V_{\mathrm{g}} = 8.17\,\mathrm{V}$ and $V_{\mathrm{g}} = 8.19\,\mathrm{V}$) an additional small shoulder around $\mathrm{TMR} = 0$ occurs in the data of Fig. 2.12(c). These shoulders are likely related to the aforementioned suppression of the peak conductance in the *slow* measurement (see Fig. 2.12(a,b)). We recall that the TMR is calculated from the ratio $G_{\mathrm{p}}/G_{\mathrm{ap}}$ (compare also Fig. 2.6): in the regions where the peaks are cut off, the ratio $G_{\mathrm{p}}^{\mathrm{slow}}/G_{\mathrm{ap}}^{\mathrm{slow}}$ is smaller than it is in the same region in the model output, where steep peak flanks lead to a larger ratio $G_{\mathrm{p}}/G_{\mathrm{ap}}$.

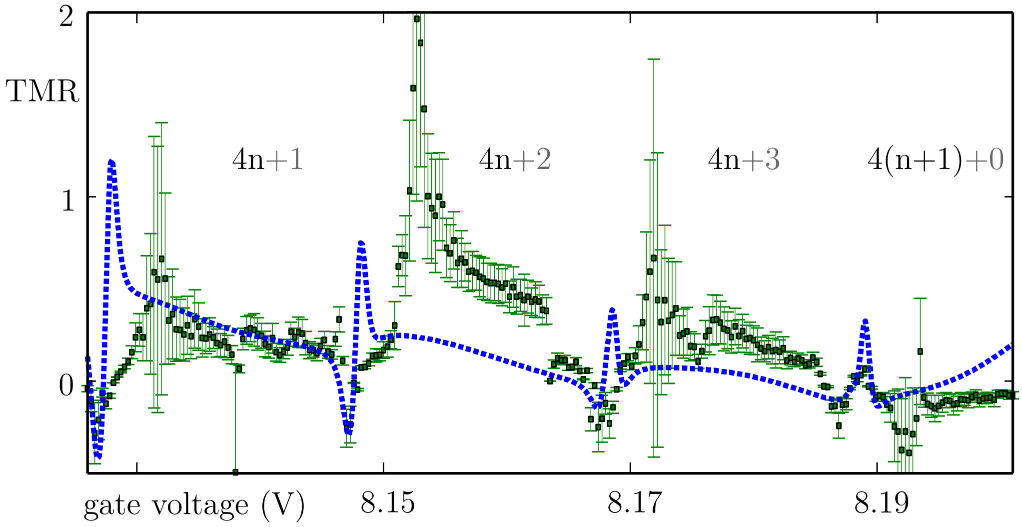

Figure 2.13: Experimental TMR data (green dots) calculated from $G_{\mathrm{p}}^{\mathrm{slow}}$, Fig. 2.12(a)(green circles), and $G_{\mathrm{ap}}^{\mathrm{slow}}$, Fig. 2.12(b) (green circles), (also shown in Fig. 2.11) plotted together with TMR obtained from the model conductance (blue dashed line), i.e., from the data shown in Fig. 2.12.

Spin-orbit coupling In case of non-zero spin-orbit coupling [14, 16], we would expect a splitting of the excited state lines in the stability diagram in Fig. 2.9. This is not resolved in our experimental data. For simplicity we therefore here assume $\Delta_{\mathrm{SO}} = 0$. Model calculations with non-zero spin orbit coupling can be found in the appendix, Sec. 2.E.

2.4 Summary & Outlook

In this first part of the work we study a carbon-nanotube based quantum dot with ferromagnetic leads. To model the data we introduce and apply the dressed second-order (DSO) framework based on the reduced density matrix formalism. The selected infinite set of contributions to the self energy accounts for charge fluctuations between the quantum dot and the ferromagnetic contacts. Thereby, we establish a theory for transport through carbon nanotube quantum dots in the weak and intermediate coupling regime that goes beyond the sequential tunneling approximation which can only account for a positive and gate-independent TMR. We demonstrate that the charge fluctuation processes, summed to all orders in the coupling to the leads, yield tunneling rates where the Lamb shift and the broadening of the resonances are given by the real and imaginary parts of the self energy, respectively. We explicitly compare the DSO self energy for different contact magnetizations and show that the DSO modeling can account both for the renormalization of excited states and the specific structures observed in the TMR gate dependence. Eventually we use our model to interpret experimental TMR data and state a qualitative agreement.

Future efforts should be put in obtaining clean TMR data from CNTs on the experimental side. Ferromagnetic materials that withstand the conditions of the chemical-vapor-deposition process would enable TMR measurements on ultra-clean carbon nanotubes. Alternatively, a stamping approach (as presented in Ref. [81]) would allow to freely choose the contact material. On the theoretical side, the understanding of the addition energy spectrum and, consequently, the design of the single particle Hamiltonian can still be improved to ultimately fit TMR data recorded over greater ranges of charging states.

Appendix

2.A Transformation of Eq. (2.22) to the Schrödinger picture

Recall that

$$\hat{\rho}_{\mathrm{red}}(t) = \hat{\mathrm{U}}_0^{\dagger}(t)\, \hat{\rho}_{\mathrm{red,S}}(t)\, \hat{\mathrm{U}}_0(t),$$

which immediately yields the relation between the time derivative in both pictures:

$$\dot{\hat{\rho}}_{\mathrm{red,S}}(t) = \hat{\mathrm{U}}_0(t)\, \dot{\hat{\rho}}_{\mathrm{red}}(t)\, \hat{\mathrm{U}}_0^{\dagger}(t) - \frac{\mathrm{i}}{\hbar}[\hat{\mathrm{H}}_S, \hat{\rho}_{\mathrm{red,S}}(t)]. \tag{2.62}$$

We insert Eq. (2.20) into the first term of this expression and end up with

$$\begin{aligned}\dot{\hat{\rho}}_{\mathrm{red}}(t) = {} & -\frac{\mathrm{i}}{\hbar}[\hat{\mathrm{H}}_S, \hat{\rho}_{\mathrm{red}}(t)] \qquad (2.63)\\ & - \sum_{ij,p} \frac{1}{\hbar^2} \int_0^t \mathrm{d}t'' \Big\{ [\hat{\mathrm{S}}_i^{p}, \hat{\mathrm{U}}_0(t'')\, \hat{\mathrm{S}}_j^{\bar{p}}\, \hat{\rho}_{\mathrm{red}}(t-t'')\, \hat{\mathrm{U}}_0^{\dagger}(t'')] \Big\langle \hat{\mathrm{E}}_i^{\bar{p}}(t'')\, \hat{\mathrm{E}}_j^{p} \Big\rangle_E \\ & \qquad - [\hat{\mathrm{S}}_i^{\bar{p}}, \hat{\mathrm{U}}_0(t'')\, \hat{\rho}_{\mathrm{red}}(t-t'')\, \hat{\mathrm{S}}_j^{p}\, \hat{\mathrm{U}}_0^{\dagger}(t'')] \Big\langle \hat{\mathrm{E}}_j^{p}\, \hat{\mathrm{E}}_i^{\bar{p}}(t'') \Big\rangle_E \Big\}, \qquad (2.64)\end{aligned}$$

where all operators are in the Schrödinger picture (except the ones in the bath) and we performed the variable transformation

$$\int_0^t \mathrm{d}t' \;\to -\int_t^0 \mathrm{d}(t-t') \;\equiv \int_0^t \mathrm{d}t''$$

on Eq. (2.22). The time convolutive form is clearly visible.

2.B Fabrication parameters of CB3224

The sample was fabricated by P. Stiller and D. R. Schmid from the group of A. K. Hüttel at the University of Regensburg. The fabrication process is similar to the process described in Sec. 4.D. Further details can be found in the thesis of D. R. Schmid, Ref. [17].

- optical lithography
  - positive photo-resist Shipley 1805, spin-coated at 4500 rpm for 30 s, baked for 2 min at 90° C
  - UV exposure for 33 s
  - developement in NaOH/H_2O (1 : 3) for 40 s
- electron beam lithography
  - PMMA 200 k3.5%, spin-coated 3000 rpm (5 s) / 8000 rpm (30 s), baked for 6 min at 150° C.
  - EBL accl. volt. 25 kV, aperture 30 μm, area dose 195 μC/cm^2
  - development in MIBK / iso-propanol (1:3) for 2 min
- metallization with 40 nm of Re (1.6 Å/s)
- reactive ion etching
  - CHF_3 at 17 nm/min for 360 s (50 sccm gas flow, 55 mTorr pressure, 150 W RF power)
  - Ar at 8 nm/min for 30 s (40 sccm gas flow, 30 mTorr pressure, 150 W RF power)
- catalyst deposition
  - EBL process with PMMA 200 k3.5% and 300 μC/cm^2 exposure dose at 25 kV
  - catalyst depostition
  - PMMA baked for 6 min at 150° C
  - lift-off in 60° C acetone
- CNT growth
  - rinse quartz tube with methane, hydrogen and argon

- heat to 900° C under argon atmosphere (1500 sccm)
- growth of CNT with 700 sccm hydrogen and 800 sccm methane for 10 min
- cooldown under argon (1500 sccm) and hydrogen (700 sccm) atmosphere

2.C Contribution of other excited states to the renormalization

When we discuss the effect of the charge fluctuations in Sec. 2.2.3 and Sec. 2.2.4 of the main text, we always focus on the most resonant transitions (see Fig. 2.4) that are energetically favorable, i.e., on transitions in Eq. (2.53) with an energy difference $E_{a/c'}^{c'/b}$ of the order of the effective line-width or below. At zero bias this is the largest available energy scale in the system. Nevertheless it is interesting to see how the outcome is affected by increasing the bandwidth and allowing excited states of the neighboring shells to contribute to the charge fluctuation channels. In terms of an effective energy shift in a multi-level quantum dot the renormalization due to excited states was also discussed in Ref. [75]. To illustrate the effect of such a modification we plot the real and imaginary parts of the self energy Σ in the vicinity of the transition $|(K\downarrow), n\rangle \rightleftarrows |\cdot, n+1\rangle$ for different sets of charge fluctuations within energy ranges of γ_0, ε_0, $2\varepsilon_0$ and $3\varepsilon_0$ in Fig. 2.C.1. We clearly see that the fluctuations from higher shells manifest themselves in additional features in the curves for $\mathrm{Re}(\Sigma)$, Fig. 2.C.1 (a,b), and $\mathrm{Im}(\Sigma)$, (c,d). Note, however, that the zero-bias conductance in our system is only sensitive to a small vicinity of a few $k_{\mathrm{B}}T$ around the resonance. Within this range the high energy contributions do not change the picture substantially. The analysis of the imaginary part in Sec. 2.2.4 is thus exact at the level of the self energy since the Fermi functions in the imaginary part suppress contributions from other shells.

2.D Calculation of $\mathrm{Re}(\Sigma)$

In this section we perform the calculation of $\mathrm{Re}(\Sigma^{1'0}) - \mathrm{Re}(\Sigma^{10})$ as part of the quantity δ_1 introduced in Sec. 2.2.3 of the main text. To this extent we analyze the renormalization of the energy difference $E_1^{1'}$ due to charge fluctuations to and from states $0 = |0; n\rangle$, $1 = |K\uparrow; n\rangle$ and $1' = |[K\uparrow]; n\rangle$ in more detail. We recall that the real part of the self energy related to a charge

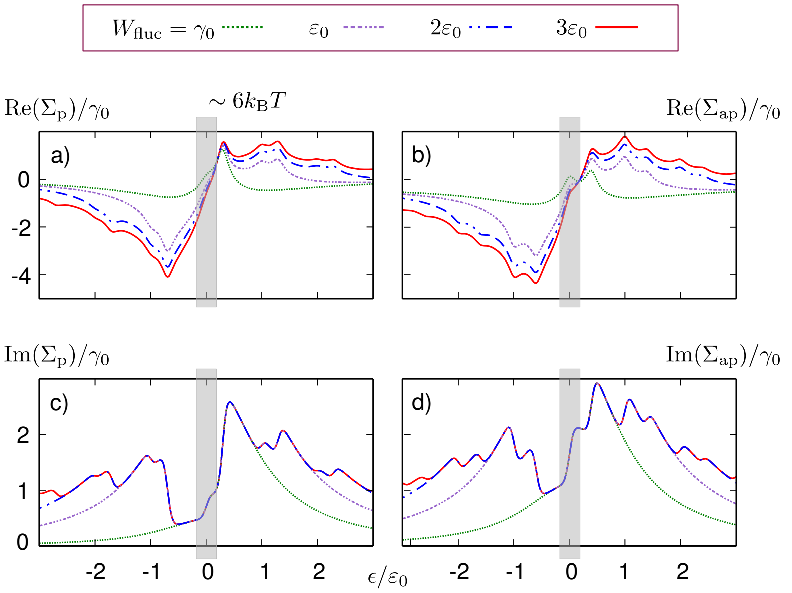

Figure 2.C.1: (Color online) Re(Σ) (a,b) and Im(Σ) (c,d) for both lead configurations as a function of energy ϵ in units of the shell spacing ε_0. Different lines are plotted for bandwidth $W_{\mathrm{fluc}} = \gamma_0$ (green, dotted) to $3\varepsilon_0$ (red, continuous) in steps of ε_0. In the vicinity of a few $k_{\mathrm{B}}T$ around the resonance ($\epsilon = 0$, gray region) the difference between the graphs for the real part (a,b) is small and for the imaginary part (c,d), it is vanishing.

fluctuation to state c' has the form (see. Eq. (2.53))

$$-\sum_l \gamma_l^{c'(b/a)}(\epsilon)\bar{\Psi}^0_{\mathrm{R}}(\mu_l \pm p(E^{c'/b}_{a/c'} - \epsilon)),$$

where we have to replace $b = 1'$, $a = 0$ or $b = 1$ and $a = 0$, respectively. Note that the contribution $\propto \bar{\Psi}^{(0)}(W)$ in Eq. (2.53) does not appear explicitly since it cancels in the difference of the shifts. Next, we have to find all states c' that contribute within our resonant approximation. We can immediately discard states that can be reached by in-tunneling from b and by out-tunneling from a, since their energy differences $E^{c'/b}_{a/c'}$ are of the order of the charging energy and thus beyond our charge fluctuation bandwidth of $W_{\mathrm{e}} = \max(eV_{\mathrm{b}}, k_{\mathrm{B}}T, \gamma_0) = \varepsilon_0/2$. We are left with states that can be reached by in-tunneling into state a and by out-tunneling from state b. Let us discuss one example for the state $1'$. There is one electron in the shell $n+1$ (denoted by the brackets [...] in the state ket) which can tunnel out and we are left with a state $|\cdot, n\rangle$. Actually this state is identical to the state 0 on the other contour, thus $E_0^{c'=0} = 0$. We can now evaluate the argument of the digamma function, i.e., $\mu_l - E^0_0 + \epsilon$, for $\epsilon = 0$. Since $\mu_{\mathrm{s/d}} = \pm\varepsilon_0/2$ and thus $|\mu_l| \leq W_{\mathrm{e}}$, we have to sum over both leads. The total contribution from fluctuations to $c' = 0$ is thus $-\gamma_0 \sum_l \kappa_{l\uparrow}\bar{\Psi}^0_{\mathrm{R}}(\varepsilon_0/2)$. The other states that can be reached by out-tunneling, e.g., $|(K\uparrow), [K\uparrow], n\rangle$, yield energy differences of at least $3/2\varepsilon_0 > W_e$. Using similar arguments we can collect all relevant contributions to the difference $\mathrm{Re}(\Sigma^{1'0}) - \mathrm{Re}(\Sigma^{10})$. In a graphical representation, this can be visualized as

$$\mathrm{Re}(\Sigma^{1'0}) - \mathrm{Re}(\Sigma^{10}) =$$

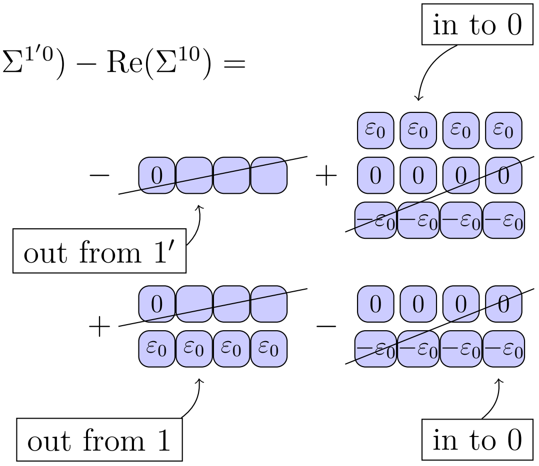

$$= 2\bar{\kappa}_{\mathrm{s}}\bar{\Psi}^0_{\mathrm{R}}(\varepsilon_0/2)$$

where one set of four boxes symbolizes one shell and we use $E^{c'/b}_{a/c'}$ as a label. Fluctuations that cancel are crossed out. Note that for excited states with an energy difference $E^{c'/b}_{a/c'} = \pm\varepsilon_0$ we add only the contribution from the source(drain) contact

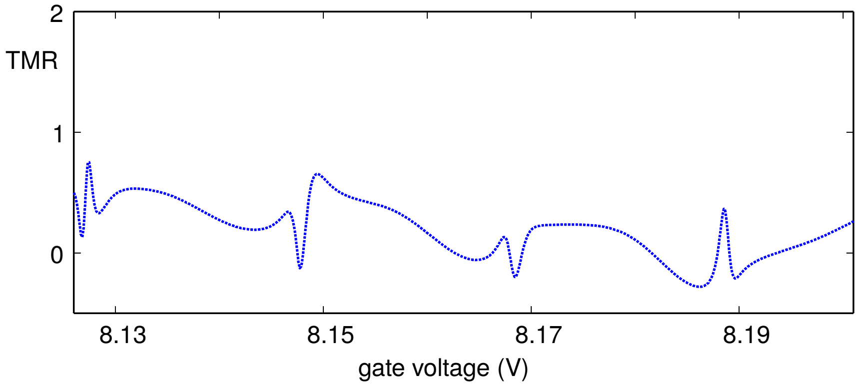

Figure 2.E.1: TMR as a function of gate voltage for orbital polarization $P_{\mathrm{orb}} = 0.6$, orbital shifts $g_{\mathrm{orb}}\mu_{\mathrm{orb}}h^{\mathrm{orb}}_{\mathrm{ap}} = -80\,\mu\mathrm{eV}$ and $g_{\mathrm{orb}}\mu_{\mathrm{orb}}h^{\mathrm{orb}}_{\mathrm{p}} = -40\,\mu\mathrm{eV}$, and $\Delta_{\mathrm{SO}} = 0.1\,\mathrm{meV}$ at $k_{\mathrm{B}}T = 40\,\mu\mathrm{eV}$. The other parameters are identical to the ones used in Fig. 2.12.

where $|\mu_l - E^{c'/b}_{a/c'}| < W_{\mathrm{e}}$. Similarly we find

$$\mathrm{Re}(\Sigma^{21}) - \mathrm{Re}(\Sigma^{21'}) = (1 + \bar{\kappa}_{\mathrm{d}} - \bar{\kappa}_{\uparrow} + \bar{\kappa}_{\downarrow})\bar{\Psi}^{0}_{\mathrm{R}}(\varepsilon_0/2),$$

which leaves us with δ_1 from Eq. (1.12).

2.E Spin-orbit coupling and valley polarization

In Sec. 2.2.1 we discussed the possibility to include spin-orbit interaction effects, as they have been reported to play a prominent role in carbon nanotubes [14, 82]. However, we did not add it in the comparison to the experimental data since they could not be resolved in the transport spectrum (Fig. 2.9). Nevertheless, values of the order of $\Delta_{\mathrm{SO}} \sim 100\,\mu\mathrm{eV}$ would still be consistent with the experimental data. Introducing a finite Δ_{SO} a priori does not affect the TMR as the Kramers pairs are spin degenerate pairs with anti-parallel and parallel alignment of spin and valley magnetic moments. Yet it has been argued that the two valleys of a CNT can couple differently to the leads [83]. If the valley quantum number is conserved upon tunneling, the mechanism can be understood in terms of a valley polarization. A possible tunneling Hamiltonian that describes this situation can be written as

$$\hat{\mathrm{H}}_{\mathrm{T}} = \sum_{l\mathbf{k}n\sigma\tau} T_{l\mathbf{k}n\sigma\tau} d^{\dagger}_{n\sigma\tau} c_{l\mathbf{k}\sigma} + \mathrm{h.\,c.}, \tag{2.65}$$

with a valley dependent coupling $T_{l\mathbf{k}n\sigma\tau}$ and an operator $c_{l\mathbf{k}\tau\sigma}$ that describes the electrons in the leads (that are also part of the CNT). Including a valley polarization in turn also renders the TMR sensitive to magnetic stray fields $g_{\mathrm{orb}}\mu_{\mathrm{orb}}h_{\mathrm{p}}^{\mathrm{orb}}$ and $g_{\mathrm{orb}}\mu_{\mathrm{orb}}h_{\mathrm{ap}}^{\mathrm{orb}}$ along the tube axis. The orbital magnetic moments $\mu_{\mathrm{orb}}^{\mathrm{p}}/\mu_{\mathrm{orb}}^{\mathrm{ap}}$ are considered to be larger then μ_{B} by one order of magnitude [84]. In Fig. 2.E.1 we present a TMR calculation for $\Delta_{\mathrm{SO}} = 100\,\mu\mathrm{eV}$, orbital polarization $P_{\mathrm{orb}} = 0.6$ and stray fields $g_{\mathrm{orb}}\mu_{\mathrm{orb}}h_{\mathrm{ap}}^{\mathrm{orb}} = -80\,\mu\mathrm{eV}$ and $g_{\mathrm{orb}}\mu_{\mathrm{orb}}h_{\mathrm{p}}^{\mathrm{orb}} = -40\,\mu\mathrm{eV}$ again combined with the experimental data. The spin-dependent shifts are assumed to be negligible in this setup. We see that the agreement with the experimental data improved slightly in Fig. 2.E.1 at the expense of additional free parameters. It is, however, outside the scope of this thesis to discuss the effect of spin-orbit coupling and the valley polarization in more detail.

Part III

A carbon nanotube as a ballistic electron waveguide

Chapter 3

An electronic Fabry-Perot interferometer

The wave-like nature of the electron has been demonstrated in a multitude of solid state physics experiments, e.g., on quantum corrals [85, 86] and on quantum point contacts [87] in 2DEGs, or, more recently, in graphene [88]. In the 90s, coherent electron transport has been observed also in CNTs [89], leading the way towards electron interference experiments in this material system. In the beginning of this century, Liang et. al observed conductance fluctuations as a function of gate and bias voltage in a source-drain geometry, that were identified as an electron wave interference effect [21]. Scattering at the nanotube-metal interface leads to interference of right- and left-moving electron waves, in analogy to an optical Fabry-Perot (FP) interferometer [90]. By changing the gate voltage V_g or the bias voltage V_b, the energy of the electrons trapped in the CNT 'cavity' and thereby the electron wave vector $\vec{k}$ can be tuned; in measurements of the differential conductance G, characteristic oscillatory patterns occur corresponding to constructive and destructive addition of the electronic wavefunctions. The *fundamental frequency* of the oscillations directly relates to the length of the contacted nanotube segment, i.e., the length of the interferometer cavity [21].

In carbon nanotube waveguides, additional features with respect to the optical FP transmission patterns can be observed in the transmission spectra [91, 92]. In Fig. 3.1, $G(V_\mathrm{g}, V_\mathrm{b})$ of a device in the Fabry-Perot regime is plotted. The *fast* oscillations along the gate voltage axis (period $\sim 10\,\mathrm{mV}$) can be related to the oscillations at the fundamental frequency f_1, quite similar to the optical FP interferometer. On top of this *primary* interference, a modulation in V_g with a period of a few volts is visible. To distinguish this pattern from the fast, fundamental oscillations that are directly related to the length of the cavity we refer to it as *secondary* interference pattern or

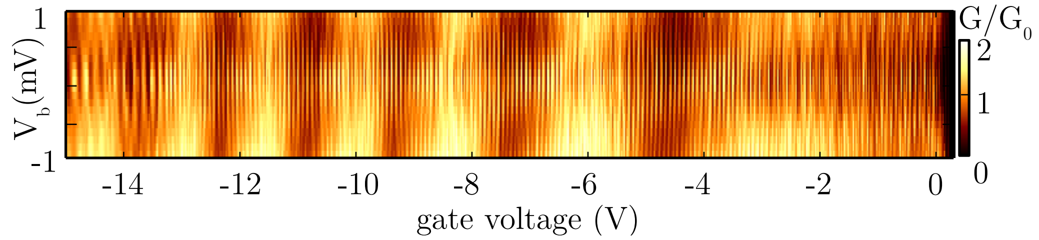

Figure 3.1: $G(V_\mathrm{g}, V_\mathrm{b})$ in the Fabry-Perot regime. The *fast* oscillations ($\sim$ 10 mV) along the gate voltage axis directly correspond to the optical Fabry-Perot interference with a period proportional to the distance between the contacts. On top of this *primary* interference effect, a modulation of the conductance can be observed on the scale of a few volts – the secondary interference.

slow oscillation in the following.

The authors of Ref. [91] suggest impurities in the CNT as a possible source of the secondary interference patterns. The impurities act as scattering centers that subdivide the CNT into a series of coupled FP interferometers. A different interpretation is provided by Jiang et al. in Ref. [93] and related works [94, 95]: The secondary interference pattern is interpreted as a *beating* of electron waves that acquire different phases in different transport channels. According to the authors, this effect can be observed in all but zigzag class carbon nanotubes. The analysis by Jiang et al. covers all basic concepts of the electron wave interference in CNTs. However, compared to the approach presented here, less value is set on the symmetry properties of the different CNT classes. The results of Ref. [93] are set side by side to ours in Sec. 3.1.5.

The symmetry considerations allow us to clarify the role of the different secondary interference patterns. We distinguish between the *beating* that can be observed solely in *armchair* CNTs and a *slow modulation* of the average conductance which is present in *armchair-like* CNTs and, under some circumstances, also in *zigzag-like* CNTs. On the basis of the FP analog and taking into account the trigonal warping of the dispersion relation we develop a qualitative and quantitative understanding of the secondary interference effect in Sec. 3.1.3. We present experimental data of a carbon nanotube as an electron waveguide in Sec. 3.2 and evaluate the secondary interference pattern in the data in Sec. 3.2.2. The results presented here are, by the time of this writing, about to be published and a preprint is available [96].

3.1 CNT Fabry-Perot interference

The electronic transport through a CNT in the strong coupling regime can be understood from the wave nature of the electron in analogy to the optical Fabry-Perot cavity. We introduce the basic concepts which lead to secondary interference in CNTs at the hand of analytic arguments supported by exemplary transmission data. The examples are obtained from ab-initio tight-binding calculations provided by M. del Valle from the group of M. Grifoni. For details on the parameters of this calculations please refer to the supplement, Sec. 4.A. For simplicity, the analytic arguments are based on the transmission function $\mathcal{T}$ of the Landauer-Büttiker formalism that is in general not directly proportional to the zero-bias conductance, i.e., the derivative of the current in Eq. (1.1). At millikelvin temperatures, however, we can to a good approximation assume $f'(E,\mu) \propto \delta(E-\mu)$.

3.1.1 Primary Fabry-Perot interference

To a first approximation we can describe the propagating electrons in the channel j by plane electron waves. It is important to note that the basic Fabry-Perot interference observed in CNTs only requires one single channel. It is the interference of a directly transmitted wave with waves that circulate one or multiple times in the cavity which produces the *fast* oscillations in G in Fig. 3.1. In terms of the phase ϕ_j acquired upon one roundtrip j, the resonance condition is given by

$$\begin{aligned}\phi_j(V_\mathrm{g},V_\mathrm{b}) &\equiv |\phi_j^{\mathrm{direct}}(V_\mathrm{g},V_\mathrm{b}) - \phi_j^{\mathrm{one-lap}}(V_\mathrm{g},V_\mathrm{b})| \\ &= |k_{j,l}(V_\mathrm{g},V_\mathrm{b}) - k_{j,r}(V_\mathrm{g},V_\mathrm{b})|L \\ &\overset{!}{=} 2\pi n, \end{aligned} \tag{3.1}$$

where $k_{j,r}$ and $k_{j,l}$ describe the wave vector component parallel to the nanotube axis of the right and left moving electrons in channel j, respectively, and n is an integer. When we insert the approximately linear dispersion relation of graphene in the vicinity of the Dirac point, Eq. (1.8), in Eq. (3.1), we obtain the relation between the cavity length and the energy difference $\Delta E(\Delta V_\mathrm{g},\Delta V_\mathrm{b})$ corresponding to one period which is related to a change in bias voltage ΔV_b, a change in gate voltage ΔV_g or a change in both,

$$\Delta\phi_j(\Delta V_\mathrm{g},\Delta V_\mathrm{b}) = |\Delta k_{i,l} - \Delta k_{i,r}|L \simeq \frac{2\Delta E(\Delta V_\mathrm{g},\Delta V_\mathrm{b})L}{\hbar v_\mathrm{F}} = 2\pi. \tag{3.2}$$

In this linear regime, we can directly obtain the length of the cavity from the primary FP interference estimating the Fermi velocity, $v_\mathrm{F} \approx 8 \cdot 10^5\,\mathrm{m/s}$ [31].

For the *armchair* (and also the *armchair-like*) class it is convenient to use $\kappa_{i,j}$ instead of $k_{i,j}$ to measure the wave vector from the Dirac point. We recall from Sec. 1.2.2 that the Dirac points in these two classes are at $\vec{K} = (k_{||} = K, k_{\perp} = 0)$ and $\vec{K}' = -\vec{K}$. We define $k_{a,l} = -K + \kappa_{a,l}$, $k_{b,r} = -K + \kappa_{b,r}$, $k_{a,r} = K + \kappa_{a,r}$ and $k_{b,l} = K + \kappa_{b,l}$, so that the resonance condition, Eq. (3.2), reads

$$\Delta\phi_j(\Delta V_{\mathrm{g}}, \Delta V_{\mathrm{b}}) = |\Delta\kappa_{j,l}(\Delta V_{\mathrm{g}}, \Delta V_{\mathrm{b}}) - \Delta\kappa_{j,r}(\Delta V_{\mathrm{g}}, \Delta V_{\mathrm{b}})|L = 2\pi. \tag{3.3}$$

Note that in the following we omit the Δ in front of ϕ_j. We measure the phase change in channel j always with respect to the Dirac point and assume $V_{\mathrm{g}} = V_{\mathrm{b}} = 0\,\mathrm{V}$ at the Dirac point, i.e., $\phi_j(V_{\mathrm{g}} = V_{\mathrm{b}} = 0\,\mathrm{V}) = 0$ for *all* CNT classes.

3.1.2 Multi-channel Fabry-Perot interference without mixing

Due to the valley and spin degrees of freedom we have to consider four conduction channels in a CNT waveguide [20]. Since the spin-degeneracy is not lifted in our experiment, we effectively deal with two pairs of spin-degenerate channels. Depending on the symmetries of the CNT, these pairs are called *Kramers* pairs or *valley* pairs. We clarify this distinction below. Within the cavity, the electron experiences multiple reflections at the contacts that can potentially mix the channels. Assuming that these channels are *independent*, i.e., not mixed upon reflection, the transmission amplitude can be described in terms of a two-channel Fabry-Perot interferometer [26],

$$\mathcal{T}(V_{\mathrm{g}}) = 2 \sum_{c\in\{a,b\}} \frac{|t_1|^2|t_2|^2}{(1 + |r_1|^2|r_2|^2 - 2|r_1||r_2|\cos[\phi_j(V_{\mathrm{g}}, L)]}, \tag{3.4}$$

where we put $V_{\mathrm{b}} = 0\,\mathrm{V}$ for simplicity and the transmission and reflection coefficients for the two barriers are given by t_1, t_2 and r_1, r_2, respectively.

If the two channels are described by identical relations $\phi_a(V_{\mathrm{g}}) = \phi_b(V_{\mathrm{g}})$, we expect to obtain single-mode Fabry-Perot interference as shown, e.g., in Fig. 3.1(c). In this case, only *primary* interference is observed. In general, when electrons in the channels do not accumulate the same phase, $\phi_a(V_{\mathrm{g}}) \neq \phi_b(V_{\mathrm{g}})$, we expect the formation of a *beat*, a transmission pattern resulting from the superposition of two FP channels with different wavevectors, see Fig. 3.2(c). Notably, the transmission pattern in Fig. 3.2(f) reflects a third case that can not be described by Eq. (3.4). We can understand its special role when we relate the three cases to the different CNT types.

3.1.3 CNT symmetry classification and the relation to interference patterns

For the classification of the CNTs we exploit the fact that the CNT eigenstates in infinitely long CNTs are invariant under the action of $\mathcal{C}_d$, the rotation of the CNT around its longitudinal axis by $2\pi/d$. d is an integer specific to the geometry of the CNT. When this symmetry is preserved also in the finite CNT including the coupling to the contacts, the crystal angular momentum $\mathfrak{m}$ is conserved and can be used to discriminate between *zigzag-like* CNTs with angular momenta $\mathfrak{m}_a$ and $\mathfrak{m}_b$ in the two valleys, respectively, and *armchair-like* CNTs with $\mathfrak{m} = 0$, as introduced in Sec. 1.2.2. Since the CNTs are supposed to be free of defects, it is only the interface to the contacts that potentially breaks the $\mathcal{C}_d$ symmetry. In the following, we discuss first the case that the contact interface does not break the $\mathcal{C}_d$ symmetry, i.e., the case of *ideal* contacts.

zigzag and zigzag-like with ideal contacts

In the contour plots in Fig. 3.1(a,d), the equi-energy lines in the vicinity of one Dirac point in the graphene $\vec{k}$-space are shown. A line indicates the θ-dependent cut that is used to obtain one half of the the 1D dispersion relations (b,e) from (a,d). Note that for all CNTs except zigzag ones, the trigonal warping of the equi-energy lines in the dispersion relation of graphene leads to a difference in the wave vectors of electrons on the right- and left-mover branch at $\varepsilon \neq 0$. The possible scattering processes in zigzag and zigzag-like CNTs are given in Fig. 3.1(b) and (e). The two lowest spin-degenerate subbands have different quantum numbers $\mathfrak{m}_a$ and $\mathfrak{m}_b$, thus, due to the $\mathcal{C}_d$ symmetry of the Hamiltonian, there is *no mixing* of the channels. The different angular momentum in the two channels is also reflected by the different perpendicular components of the wave vector in the two valleys, $k_\perp = \pm K$. Time reversal symmetry requires $\varepsilon_a(k) = \varepsilon_b(-k)$, therefore at a given energy $k_{a,l} = -k_{b,r}$ and $k_{a,r} = -k_{b,l}$, which implies $\phi_a = \phi_b$ in Eq. 3.4. Hence, the channels acquire the same phase difference due to a change in V_g or V_b. The problem can thus be mapped onto a single mode FP interferometer. Tight-binding calculations confirm the single-mode-like character of the interference pattern for all numerically evaluated *zigzag-like* CNTs. Fig. 3.1(f) shows the results for a (6,3) CNT with a length of 1240 nm.

In *zigzag* CNTs, $\varepsilon_j(k)$ is symmetric with respect to the Dirac point within each valley, i.e., $k_{a,l} = k_{a,r}$ and $k_{b,r} = k_{b,l}$, see Fig. 3.1(b). Consequently, the arguments used for *zigzag-like* CNTs apply also to the *zigzag* CNTs. For the transmission we again obtain a single-mode interference pattern, see

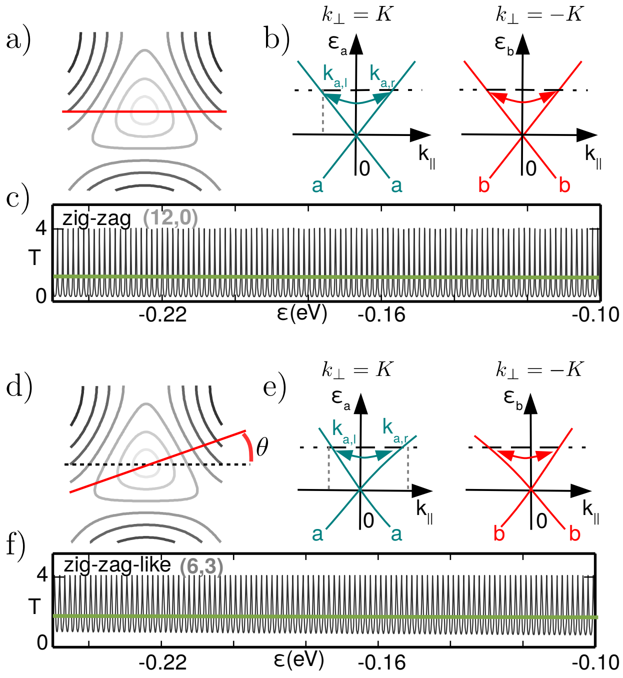

Figure 3.1: (a) *Zigzag*. Graphene dispersion relation $\varepsilon(\vec{k})$ in the vicinity of one Dirac point. The red line marks the direction of $k \equiv k_{||}$. (b) The lowest 1D subbands in the vicinity of both $\vec{K}$ and $\vec{K}'$ points, $\varepsilon_a(k)$ and $\varepsilon_b(k)$ at $k_\perp = K$ (green) and $k_\perp = -K$ (red) are identical and symmetric with respect to the $\vec{K}$ and $\vec{K}'$ point, respectively. (c) Exemplary transmission pattern obtained by tight-binding (TB) calculations provided by M. del Valle, see appendix, Sec. 4.A. The transmission of a (6,0) CNT in the tight-binding calculation shows no slow modulation. (d,e) *Zigzag-like*. Right and left moving branches within each valley exhibit different wave vectors $k_{j,r/l}$ due to the trigonal warping. The states in the two valleys have different crystal angular momentum. Therefore, no inter-valley scattering is possible in *zigzag* and *zigzag-like* CNTs with ideal contacts, see text. (f) A single-channel-like transmission pattern can be observed for the (6,3) CNT.

Fig. 3.1(c).

armchair and armchair-like with ideal contacts

In *armchair* and *armchair-like* CNTs, states in both valleys K and K' share the property $\mathfrak{m} = 0$, therefore the $\mathcal{C}_d$ symmetry does not prevent scattering between the valleys, see Fig. 3.2(b,e). Ideally, *armchair* CNTs are parity symmetric, i.e., mirror symmetric with respect to a plane perpendicular to the nanotube axis. In Fig. 3.2(b), the eigenstates a with even parity are described by the green line and the eigenstates b with odd parity by the red line.

As a consequence of the parity symmetry, the transmission is given by the superposition of independent channels labeled by the parity states with different wave vectors $\kappa_{a,\mathrm{r}} = -\kappa_{a,\mathrm{l}} \neq \kappa_{b,\mathrm{r}} = -\kappa_{b,\mathrm{l}}$. Here, the equalities are a consequence of time-reversal symmetry. Thus, when we increase the gate voltage by V_g (starting from the Dirac point), the phases in the two channels are affected differently, $\phi_a(V_\mathrm{g}) = 2\kappa_{a,r}(V_\mathrm{g})L \neq \phi_b(V_\mathrm{g}) = 2\kappa_{b,r}(V_\mathrm{g})L$. In the transmission spectra we consequently observe a characteristic beat, as, e.g., in the transmission spectrum of a $(7,7)$ CNT in Fig. 3.2(c).

In *armchair-like* CNTs, the wave vectors of the electrons are also subject to trigonal warping since $\theta > 0$. At the same time, the parity symmetry is absent and both intervalley and intravalley scattering processes can take place, see Fig. 3.2(e). This makes it difficult to label transport channels in a manner similar to the three other cases discussed so far. Here, we treat the transmission in the *armchair* geometry as a limiting case of the *armchair-like* geometry. This implies that the labels a and b refer to the same pairs of branches as in the *armchair* geometry, see Fig. 3.2(e), but due to the absence of the parity symmetry the two channels are mixed. In a simple model presented in the appendix, Sec. 4.C, we start from independent channels a and b and allow for a finite inter-channel mixing upon reflection at the interfaces. The sliding average of the transmission in this simple models shows a slow modulation, similar to what is observed in tight-binding calculations for *armchair-like* CNTs, compare Fig. 3.2(f). The slow modulation is governed by the phase difference $\Delta\phi^\theta(E) = |\phi_a^\theta(E) - \phi_b^\theta(E)| = 2|\kappa_{a,i}^\theta(E) - \kappa_{b,i}^\theta(E)|L$ between the modes, which is the same for $i = l$ and $i = r$. In particular, a peak at energy E_n in the average conductance occurs when

$$\Delta\phi^\theta(E_n) = 2\pi n, \tag{3.5}$$

i.e., when the two channels interfere constructively. We test this relation by evaluating the peak positions E_n of the average conductance in the tight-binding model for the *armchair-like* $(10,4)$ CNT in Fig. 3.3(a). The wave

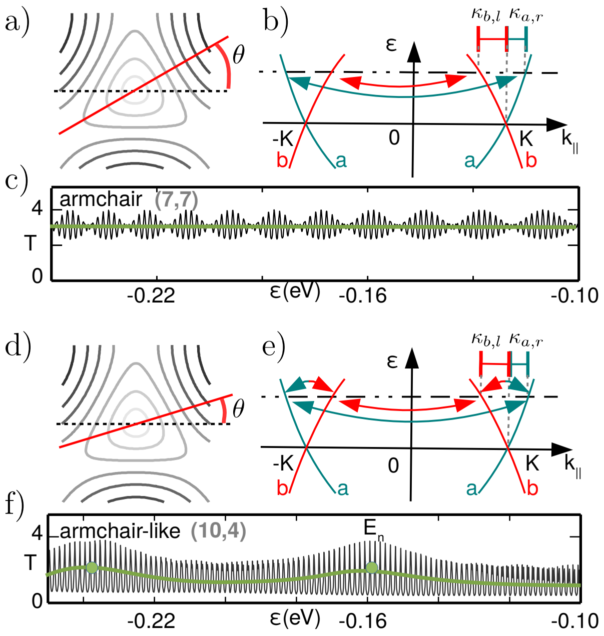

Figure 3.2: Dispersion relation and model transmission for *armchair* (a-c) and *armchair-like* CNTs (d-f). The figure is organized similar to Fig. 3.1. *Armchair*: (a) The maximal chiral angle $\theta = 30°$ induces a maximal difference between the wavevectors in the right and left-moving branches in each valley in (b). Due to the parity symmetry, scattering only takes place between the two inner branches a (red lines) and the two outer branches b (green lines). Since the two channels accumulate different phases, a beat in the interference pattern is observed in the TB calculation for the (7,7) CNT. *Armchair-like*: (d,e) Trigonal warping leads to a wavevector difference between the right- and left-moving branches in both valleys, similar to the *armchair* case. In the *armchair-like* CNTs the parity symmetry is broken and inter-channel scattering is enabled (see text). (f) A slow modulation of the sliding average can be observed in the transmission of a (10,4) CNT. The peaks in the average are marked by filled circles and are labeled by the position E_n of point n, each.

vector components $\kappa_{j,i}$ on the different branches that occur in the phase difference $\Delta\phi^\theta(E)$ are given by $\varepsilon^\theta(K + \kappa_{a,r}) = E$, $\varepsilon^\theta(K + \kappa_{b,l}) = E$ and similarly for the two branches $\kappa_{a,l}$ and $\kappa_{b,r}$ in the vicinity of K', see Fig. 3.2(b). For simplicity, we us the zone-folding approximation, Eq. (1.10), to calculate the dispersion relation $\varepsilon^\theta(k)$.[1] The phase difference $\Delta\phi^\theta(E)$ is shown for different chiral angles θ in Fig. 3.3(b). We can already see from Fig. 3.2(a) that the wave vector difference $\kappa_{a,l}-\kappa_{b,r}$ in the vicinity of the $\vec{K}'$ point depends on the chiral angle and reaches its maximum for $\theta = 30°$. The evolution of the phase difference $\Delta\phi^\theta(E)$ is thus directly governed by the trigonal warping of the equi-energy lines in the graphene dispersion. Consequently, the slope of $\Delta\phi^\theta(E)$ is monotonically increasing with θ and is zero for the *zigzag* case and maximal for the *armchair* case. For energies $E \leq 1\,\mathrm{eV}$ and neglecting curvature effects, the trigonal warping can be accounted for by a factor $\sin(3\theta)$ [93]. Within this approximation we obtain for the phase difference

$$\Delta\phi^\theta(E) = \Delta\phi^{30°}(E)\sin(3\theta), \tag{3.6}$$

where $\Delta\phi^{30°}$ is the phase difference between the channels for energy E in the *armchair* CNT.

We use the positions E_n extracted from the averaged conductance $\bar{G}(V_\mathrm{g})$ in Fig. 3.3(a) to insert points at coordinates $(E_n, 2\pi n)$ in (b) according to Eq. (3.5). The points lie on the line for $\theta = 16.1°$ which corresponds to the chiral angle of a $(10, 4)$ CNT. The conductance calculated in the tight-binding model thus agrees nicely with the analysis in Sec. 4.C, i.e., with Eq. (3.5). We will use this important result in the next section to evaluate transport data.

3.1.4 Secondary interference in CNTs with broken symmetry

The secondary interference which is accompanied by the slow modulation of the average conductance is a consequence of the mixing of the transport channels. This mixing is prohibited in *zigzag-like* CNTs as long as the coupling between the leads and the CNT is symmetric under the application of $\mathcal{C}_d$. When this symmetry is broken we recover the secondary interference effects observed for *armchair-like* CNTs also in *zigzag-like* CNTs. In Fig. 3.4(a) we plot the conductance calculated for a *zigzag-like* $(6, 3)$ CNT with random on-site energies in the range $0.07\,\mathrm{eV} \leq \epsilon_{2p} \leq 8\,\mathrm{eV}$ (average $\bar{\epsilon}_{2p} = 3\,\mathrm{eV}$) in the ring that couples the CNT to the lead (cf. Sec. 4.A). On top we show

---

[1] Calculations that include curvature and spin-orbit effects can be found in the appendix, Sec. 4.A. These refinements do not affect the analysis of the secondary interference pattern.

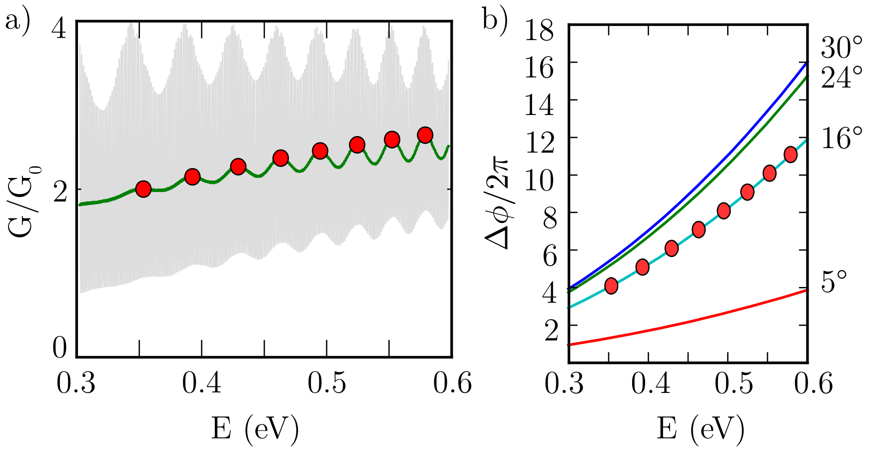

Figure 3.3: (a) Conductance G (light gray) and average conductance (green line) for a $(10, 4)$ CNT of length 1240 nm ($G_0 = \mathrm{e}^2/h$). Peak positions E_n in the average conductance are marked by red filled circles. (b) Phase differences $\Delta\phi^\theta$ between modes as a function of energy measured from the Dirac point for different chiral angles θ indicated on the right. The filled circles are obtained using the peak positions E_n of the slow modulation in (a) and requiring $\Delta\phi/2\pi = n$.

the sliding average conductance $\bar{G}$ (green line). The peak positions E_n are extracted from $\bar{G}$ and compared to the the evolution of $\Delta\phi^\theta$ for a $(6, 3)$ CNT with chiral angle $\theta = 19.1°$ in (b). The clear correspondence indicates that our interpretation of the secondary interference in *zigzag-like* CNTs with broken symmetry is consistent with the tight-binding model.

Similar results are obtained when the symmetry in the *zigzag-like* CNT is broken by using two different values for the on-site energies on the upper, $\epsilon_{2p} = 5\,\mathrm{eV}$, and lower half, $\epsilon_{2p} = 1\,\mathrm{eV}$, of the contact ring in a *zigzag-like* $(9, 6)$, see Fig. 3.5.

The parity symmetry in *armchair* CNTs seems to be surprisingly robust against symmetry braking in the contact ring. Tests with random on-site energies in the same range as applied to the *zigzag-like* CNTs show little effect on the secondary interference pattern or the sliding average of the conductance.

3.1.5 Comparison to results by Jiang et al.

The relation between the secondary interference pattern in the FP interference and the CNT dispersion has been reported by Jiang et al. in 2003 [93]. The authors observe secondary interference patterns in all CNT classes except the

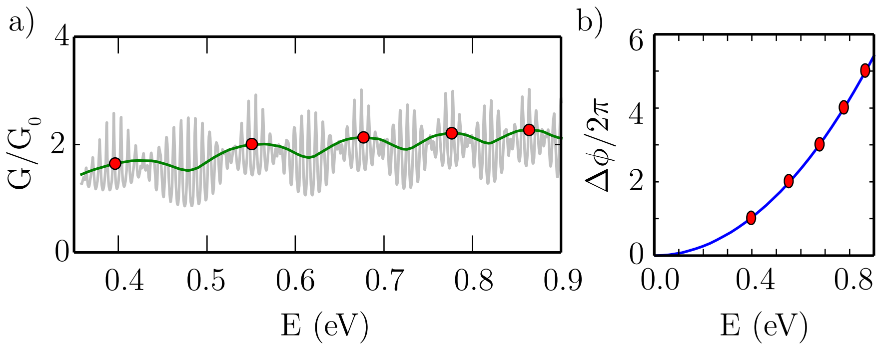

Figure 3.4: (a) Conductance G for a *zigzag-like* $(6, 3)$ CNT ($L = 220\,\mathrm{nm}$, $\theta = 19.1°$) with random on-site energies in the range $0.07\,\mathrm{eV} \leq \epsilon_{2p} \leq 8\,\mathrm{eV}$ on the coupling ring (light gray line) and the sliding average of the conductance $\bar{G}$ (green line). We clearly observe a secondary interference pattern and a modulation of the average. The peaks in the average are marked by red filled circles. Over the full gate voltage range, a slight increase of the conductance level is observed in the average and is subtracted prior to peak detection. This results in an offset of the first marker with respect to the apparent peak in the sliding average. (b) The phase difference between the channels from the zone-folding dispersion relation (blue line) compared to the peak positions from (a) assuming that Eq. (3.5) holds.

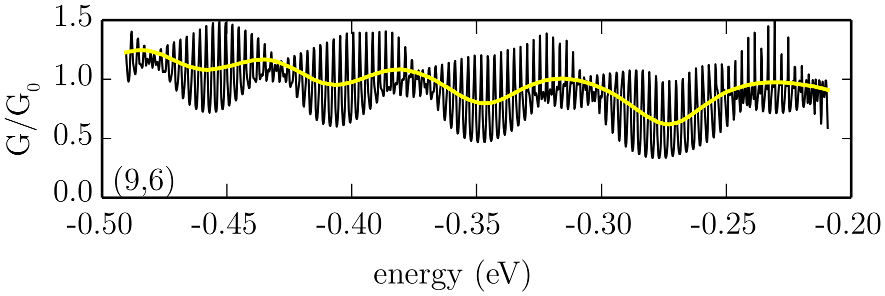

Figure 3.5: Conductance G (black line) and the sliding average of the conductance (yellow line) for a *zigzag-like* $(9, 6)$ CNT with $L = 660\,\mathrm{nm}$, $\theta = 23.4°$. The rotational symmetry of the coupling region is broken by choosing different on-site energies at the top, $\epsilon_{2p} = 5\,\mathrm{eV}$, and at the bottom half coupling ring, $\epsilon_{2p} = 1\,\mathrm{eV}$. We clearly observe a secondary interference pattern and a modulation of the average.

zigzag class in tight-binding calculations. For *armchair*, *armchair-like* and *zigzag-like* CNTs, Jiang et al. provide an equation, Eq. (8) in Ref. [93], for the period of the secondary interference pattern in gate voltage as a function of the number n of the period counted from the Dirac point, i.e., $V_\mathrm{g} = 0\,\mathrm{V}$. This result agrees with our findings.

The authors further claim that for any CNT class "[...] both the rapid and slow oscillation periods are independent of the choice of the [on-site energy values on the coupling ring for the two sublattices], which can also be seen clearly from the later discussions.". From our analysis, we see that this is not the case for *zigzag-like* CNTs, where a rotational symmetric coupling suppresses the "slow oscillations".[2]

This deviation with respect to our findings roots in the different approaches with respect to the CNT symmetries, and, more specifically, the rotational symmetry. The consideration of CNTs with *ideal* contacts as a starting point for a basic analysis of the interference patterns that we can expect in the different CNT classes allows us to discriminate carefully between the beating observed in *armchair* CNTs with a constant sliding average and the slow modulation of the sliding average in *armchair-like* CNTs (and *zigzag-like* CNTs with broken rotational symmetry). This distinction is the main advance with respect to the work by Jiang et al. on the theoretical side.

Realizing the difference between these two forms of secondary interference allows for a more reliable analysis. This becomes clear when we try to apply Eq. (8) in Ref. [93] to experimental data. While this equation correctly describes the evolution of the period of the secondary interference in general, it is *a priori* not clear how to measure *one period* in the conductance data. From our analysis we know that the secondary interference observed in *armchair* CNTs is a beating with two maxima (of the hull curve) within one period (cf. Sec. 4.C) while the secondary interference that appears due to channel mixing in *armchair-like* and *zigzag-like* CNTs, i.e., the slow modulation of the sliding average, exhibits one peak per period. Thus, when one observes such a periodical slow modulation of the average, he measures one period as the distance between subsequent peaks in the average. When the average is constant, one period is given by the distance between every second peak.

3.2 Experiment & Evaluation

The data shown in this part of the thesis is recorded from KG_R3BB, a sample fabricated by K. Götz and F. Schupp from the group of A. K. Hüttel. The electrode material, a 10/40 nm Ti/Pt bilayer, is patterned on top of

---

[2] The term "slow oscillation" is used in Ref. [93] synonymous to "beating".

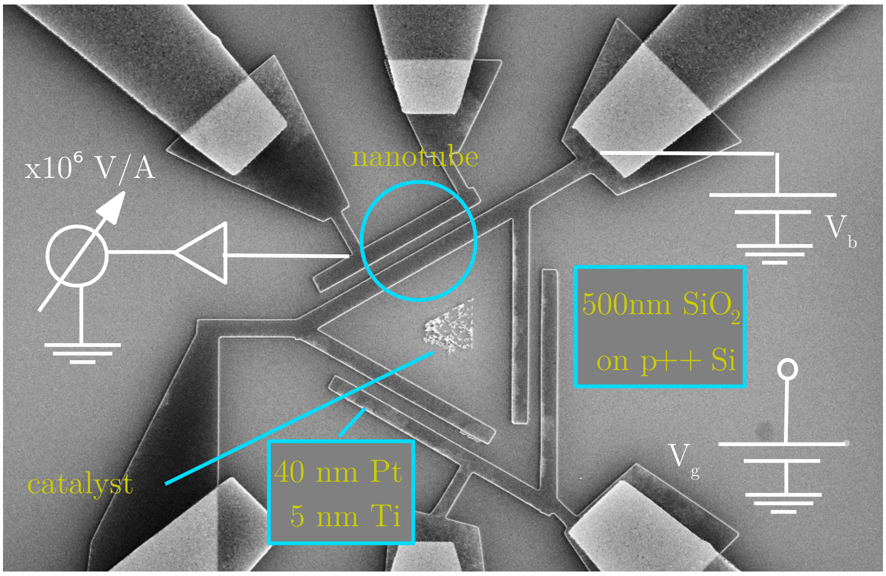

Figure 3.1: Electron micrograph of a sample similar to the measured device. The Pt/Ti structures on top of the Si/SiO_2 are clearly visible. In the center of the triangular structure traces of the catalyst can be identified. Schematic drawings indicate the measurement circuit.

a degenerately doped Si substrate with a 500 nm thick insulating capping layer, see Fig. 3.1. In order to avoid contamination of the CNT, we grow the carbon nanotube as a last fabrication step across the contact electrodes separated by a 1.2 μm trench [8]. The details of the fabrication are identical to the recipe for the sample AD_CB14 presented in Sec. 4.D apart from an additional etching step prior to the CNT growth which is applied to deepen the trench between the contacts. The identification of a promising device is done solely via room temperature transport measurements using a probe station. This is necessary to avoid contamination of the nanotube. The transport measurements presented here, e.g., in Fig. 1, were recorded at a base temperature of 15 mK in a ^{3}He/^{4}He dilution cryostat.

3.2.1 Transport Measurement

The presented measurements were conducted using a DC measurement setup with the bias voltage applied to the source contact while the drain contact is grounded. A current-voltage amplifier is used to sensitively measure DC current at the drain contact. The amplification is set to 10^6 V/A throughout the experiment. The conductance is obtained by numerical derivation of the current data.

Conductance data

$G(V_\mathrm{g}, V_\mathrm{b})$ for the sample KG_R3BB is shown in Fig. 3.2(a). Panel (e) shows a linetrace of (a) at zero bias. On average, the conductance is $\sim 1\,\mathrm{e}^2/\mathrm{h}$, with peak values of $2\,\mathrm{e}^2/\mathrm{h}$. The most prominent feature observed in Fig. 3.2(a,e) is a repeated modulation of the conductance on a scale of a $1-2\,\mathrm{V}$. It is accompanied by a slow modulation of the sliding average conductance $\bar{G}$ shown in (f). The period of this slow modulation decreases with more negative gate voltage values. This pattern is identified with the slow modulation of the average conductance observed in the *armchair-like* CNTs in the previous section. For a later analysis we extract the positions of the peaks in the average conductance, Fig. 3.2(f), and label the positions in gate voltage by $V_{\mathrm{g},n}$, $n = 1 \dots 7$. From these values we obtain the peak positions $E_n = \alpha V_{\mathrm{g},n} + \Delta E_\mathrm{gap}$, where α is the gate voltage lever arm and ΔE_gap is an energy offset that accounts for the doping of the CNT. The lever arm α is given by the ratio $\Delta V_\mathrm{b}/2\Delta V_\mathrm{g}$ where the distances are measured between two pairs of peaks in the conductance, respectively, that form rhombic structures in $G(V_\mathrm{g}, V_\mathrm{b})$. These structures can be identified in three regions of constructive interference shown in Fig. 3.2(b-d). We discuss the extraction of the lever arm in the ballistic FP regime in Sec. 4.B of the appendix. Across a wide range of gate voltages, $-15\,\mathrm{V} < V_\mathrm{g} < -2\,\mathrm{V}$, the gate conversion factor stays almost constant, $\alpha_\mathrm{h} = 0.0210 \pm 0.0007$, with slight variations as can be seen from the (similarly sized) rhombi in the panels (b-d). Contrarily, in the vicinity of the bandgap the lever arm increases and reaches its peak value, 0.68 ± 0.03, in the band gap, see Fig. 3.3(b).

To compare the conductance data to model calculations we have to measure the energy difference from a unique common point of reference. We choose the Dirac point in the model which is identified with the center of the bandgap at $V_\mathrm{g} = 0.28\,\mathrm{V}$ in the experiment. We thus have to assess the difference $\Delta E_\mathrm{gap} = \int_{0\,\mathrm{V}}^{0.28\,\mathrm{V}} \alpha_\mathrm{gap}(V_\mathrm{g})\mathrm{d}V_\mathrm{g}$ between $V_\mathrm{g} = 0\,\mathrm{V}$ and the center of the bandgap. To this end, we extract the gate voltage lever arm in the vicinity of the bandgap on the hole side whenever it is possible (dots in Fig. 3.3(b)) and interpolate between the values (lines in (b)). We obtain $\Delta E_\mathrm{gap} = 60 \pm 5\,\mathrm{meV}$. The size of the bandgap, Fig. 3.3(a), is naturally obtained with a similar precision, $E_\mathrm{g} = 66 \pm 6\,\mathrm{meV}$. We summarize the values into Tab. 3.1.

3.2.2 Analysis of the secondary interference

The slow modulation of the sliding average conductance indicates that our specimen is of the *armchair-like* class or the *zigzag-like* class. When the latter applies, the rotational symmetry of the contact region is broken, e.g., by the

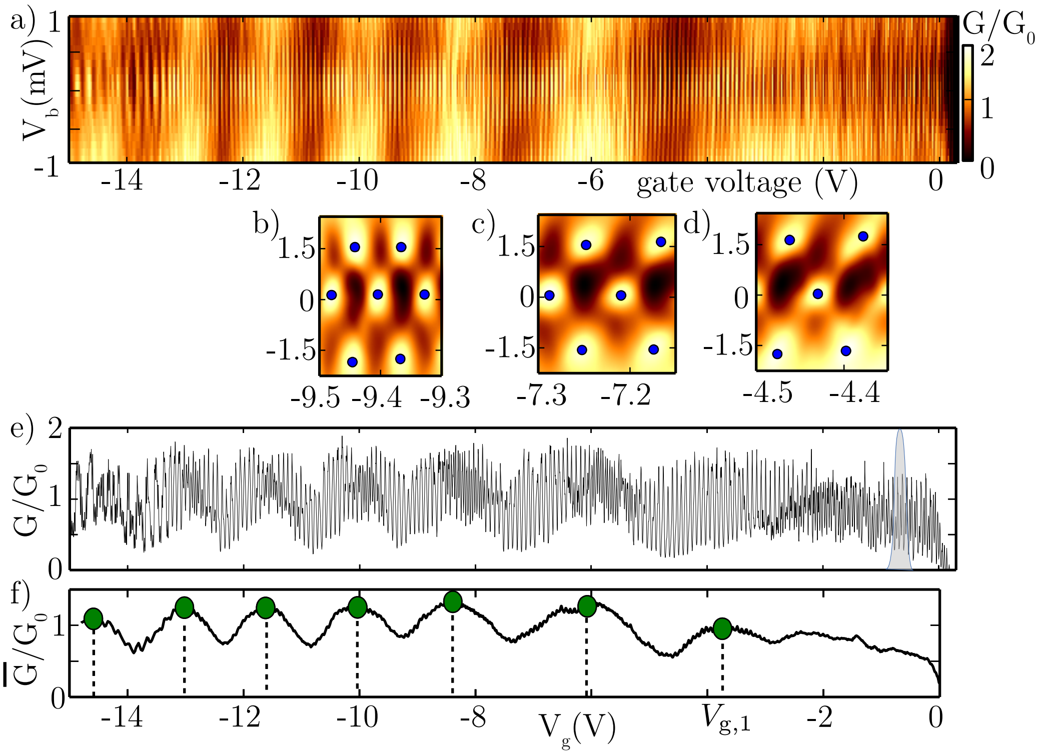

Figure 3.2: (a) $G(V_g, V_b)/G_0$ of sample KG_R3BB. We clearly observe a dense rhombic pattern superimposed with a slowly varying average conductance level (darker and brighter regions) with gate voltage. (b-d) Zoom of (a) with a slightly larger range in the bias voltage. Filled blue circles mark the peak positions of the conductance. (e) $G(V_g)/G_0$ at zero bias. In the transmitted signal, an oscillation with the fundamental frequency f_1 dominates the transmission spectrum. The oscillations at the fundamental frequency are periodically interrupted regularly by regions with a frequency doubling. (f) Moving average of the zero bias conductance $\bar{G}$. A slow oscillation is observed. The peaks are highlighted by filled green circles and their positions are labeled by $V_{g,n}$, $n = 1 \dots 7$.

$\alpha_{el}[\cdot 10^{-1}]$	$\alpha_h[\cdot 10^{-3}]$	E_{gap}	ΔE_{gap}	$f_1\,[\frac{1}{eV}]$	L [μm]
6.8 ± 0.3	21.0 ± 0.7	66 ± 6	60 ± 5	610 ± 10	0.99 ± 0.03

Table 3.1: Gate conversion factors, energy gap, offset of the energy gap, fundamental frequency and length extracted for sample KG_R3BB. All energies are given in units of meV. The error estimates are discussed in Sec. 3.2.2.

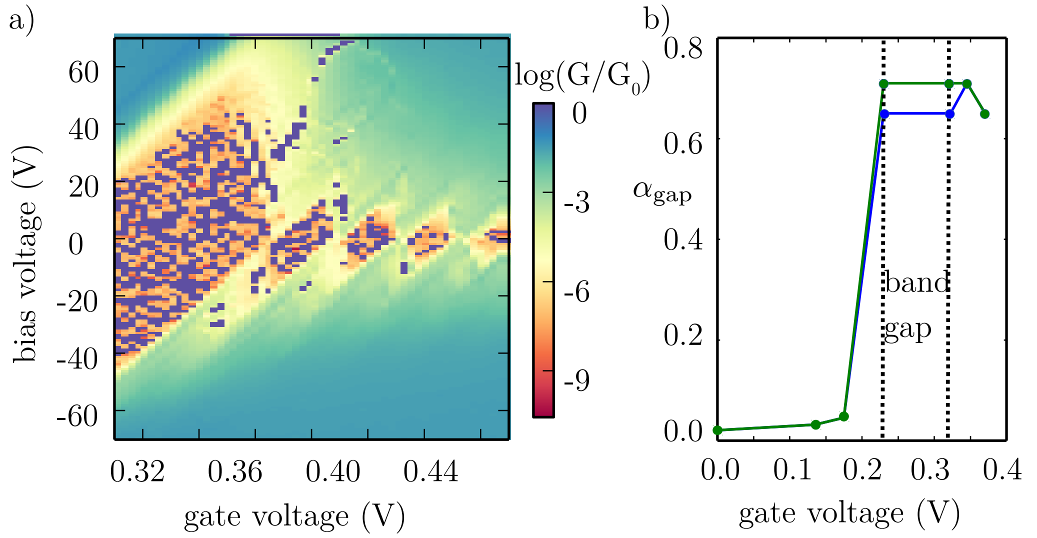

Figure 3.3: (a) $\log(G(V_{\mathrm{b}}, V_{\mathrm{g}})/G_0)$ showing the bandgap and the first few electron states. The left upper edge (source line) of the bandgap is clearly visible, while the right upper edge (drain line) is not clearly resolved and induces an error in the determination of the height of the bandgap and, similarly, the lever arm in the bandgap. (b) α_{gap} in the vicinity of the bandgap. The upper (green) and the lower (blue) graph indicate the range of possible values of α_{gap} estimated from (a).

asymmetric coupling of the CNT to the surface of the metallic leads. In both cases, the dispersion relation determines the peak positions E_n via Eq. (3.5) as has been shown for the numerical transmission data in the last paragraph in Sec. 3.1.3. By extracting the peak positions E_n from the experimental data, we can estimate the chiral angle θ of the specimen. Prerequisite to this analysis is a set of experimental data that covers a range in gate voltage where we are able to identify multiple peaks of the slow modulation of the average conductance. The larger the visible number of slow oscillations, the higher is the accuracy in identifying the chiral angle. The experimental data obtained from KG_R3BB is suitable for this analysis showing 7 peaks of the average conductance, see Fig. 3.2(f).

In order to fit the experimental data, we first assess the error in estimating the positions E_n of the maxima in the averaged conductance signal. The sources of this error are twofold: First, as already noted in Sec. 3.2.1, ΔE_{gap} can only be assessed with limited precision, $\Delta E_{\mathrm{gap}} = 60 \pm 5\,\mathrm{meV}$. Second, for the gate voltage lever arm in the region we are interested in, $V_{\mathrm{g}} < -2$, we obtain $\alpha = 0.0210 \pm 0.0007$. This induces non-negligible errors in E_n for the larger values of n. Finally, an additional uncertainty arises from the fact that the overlap energy t that is used in the model of the dispersion relation, see Sec. 1.2.2, is known with a precision $t = 2.6 \pm 0.1\,\mathrm{eV}$ [36, 43].

To determine the region of acceptable parameters for θ, we apply a χ^2 test on the hypothesis, that the model describes the measured data points E_n. The model dispersion is determined by the chiral angle θ, the offset ΔE_{gap} and the overlap energy t. For each set of parameters we calculate the χ^2 value,

$$\chi^2(\theta, \Delta E_{\mathrm{gap}}, t) = \sum_n \frac{1}{\sigma_n^2} \left[E(n, \theta, t) - (E_n + \Delta E_{\mathrm{gap}}) \right]^2 ,$$

where the values $E(n, \theta, t)$ are obtained from the condition $\Delta\phi^{\theta}(E, t) \overset{!}{=} 2\pi n$ and σ_n is the error in the estimation of the peak positions E_n, which is mainly determined by the error of α for $V_{\mathrm{g}} < -2\,\mathrm{V}$. From the χ^2 value we calculate $P = 1 - F_\nu(\chi^2)$, where F_ν is the cumulative distribution function for the χ^2 distribution, $\nu = N - N_{\mathrm{p}}$ is the number of degrees of freedom, $N = 7$ is the number of points for the fit and $N_{\mathrm{p}} = 2$ is the number of free parameters [97]. Thereby, apart from the chiral angle θ, the bandgap offset ΔE_{gap} is used as a free parameter which is allowed to vary within the bounds estimated above. In Fig. 3.4 we show $P(\theta, \Delta E_{\mathrm{gap}})$ for different values of the overlap integral in the tight-binding dispersion relation, t. By setting a threshold value for rejecting the fit, $P < 0.1$, we obtain two results. First, a value of $t = 2.7\,\mathrm{eV}$ is not consistent with our data within the range $55\,\mathrm{meV} \leq \Delta E_{\mathrm{gap}} \leq 65\,\mathrm{meV}$, see the left panel in Fig. 3.4. Smaller values for t, i.e., $2.5\,\mathrm{eV} \leq t \leq 2.6\,\mathrm{eV}$

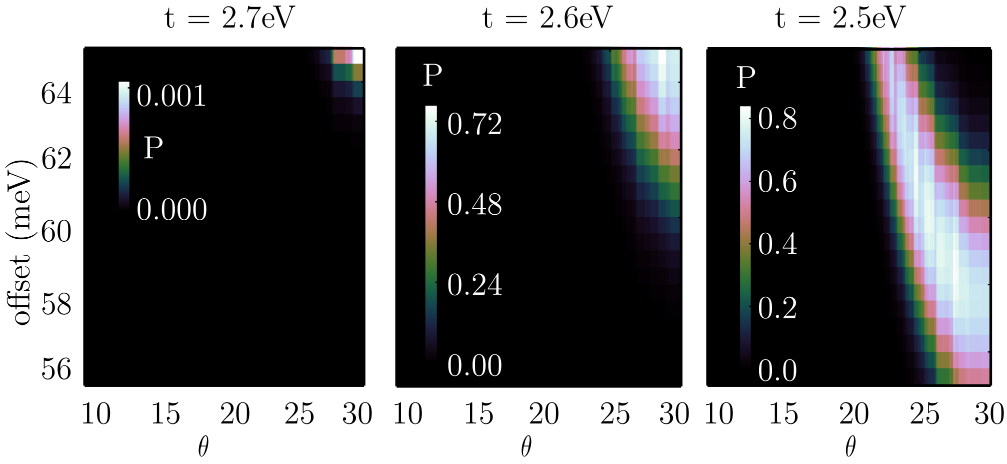

Figure 3.4: $P(\theta, \Delta E_{\text{gap}})$ for different values of t. Note that the range of the colorbar in the first panel is smaller by two orders of magnitude compared to the other two. A value of $t = 2.7\,\text{eV}$ is not consistent with our data, while values $2.5\,\text{eV} \leq t \leq 2.6\,\text{eV}$ are consistent.

yield acceptable fits. Second, the acceptable values for the chiral angle lie in the range $22° \leq \theta < 30°$.

In Fig. 3.5, we plot the phase difference $\Delta\phi^{\theta}(E)$ for different chiral angles θ obtained using $t = 2.5\,\text{eV}$. Note that the CNT with chiral angle $\theta = 30°$ (armchair) exhibits the steepest progression with energy. The phase difference $\Delta\phi^{\theta}(E)$ at a given energy is monotonically increasing with θ between the *zigzag* (Fig. 3.5, left inset) and the *armchair* case (right inset). The gray shaded area in Fig. 3.5 indicates the range $22° \leq \theta < 30°$ of acceptable fits to the experimental data.

3.2.3 The average length of the electron path

In this and in the next section we discuss properties of the conductance data which are not directly linked to the analysis of the secondary interference pattern. The starting point of this analysis is Eq. (3.4), which describes the transmission originating from two *independent* channels. Corresponding to the discussion in Sec. 3.1.3, this strictly holds in *zigzag* CNTs and in *zigzag-like* and *armchair* CNTs when the $\mathcal{C}_d$ and the parity symmetry are present, respectively. Eq. (3.4) is also valid for certain values of the gate voltage where the electrons in the two channels are in phase, i.e., regions where we observe essentially single-channel interference. In the following, we apply an analysis that is derived from Eq. (3.4), i.e., for a cavity without

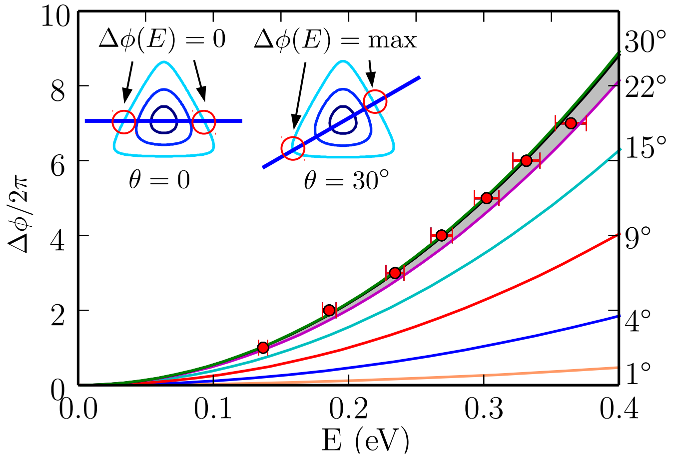

Figure 3.5: Phase differences $\Delta\phi$ between the two modes as a function of energy measured from the Dirac point. Lines indicate the numerically obtained $\Delta\phi^\theta(E)$ for different values of θ (indicated on the right). The phase difference is a monotonically increasing function of θ starting from the zigzag CNT with $\theta = 0$ (inset, left) to the armchair CNT with $\theta = 30°$ (inset, right). The experimental values (filled circles) are fitted varying the angle θ and the band-gap offset ΔE_{gap}. Acceptable fits are obtained by chiral angles in the range $22° \leq \theta < 30°$, as indicated by the gray shaded area.

T_{avg}	T_{p}	r_1	r_2	$l_{\mathrm{avg}}[L]$	$l_{\mathrm{avg}}^{\mathrm{FT}}[L]$
0.24	0.47	0.97	0.33	1.3	1.8

Table 3.2: Table with extracted parameters for sample KG_R3BB. The reflection coefficients r_1 and r_2 are evaluated directly from the peak and average values of the conductance data. The two values in the last column for n_{LT} are extracted from the ranges $-5\,\mathrm{V} < V_{\mathrm{g}} < -0.5\,\mathrm{V}$ (green) and $-14\,\mathrm{V} < V_{\mathrm{g}} < -5\,\mathrm{V}$ (blue), respectively.

mode mixing, also to data that shows clear evidence of mode mixing. We thereby assume that the effect of the mode mixing on the derived quantities is small.

From Eq. (3.4) we can infer the average transmission,

$$T_{\mathrm{avg}}(r_1, r_2) = \frac{T_1 T_2}{1 - R_1 R_2} = \frac{(1 - |r_1|^2)(1 - |r_2|^2)}{1 - |r_1|^2 |r_2|^2} \tag{3.7}$$

and the peak transmission,

$$T_{\mathrm{p}}(r_1, r_2) = \frac{(1 - |r_1|^2)(1 - |r_2|^2)}{(1 - |r_1||r_2|)^2}. \tag{3.8}$$

Extracting T_{avg} and T_{p} from the conductance data (where we again neglect the effects of finite temperature) we obtain r_1 and r_2. In Tab. 3.2 we list the average, the peak transmission, r_1 and r_2.

The average length of the electron path in the interferometer can be calculated by considering the probability to perform n labs, $P_n = (|r_1|^2 |r_2|^2)^n$, multiplied by the path length $2nL$, i.e.,

$$\begin{aligned} l_{\mathrm{avg}} &= L + |r_1|^2 |r_2|^2 2L + \cdots + (|r_1|^2 |r_2|^2)^n n 2L + \cdots \\ &= \left[1 + \frac{2|r_1|^2 |r_2|^2}{(1 - |r_1|^2 |r_2|^2)^2}\right] L. \end{aligned} \tag{3.9}$$

In Tab. 3.2, the average path length l_{avg} is evaluated using the estimation of the reflection parameters r_1 and r_2 from Eq. (3.7) and Eq. (3.8). l_{avg} necessarily imposes a lower limit on the phase relaxation length in the CNT, $L_\phi > l_{\mathrm{avg}}$.

3.2.4 Properties of the Fourier transform

In optics, a Fourier analysis of the transmission spectrum can be used to quantify the quality of an interferometer [98]. The summands T_j of the transmission function in Eq. (3.4),

$$\mathcal{T}(V_\mathrm{g}) = \sum_j T_j(V_\mathrm{g}),$$

are even functions with periodicity π/L. Thus they can be expanded in a Fourier series,

$$T_j(V_\mathrm{g}) = \sum_n \alpha_n \cos(nk_j(V_\mathrm{g})L), \tag{3.10}$$

with coefficients

$$\alpha_n = \frac{L}{\pi} \int\limits_{-\pi/2L}^{\pi/2L} \mathrm{d}k\, T_j(k) \cos(nkL).$$

While the calculation of the coefficients in general is cumbersome, it can be shown that the ratio of two coefficients yields the product of the two reflection coefficients [98],

$$\frac{\alpha_{n+1,L}}{\alpha_{n,L}} = |r_1||r_2|. \tag{3.11}$$

The coefficients can thus be written as

$$\alpha_n = \alpha_0(|r_1||r_2|)^n, \tag{3.12}$$

where $m = n + 1$ is the harmonic order, i.e., $mf_1 = f_m$. For the experimental data we perform the Fourier transform using a sliding window of width 0.4 V. In Fig. 3.6(b) we show the absolute value of the coefficients as a function of frequency obtained from the zero-bias conductance $G(V_\mathrm{g})$ in (a). We identify the fundamental frequency component and up to six higher harmonics. Note that the amplitudes of the harmonics in the FT are oscillating when we change the gate voltage. Since this is not accounted for in Eq. (3.12), we have to average the FT amplitude over a gate voltage range that includes multiple periods of the slow modulation to compare the FT data to Eq. (3.12). To this end, we divide the full gate voltage range into two ranges, [−15 V, −5 V] and [−5 V, −0 V]. Fig. 3.7(a,b) shows fits of Eq. (3.12) to the amplitudes of the Fourier transform.

We extract the product $|r_1||r_2|$ from the slope in Fig. 3.7 and infer another estimate of the average length of the electronic path, $l_\mathrm{avg}^\mathrm{FT}$, from Eq. (3.9), see Tab. 3.2. We note that the path length deduced from the Fourier transform is considerably larger than the path length estimated from peak and average conductance.

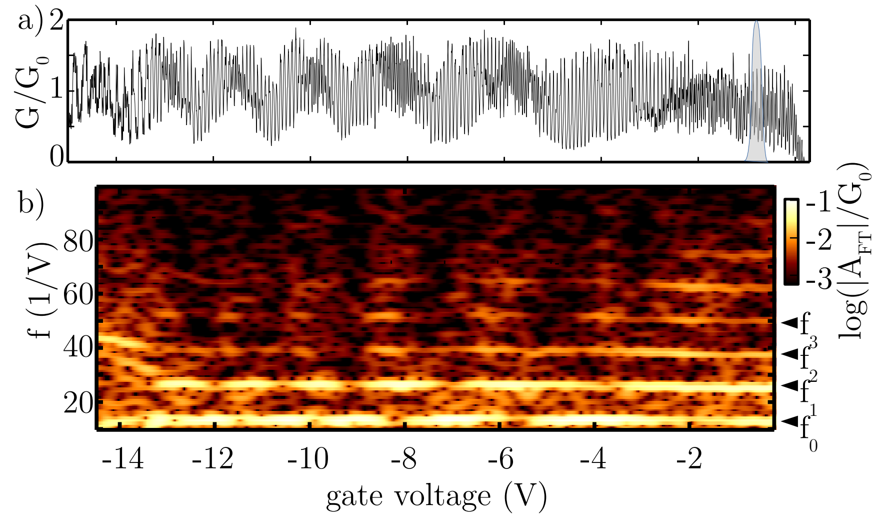

Figure 3.6: (a) $G(V_\mathrm{g})/G_0$ repeated from Fig. 3.2(e) for reference. (b) Absolute values of the Fourier transform amplitudes obtained for a sliding window of width 0.4 V from (a).

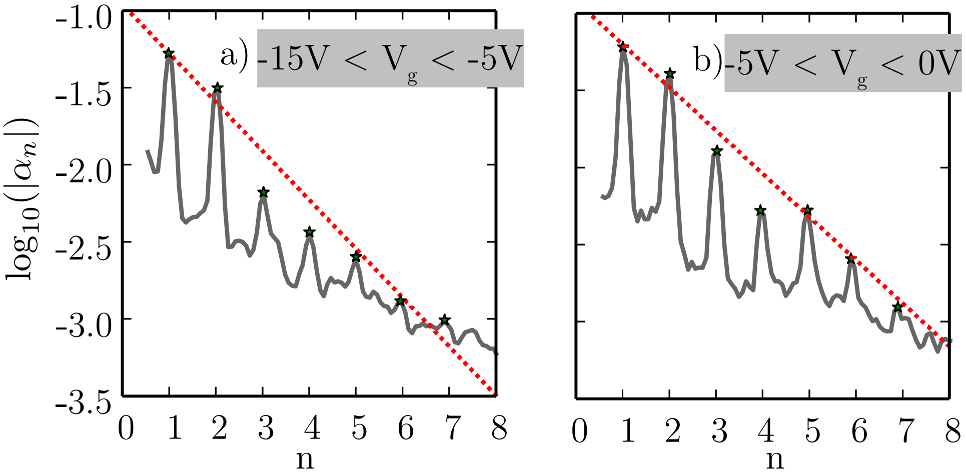

Figure 3.7: FT amplitude obtained from Fig. 3.6 by averaging over regions in the gate voltage (grey line) on a logarithmic scale. Peaks in the graph (highlighted by stars) indicate the positions of the harmonics f_n. The peak positions are used for the fit to Eq. (3.12) (dashed line). (a) Amplitudes averaged over a gate voltage range of $-15\,\mathrm{V} < V_\mathrm{g} < -5\,\mathrm{V}$. (b) Amplitudes averaged over a gate voltage range of $-5\,\mathrm{V} < V_\mathrm{g} < 0\,\mathrm{V}$.

Gate dependent oscillations of the frequency components Another striking feature of the Fourier transform in Fig. 3.6(b) is the modulation of the FT amplitudes α_n with gate voltage. The period of this modulation is the same for the fundamental frequency component and the higher harmonics. When the interfering modes are not mixed, i.e., Eq. (3.4) applies, we can predict the oscillations of the amplitudes of the different frequency components as a function of gate voltage. Let us rewrite the two channel transmission formula for the armchair geometry, Eq. (3.4),

$$\begin{aligned}\mathcal{T}(V_\mathrm{g}) &= T_a(V_\mathrm{g}) + T_b(V_\mathrm{g}) \\ &= \sum_n \left[\alpha_{a,n}\cos(nk_a(V_\mathrm{g})L) + \alpha_{b,n}\cos(nk_b(V_\mathrm{g})L)\right].\end{aligned}$$

Since $\kappa_{a,i} \sim \kappa_{b,i}$ we can assume $k_a \sim k_b$ and $\alpha_{a,n} \sim \alpha_{b,n}$. Then, a minimum of the harmonic term of order n is given by the destructive interference of both waves, i.e.,

$$|k_a - k_b|nL = \pi + 2\pi m$$

for integer m. The period of the modulation of higher harmonics with gate voltage thus decreases with n, i.e.,

$$|k_a(V_\mathrm{g}) - k_b(V_\mathrm{g})|L = \frac{\pi + 2\pi m}{n}. \tag{3.13}$$

This behavior is confirmed in a Fourier analysis of numerical transmission data for a $(7, 7)$ *armchair* CNT, see Fig. 3.8(b).

In the Fourier analysis of numerical transmission data for an *armchair-like* $(10, 4)$ CNT in Fig. 3.8(c,d), the amplitudes of the fundamental component and the higher harmonics all oscillate with the same period. A difference in the FT of the transmission for *armchair* and *armchair-like* CNTs is expected, since we concluded in Sec. 3.2.2 that mode mixing inhibits an application of Eq. (3.7) – the starting point of this analysis. The gate dependent oscillation of the frequency components in the experimental data, Fig. 3.6(b), shows a closer resemblance to the numerical results for the *armchair-like* CNT as expected from the analysis in Sec. 3.2.2. The period in the FT of the experimental data is the same for all frequency components. However, the maxima of the oscillations of the fundamental frequency component in the experimental data are shifted along the gate voltage axis with respect to the higher harmonics (for a maximum in $|\alpha_1(V_\mathrm{g})|$ we find a minimum in $|\alpha_n(V_\mathrm{g})|$, $n > 1$). This is not observed in the numerical result in Fig. 3.8(d).

3.2.5 Open questions

The difference in the length of the average electron path The average length of the electron path is shorter when evaluated directly from the

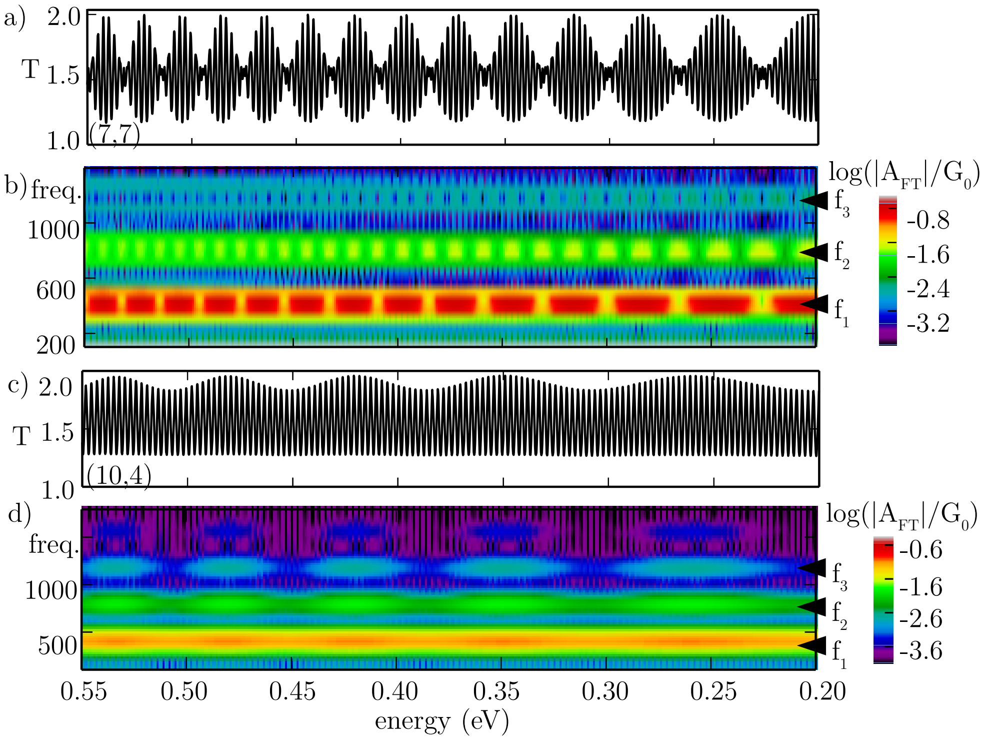

Figure 3.8: Transmission data from tight-binding calculations for a $(7,7)$ *armchair* CNT (a) and a $(10,4)$ *armchair-like* CNT (c). (b) Fourier transform of (a) on a $\log_{10}$-scale obtained from the transmission data using a sliding window of width 0.015 eV. (d) Fourier transform of (b) using a sliding window of width 0.019 eV.

transmission function instead of the decay of the Fourier transform amplitudes, see Tab. 3.2. When considering finite temperatures, the FP resonances are essentially broadened as soon as $k_\mathrm{B}T > \Gamma$ [57]. We thus expect that l_avg decreases since T_p is reduced and T_avg is increased. $l_\mathrm{avg}^\mathrm{LT}$ also decreases since it directly reflects the *non-sinusoidal* shape of the resonances, i.e., the sharpness of the resonances. Preliminary calculations confirm that an increase in temperature can not lead to the observed difference between l_avg and $l_\mathrm{avg}^\mathrm{LT}$.

Another source of error lies in the assumption that Eq. (3.4) is applicable (in principle) to the transmission when channel mixing is present. From this assumption, the equality of l_avg and $l_\mathrm{avg}^\mathrm{LT}$ follows. In the tight-binding results we observe, that for random on-site energies on the contact ring T_p is decreased and T_avg is increased. In Fig. 3.4(a), where the conductance for a *zigzag-like* $(6, 3)$ CNT is shown, the peak transmission is reduced compared to the theoretically expected maximum of $4\,\mathrm{e}^2/h$. On the other hand, in *armchair-like* CNTs the peak conductance and the average conductance remain unaffected, see Fig. 3.3(a). From this qualitative argument it seems likely that mode mixing which is induced by a breaking of the rotational symmetry in the contacts can lead to a decrease in l_avg. Further checks are needed to see if $l_\mathrm{avg}^\mathrm{LT}$ and the ratio between the amplitudes of the harmonics in the FT remains constant when the rotational symmetry is broken in *zigzag-like* CNTs. When this is the case, the difference between $l_\mathrm{avg}^\mathrm{LT}$ and l_avg can be used to distinguish between CNT cavities with intrinsic and extrinsic mode mixing.

The size of the bandgap Note that a bandgap of the size reported in Tab. 3.1, i.e., 66 meV, is not expected as a consequence of the curvature of the CNT. When we estimate the curvature gap for a $(7, 4)$ *armchair-like* CNT ($\theta = 21°$, $R = 3.8\,\text{Å}$) using Eq. (1.11) we obtain a size of the gap of $E_\mathrm{gap} = 31\,\mathrm{meV}$. This value sets an upper bond to the range of curvature induced band-gaps since only CNTs with $R > 4\,\text{Å}$ are considered stable. Typical values for larger radii and chiral angles lie below 10 meV. For the next candidate, the $(8, 5)$ CNT ($\theta = 22°$, $R = 4.5\,\text{Å}$), we obtain already $E_\mathrm{gap} = 20\,\mathrm{meV}$. This deviation of the size of the theoretically estimated curvature gap and the experimentally observed bandgap in nominally metallic CNTs is observed frequently [99]. The authors of Ref. [99] suggest that the bandgap size is dominated by an electron interaction effect. A *Mott* gap due to repulsive electron interaction at half filling can lead to bandgap sizes in the range $10 - 100\,\mathrm{meV}$. Using the relation between the CNT radius r and the size of the *Mott* gap, $\Delta = \beta r^{-1.3}$, we obtain $r \simeq 1\,\mathrm{nm}$.

3.3 Summary

We analyze wave interference effects in the electronic transport spectrum of a strongly coupled CNT. We focus on the low-bias conductance at low temperature. We start our analysis from a simple plane wave model for the FP interference in CNTs. From basic arguments we follow that the symmetries present in different CNT classes strongly affect the FP interference pattern. Under the assumption that the contact interfaces between metal and CNT do not break the rotational symmetry of the CNT, *zigzag* and *zigzag-like* CNT cavities only show conventional Fabry Perot interference, the *primary* interference. *Armchair* and *armchair-like* CNTs reveal additional periodic modulations with a larger period, the *secondary* interference. Specifically, a beat or beating is predicted for *armchair* CNTs where the two independent cavity modes acquire different phases due to a change in bias or gate voltage, and a slow oscillation of the average transmission is expected in *armchair-like* CNTs. The latter arises due to the mixing of transport channels which is an intrinsic feature of the *armchair-like* geometry. The predictions from the simple model are confirmed in numerical tight-binding calculations for all CNT classes. When we brake the rotational symmetry of the contact interface in the numerical model for *zigzag-like* CNTs, secondary interference can be observed in this class as well. The evolution of the period of this interference pattern as a function of gate voltage strongly suggests that this effect can be related to channel mixing, similar to what we observe in the *armchair-like* class.

The period of the secondary interference depends on the evolution of the phase difference between the two modes. This evolution, in turn, is governed by the trigonal warping of the dispersion relation. The effect of the trigonal warping on the one-dimensional dispersion relation increases with chiral angle and is strongest in armchair CNTs.

In the second part of the chapter we apply our analysis to experimental data. In the zero-bias conductance we observe a superimposed *slow* modulation in the conductance with a period of $10-20$ times the period of the fast *primary* oscillation. This modulation is also reflected in an oscillation of the average conductance. In the spirit of our analysis we estimate the chiral angle, $22^\circ \leq \theta < 30^\circ$, from the period of the slow modulation. The accuracy of this estimate is governed by uncertainties in the conversion from gate voltage values to the energy scale used in the model, and by the precision of the tight-binding overlap energy t.

As a side note, we comment on the Fourier transform of CNT FP cavities and infer the average electronic path length from the decay of the amplitudes of the higher harmonics.

Chapter 4

Loose ends: CNT transport data to be still analyzed

In this chapter we present data recorded in the strong coupling regime that is not yet analyzed. The measurements are conducted with two samples, AD_CB14 (I) and CB3224 (II) at low temperatures. The fabrication details for (I) can be found in the appendix, Sec. 4.D together with the characteristics of the transport in the FP regime in Sec. 4.E. The second sample (II) was fabricated by P. Stiller (cf. Sec. 2.B) and the measurements were conducted by D. R. Schmid, P. Stiller and the author in the course of three different experiments: Data recorded in February 2011 at 300 mK in a He^3 cryostat is labeled (IIa), data recorded in October and November 2011 in a dilution fridge at different temperatures is labeled (IIb) while data recorded in July 2012 in a dilution fridge at 30 mK is labeled (IIc). Refer to Tab. 4.1 for an overview. The data discussed in Sec. 1.2.3 resulted from the experiment (IIc).

experiment	sample	date	researchers	temperature
(I)	AD_CB14	Oct. 13	AD	15 mK
(IIa)	CB3224	Feb. 11	PS, DS	300 mK
(IIb)	CB3224	Oct. 11	PS, DS	var.
(IIc)	CB3224	Jul. 12	DS, AD	30 mK

Table 4.1: The different experiments performed on the samples AD_CB14 and CB3224. PS is a shortcut for P. Stiller, DS stands for D. R. Schmid and AD for the author of the thesis.

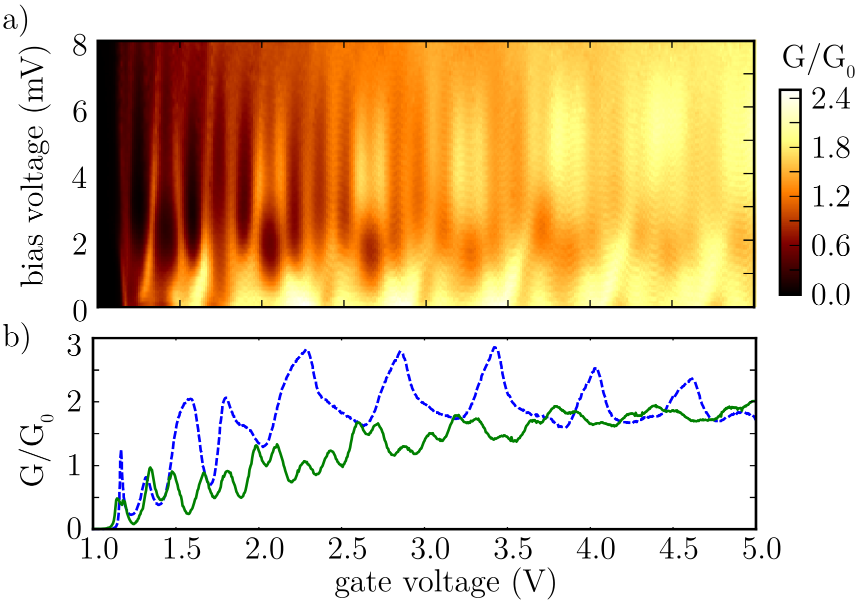

Figure 4.1: (a) $G(V_{\mathrm{g}}, V_{\mathrm{b}})$ for finite bias in the electron transport regime in (I). (b) Linetraces from (a) at $V_{\mathrm{b}} = 0\,\mathrm{V}$ (blue dashed line) and at $V_{\mathrm{b}} = 5\,\mathrm{mV}$ (green solid line). The zero-bias graph resembles the corresponding graph on the hole side, see Fig. 4.E.1. The graph at finite bias clearly oscillates with a period $\sim 0.1 - 0.2\,\mathrm{V}$ along the gate voltage axis.

4.1 Conductance oscillations in the Fabry-Perot regime at finite bias

In this section, solely data from (I) is discussed. In Fig. 4.1(a) we observe conductance oscillations as a function of the gate voltage that can not straightforwardly be related to the Fabry-Perot cavity behavior. These oscillations with a period $\sim 0.1 - 0.2\,\mathrm{V}$ are not prominent in the zero-bias conductance, Fig. 4.1(b, blue dashed line), while for finite bias, $2\,\mathrm{mV} \leq V_{\mathrm{b}} \leq 8\,\mathrm{meV}$, they are clearly visible, see Fig. 4.1(b, green line). Additional higher frequency components in a *zero-bias* Fabry-Perot interference pattern that do not coincide with the usual hierarchy of harmonics, $f_n = nf_1$, can be attributed to additional scattering centers along the CNT.

However, the Fourier transform of the zero-bias signal, Fig. 4.E.2(b) does not show prominent higher frequency components. That this feature clearly depends on the bias voltage can be seen in Fig. 4.2(a,b). In (a), we plot the FT amplitudes of linetraces taken along the gate voltage axis in the range $1\,\mathrm{V} < V_{\mathrm{g}} < 10\,\mathrm{V}$ for different values of the bias voltage. The

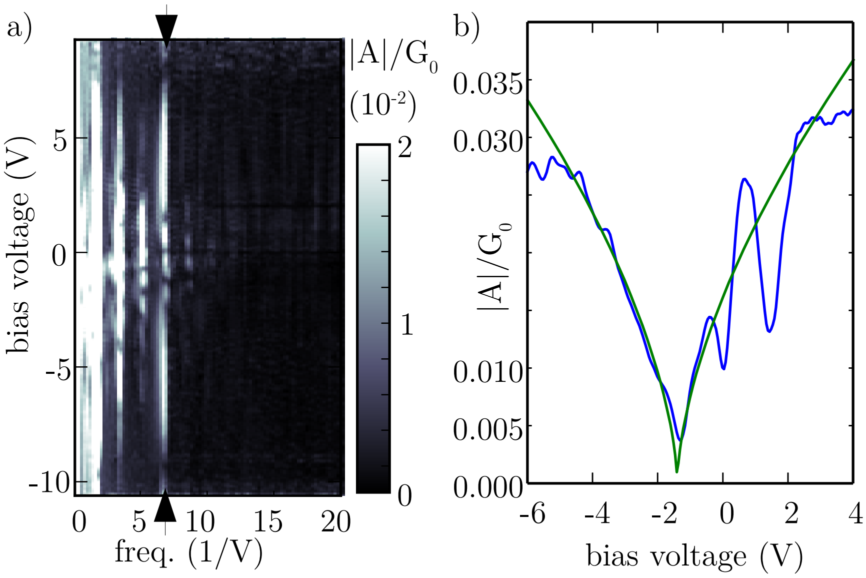

Figure 4.2: (a) FT amplitudes of linetraces in $G(V_\mathrm{g}, V_\mathrm{b})$ in the range $1\,\mathrm{V} < V_\mathrm{g} < 10\,\mathrm{V}$ for different bias voltages in (I). The peculiar component corresponding to the fast oscillations in Fig. 4.1 is marked by small arrows. (b) Linetrace of (a) along the bias voltage axis for the frequency component marked by the little arrows in (a) (blue line). The green line is a fit to a function $(V_\mathrm{b} - \Delta V_\mathrm{b})^\alpha$ with $\alpha = 0.61$.

component corresponding to the fast oscillations is highlighted and we note that it does not follow the same evolution as the harmonics of the FP cavity interference although its frequency lies very close to the fourth harmonic. The FP interference amplitudes decay for finite bias voltage and are maximal in the vicinity of zero bias. In Fig. 4.2(b) we plot a linetrace of (a) for the highlighted component with a frequency of $f^* = 6.6\frac{1}{\mathrm{V}}$.

In the spirit of the Fabry-Perot analysis of the previous chapter we interpret the pattern as a interference of electron waves in a CNT of length L. In this case, the corresponding waves travel at velocities $\tilde{v} = v_\mathrm{F} * f^*/f_1 = 3.1 \cdot 10^6\,\mathrm{m/s}$ according to Eq. (4.11). As a function of bias voltage, we observe a power law suppression of the f^* component, i.e., $G \sim V_\mathrm{b}^\alpha$. We fit the amplitude of the f^* component in Fig. 4.2(b, blue line) using the function $(V_\mathrm{b} - \Delta V_\mathrm{b})^\alpha$ and obtain $\alpha = 0.61$. ΔV_b accounts for the offset in bias voltage which appears due to the current-voltage amplifier used in the measurement setup.

Such a power-law suppression is also observed in interacting one-dimensional electron systems that form a *Luttinger liquid*(LL) [40]. Within this interpretations, the observed interference pattern stems from plasmon waves that travel at velocities $\tilde{v} = v_\mathrm{F}/g$, where g is proportional to the strength of the interaction. Following this argument we find $g = 0.26$. According to Ref. [40], the exponent α that governs the power law suppression of the plasmon excitations with bias voltage is in this case given by $\alpha = (1/g - 1)/4$. Again, we obtain a similar value, $g = 0.29$.

Although tempting, the interpretation of the f^* oscillations as a result of the formation of a LL does not hold. A LL requires a continuous spectrum of electron states [100]. Thus, to observe features related to the LL, the quantization energy $\epsilon_0/g \simeq 12\,\mathrm{meV}$, see Sec. 4.E, is required to be small with respect to eV_b [101]. In our experiment, the f^* oscillations emerge already at $\sim 3\,\mathrm{mV}$. At this point we can not give a satisfactory explanation of the observations. It would be interesting to measure $G(V_\mathrm{g}, V_\mathrm{b})$ at different temperatures to check if the linear conductance is suppressed with temperature, too.

4.2 A 0.7-like feature to the left of the bandgap

The 0.7 anomaly is a famous effect in quantum transport. By increasing a local gate that determines the potential of a quantum point contact (QPC) between two reservoirs, the conductance decreases stepwise by $2e^2/h$. When the last channel of a quantum point contact is closed, the conductance does not show a clean step but exhibits a shoulder at a height of $0.7 \cdot 2e^2/h$ [102]. The shoulder is sensitive to magnetic field and temperature and is accompanied by a zero-bias peak (ZBP), much like the Kondo effect [103]. We discuss data

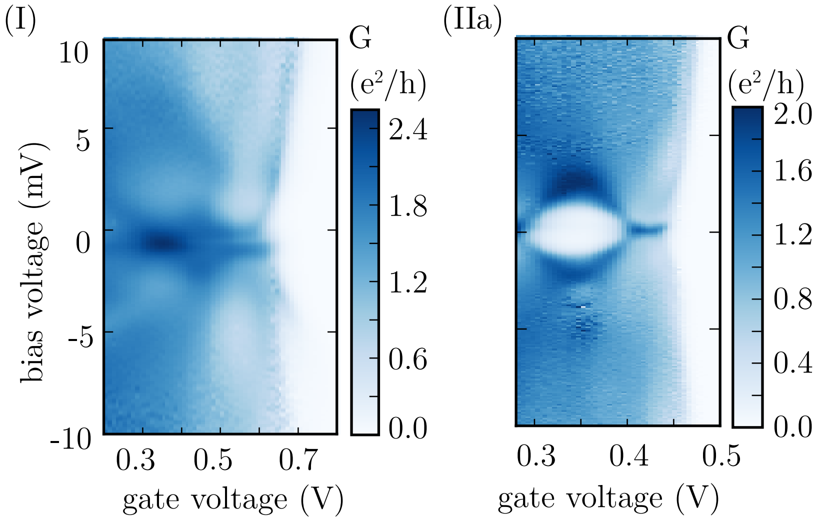

Figure 4.1: $G(V_\mathrm{g}, V_\mathrm{b})$ to the left of the bandgap for experiment (I) and (IIa). In (I), no Coulomb blockade is observed and the device enters the FP regime directly. In (IIa), a Coulomb blockade diamond is observed at $V_\mathrm{g} \simeq 0.35\,\mathrm{V}$.

from (I), (IIa), (IIb) and (IIc) in the light of the 0.7 anomaly. The stability diagram in the region of interest, i.e., close to the bandgap on the hole side, is shown for (I) and (IIa) in Fig. 4.1. The analysis will remain on a qualitative level and is not sufficient to prove that the observed effect can indeed be mapped to its QPC analogue straightforwardly.

4.2.1 Magnetic field behavior

In measurements of the 0.7 anomaly in QPCs the magnetic field is always oriented in-plane with the 2DEG of the reservoirs. In CNTs, the field parallel to the axis affects the bandstructure considerably (cf. Sec. 1.2.3) and the 0.7-like behavior is difficult to identify. Therefore, we analyze data that is recorded with the magnetic field perpendicular to the CNT axis.[1] The zero-bias conductance at $T \simeq 30\,\mathrm{mK}$ does not reach the theoretical limit of $4e^2/h$ in both samples. To compare the behavior to the QPC we relate the conductance to its maximum in the observed range, G_max Without magnetic field, the conductance in (I) shows a clear shoulder at $\sim 0.7 \cdot G_\mathrm{max}$ approaching the bandgap from the hole side, see Fig. 4.2(I). The shoulder is getting more pronounced when the field is increased and eventually forms a peak at

---

[1] The setup allows for a rotation of the magnetic field in the plane of the sample surface. Data recorded in the presence of parallel magnetic field is available, too.

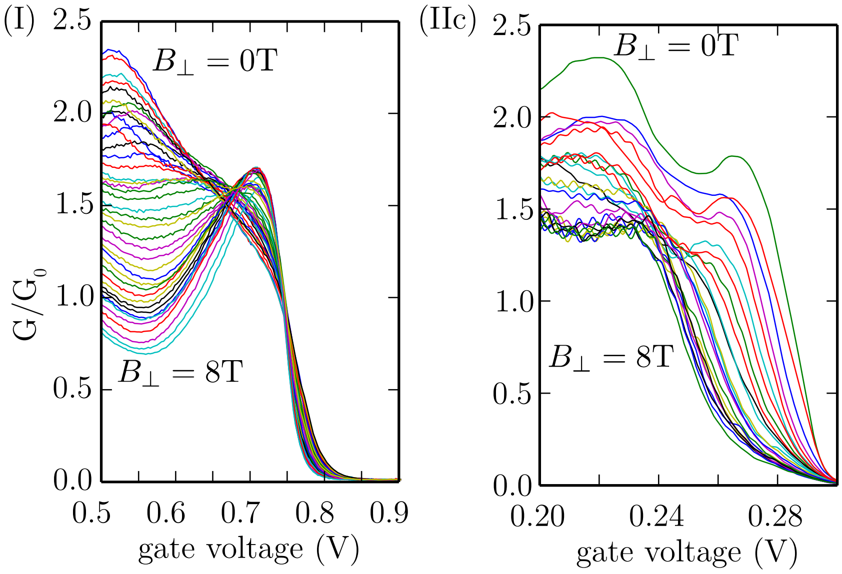

Figure 4.2: $G(V_\mathrm{g})$ for different equidistant magnetic field values in the range 0 T (top line) to 8 T (bottom line). The magnetic field is oriented perpendicular to the nanotube axis. (I): A shoulder can be clearly observed at $\sim 0.7 G_\mathrm{max}$ which turns into a step for ~ 4 T. At 8 T, a dip is followed by a peak. (IIc): The zero-field signature resembles more a step at $\sim 0.7 G_\mathrm{max}$ than a shoulder. With increasing field the step transforms into a plateau at $\sim 0.6 G_\mathrm{max}$.

$\sim 0.7 \cdot G_\mathrm{max}$ followed by a dip at $\sim 0.4 G_\mathrm{max}$. Up to ~ 4 T, the behavior is in agreement with experimental observations of the 0.7 anomaly in QPCs where the conductance is expected to exhibit an additional step at $0.5 \cdot G_\mathrm{max}$ due to spin-splitting [104]. The dip-peak feature at high fields, however, is not observed in the QPC.

In Fig. 4.2(IIc), the signature is less pronounced and clear. At zero field, a step is observed at $\sim 0.7 G_\mathrm{max}$ and the conductance decreases with increasing field eventually forming a plateau at $\sim 0.6 G_\mathrm{max}$.

4.2.2 Temperature dependence

Measurements with varying temperature where only conducted in (IIb), see Fig. 4.3. Note that the curve for $T = 30$ mK is only roughly similar to the curve for $B_\perp = 0$ T from experiment (IIc) in Fig. 4.2, a clear indication that the transport properties of the sample changed over time. At low temperature, we observe a clean shoulder at $\sim 0.7 G_\mathrm{max}$ which deepens for increasing

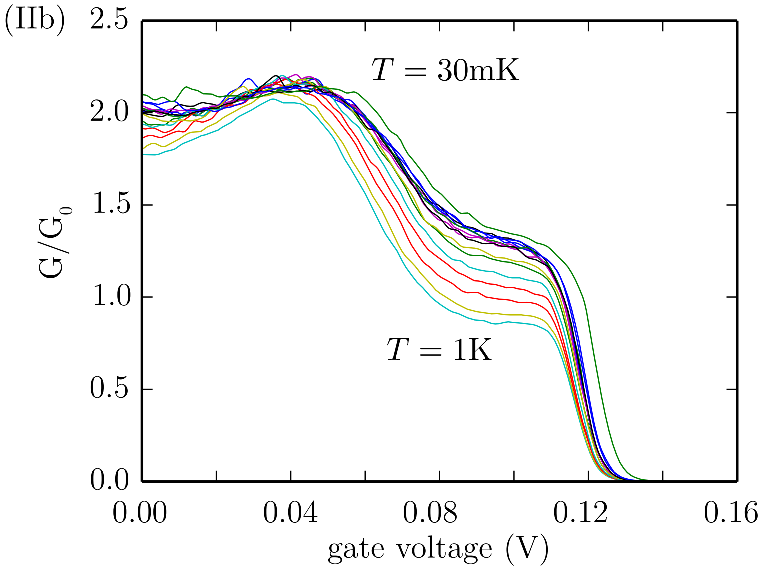

Figure 4.3: $G(V_\mathrm{g})$ in the vicinity of the bandgap for different temperatures in the range $30\,\mathrm{mK} \lesssim T \lesssim 1\,\mathrm{K}$ in experiment (IIb). The shoulder is getting more pronounced with increasing temperature.

temperature. The signature is clear and agrees nicely with observations for the QPC [102].

4.2.3 Zero-bias peak

Along the bias axis, a peak is observed in $G(V_\mathrm{g}, V_\mathrm{b})$ at the top of the first step in the conductance in QPCs [102]. In the data of (I) in Fig. 4.4, the ZBP clearly appears (slightly offset by $V_\mathrm{b} = 0.66\,\mathrm{V}$ as can be seen from Fig. 4.1(I)). It is accompanied by satellite peaks at $V_\mathrm{b} \sim \pm 3\,\mathrm{mV}$, another reminiscence of the Kondo effect [17]. There is no data available on how the ZBP and the satellites evolve with magnetic field. Surprisingly, the ZBP evolves from a split-peak into a single one at $V_\mathrm{g} = 0.4\,\mathrm{V}$ which is not a common feature in QPC data [102]. In Fig. 4.5, the ZBP in (IIa) is plotted. Here, the peak conductance in the vicinity of the bandgap is smaller, $G_\mathrm{max} \sim 2e^2/h$. Prior to the evolution of the ZBP at $V_\mathrm{g} \simeq 0.42\,\mathrm{V}$, there are again tiny satellite peaks visible at $V_\mathrm{b} \sim \pm 3\,\mathrm{mV}$. At $V_\mathrm{g} \simeq 0.4\,\mathrm{V}$, the peak splits due to the CB charging state, compare Fig. 4.1(IIa).

(I)

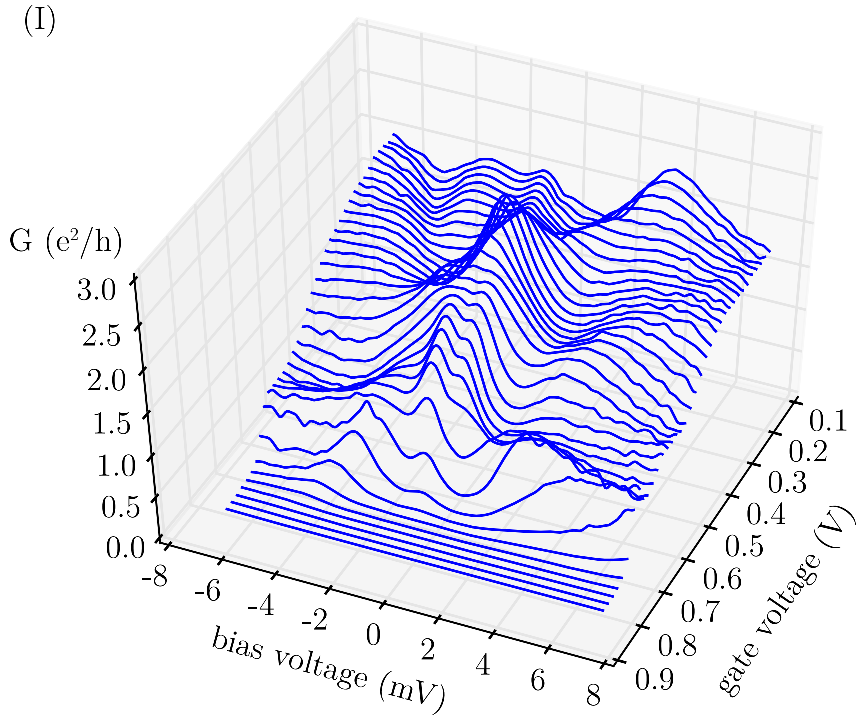

Figure 4.4: $G(V_\mathrm{b})$ for different values of V_g in a series of line plots. (I) shows a prominent ZBP which emerges from a split-peak at $V_\mathrm{g} = 0.4\,\mathrm{V}$. Between the ZBP and the bandgap, satellite peaks appear at $V_\mathrm{b} \sim \pm 3\,\mathrm{mV}$ and $V_\mathrm{g} \simeq 0.65\,\mathrm{V}$ (cf. Fig. 4.1(I)).

(IIa)

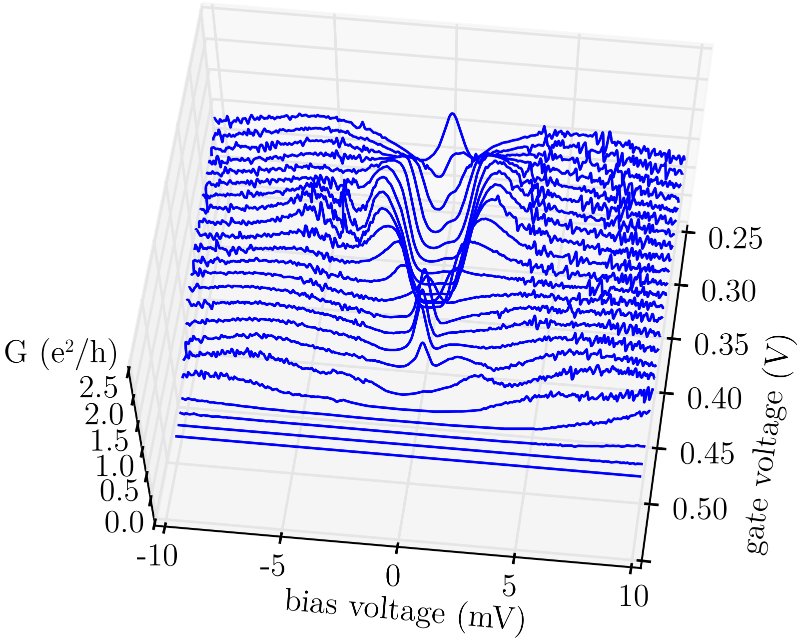

Figure 4.5: $G(V_\mathrm{b})$ for different values of V_g in (IIa). The conductance data exhibits two small satellite peaks at $V_\mathrm{b} \sim \pm 3\,\mathrm{mV}$ and $V_\mathrm{g} \simeq 0.45\,\mathrm{V}$ before the ZBP emerges when we decrease the gate voltage starting from the bandgap. When we decrease V_g further starting from the ZBP, the peak splits again due to the CB charging state, compare Fig. 4.1(IIa).

Appendix

4.A Details on the tight-binding calculations

For the numerical calculations M. del Valle uses a tight-binding Hamiltonian for the description of the CNT. Interactions up to first-nearest neighbors are considered and the model is restricted to one $2p$ orbital per atom. The $2p$ orbitals give rise to the π and π^* bands, which are responsible for the CNT's conduction as the next molecular orbitals lie energetically far apart.

The Hamiltonian describing our systems reads

$$H_0 = \sum_i \epsilon_{2p} c_i^\dagger c_i + \sum_{\langle i,j \rangle, i \neq j} t_{ij} c_i^\dagger c_j, \tag{4.1}$$

where the indices $\langle i, j \rangle$ indicate nearest neighbor atom sites and the summation is extended over all points in the lattice. The transfer integrals ϵ_{2p} serve as the onsite energies and t_{ij} are the hopping parameters. Our energy scale is shifted in order to have vanishing on-site energies, setting $\epsilon_{2p} = 0$. The Tománek-Louie parametrization for graphite up to nearest-neighbor interactions is used, including the hopping parameter $t = -2.66\,\mathrm{eV}$ [105]. This parametrization set includes also the σ molecular orbitals, and has been proven to be a consistent parameter set. The σ orbitals mix with the π molecular orbitals due to the finite curvature. To account for curvature and include also spin-orbit effects in the calculations, a set of parameters containing the Slater-Koster hopping integrals for the different molecular orbitals is included. The transfer integrals describing the hopping between nearest neighbors are not given by constants any more but depend on the relative three-dimensional position of the atoms, and on the strength of the spin-orbit interaction. The derivation of these transfer integrals can be found in Ref. [106], together with the spin-orbit coupling parameter used in our numerical calculations. The finite curvature and the spin-orbit interaction do not affect the main secondary interference pattern in the numerical results. For simplicity, calculations in the main text do not include these effects.

Coherent transport in finite CNTs is calculated within the Landauer

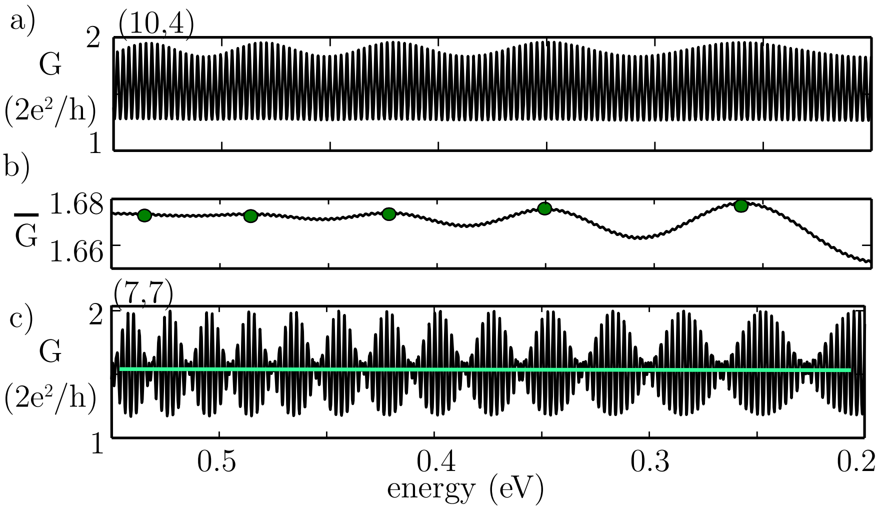

Figure 4.A.1: (a) Conductance of an armchair-like (10,4) CNT ($L = 660\,\mathrm{nm}$) from tight-binding calculations including curvature and spin-orbit effects. The secondary interference pattern, i.e., a modulation of the conductance over a period of $0.05 - 0.10\,\mathrm{eV}$, is evident. (b) Average value of (a) obtained using a $0.019\,\mathrm{eV}$-wide sliding window. Slow oscillations of the average conductance values are clearly visible. The peak positions are marked by filled circles. (c) Transmission of a (7,7) armchair CNT ($L = 660\,\mathrm{nm}$) from tight-binding calculations including curvature and spin-orbit effects. The average is constant (green line).

approach using real-space Green's functions [107]. The finite length requires the application of decimation techniques to reduce computational costs [108]. The barriers at the interfaces with the leads are modelled by considering a reduced hopping parameter $t^{c}_{ij} = 0.73t_{ij}$ and an enlarged onsite energy $\epsilon_{2p} = 0.1\,\mathrm{eV}$ for the atoms on the ring that forms the contact to the leads. This model of the barriers has been used successfully in real-space transport calculations in the Fabry-Perot regime [109]. Unless specified otherwise, all on-site energies on the contact ring are equal in the numerical results shown in the main text. Thus, the barriers respect the symmetries (rotational, parity) of all CNTs.

In Fig. 4.A.1(a) we show the results for the transmission of a $(10, 4)$ armchair-like CNT with a length $L = 660\,\mathrm{nm}$. The secondary interference pattern can be observed. The sliding average of the transmission in (b) follows the slow modulation of the transmission signal. Contrarily, the transmission through the $(7, 7)$ armchair nanotube in Fig. 4.A.1(c) exhibits a beat, and the sliding average (green line) is constant, just as it is observed for CNTs where curvature and spin-orbit effects are not included.

4.B Evaluation of the gate voltage lever arm

We can analyze the conductance data by considering energy conservation of the transmitted electrons, similar to the analyis carried out for the weakly coupled quantum dot in Sec. 1.1. Note, however, that our understanding of the two regimes is quite different: In the sequential tunneling picture, an incident electron tunnels into a state on the quantum dot, looses its phase memory and tunnels out of the dot. The electron-electron interaction is important due to the small capacitance of the quantum dot. The related energy scale, the charging energy E_c, is large compared to the effective coupling energy and the thermal energy. This leads to quantization in the charge occupancy of the quantum dot. On the other hand, in the regime with highly transparent contacts, the fluctuations in the conductance are governed by electron wave interference and theoretical modeling is best done in terms of scattering states or Green's functions. This difference between the two pictures is discussed in more detail in Ref. [26], Ch. 6.

The energy of an electron on the CNT with respect to the potential of the unbiased contact is given by

$$E(V_\mathrm{g}, V_\mathrm{b}) = \eta e V_\mathrm{b} - \alpha e V_\mathrm{g}, \tag{4.2}$$

$$E(V_\mathrm{g}, V_\mathrm{b}) = -(1-\eta) e V_\mathrm{b} - \alpha e V_\mathrm{g}, \tag{4.3}$$

when injected from source or drain contact, respectively. $\eta e V_\mathrm{b}$ is the energy

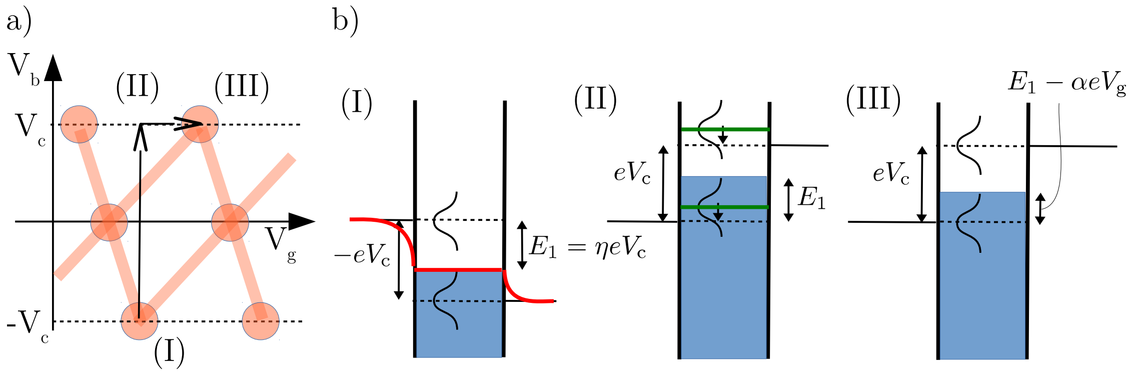

Figure 4.B.1: Resonant transport in the ballistic regime. (a) Schematic of the conductance as a function of gate and bias voltages. The filled circles highlight regions where both electrons from the source and from the drain contact resonate within the cavity. Along the lines that connect the circles, only one resonance condition is met. (b) Energy band diagrams for the three coordinates highlighted by (I-III) in (a). (I) At this point, both source and drain electrons are resonant. Note that the finite bias affects the bottom of the band in the CNT as indicated by the red line. (II) We increase the bias voltage by $2V_c$. Note that the energy of the electron on the CNT is changed by $2E_1 = eV_b$. Due to the asymmetric drop neither of the resonant conditions is met. (III) We shift the CNT band by changing the gate voltage to recover the two resonance conditions.

difference of the electrostatic potential between source contact and CNT. This potential follows the quasi-Fermi level of the system within one screening length in the metallic contacts [26]. The variation of the electrostatic potential across the system is indicated by a red line in Fig. 4.B.1(b, I). In this approximation we neglect the potential due to extra charges on the nanotube. This potential becomes important at comparably large bias voltages $> 50\,\mathrm{meV}$ where it determines the threshold voltage of a CNT that is operated as a field effect transistor [22]. We also assume that the capacitances between the contacts and the nanotube are negligible compared to the capacitance of the backgate. In a careful analysis, all capacitances in the system and the potential due to extra charges are used in the Poisson equation to iteratively compute a *self-consistent* potential of the electrons on the nanotube [3].

When we change the bias, the electrostatic potential of the nanotube is modified as well. In Fig. 4.B.1(b, I), we start from a resonant coordinate in the $G(V_b, V_g)$-plane and increase the bias by $2V_b$. Due to an asymmetric drop $\eta \neq 0.5$, the resonance condition which depends on the electrostatic potential is not met in Fig. 4.B.1(b, II). We can shift the CNT bands by changing the gate voltage to recover the resonance, see Fig. 4.B.1(b, III). Note that we choose $\eta \neq 0.5$ here to keep the discussion general. The potential drop can be explained by the formation of a resisitivity dipole in the contacts which is symmetric and we can assume $\eta = 0.5$ [26].[2]

Let us assume that we change the gate voltage from one point $V_{\mathrm{g},1}$ where the resonance condition is met to the next point $V_{\mathrm{g},2}$, i.e., the roundtrip phase in channel j changes by $|\phi_j(V_{\mathrm{g},1}, V_{\mathrm{b}} = 0\,\mathrm{V}) - \phi_j(V_{\mathrm{g},2}, V_{\mathrm{b}} = 0\,\mathrm{V})| = 2\pi$. The energy of the electron on the CNT is changed by $\Delta E = \alpha|V_{\mathrm{g},1} - V_{\mathrm{g},2}|$. Now, we keep the gate voltage constant and move from a point in the stability diagram where the resonance condition is met for negative bias, $(V_{\mathrm{g}}, V_{\mathrm{b}} = -V_{\mathrm{c}})$, to the point where the condition is met for positive bias values, i.e., $|\phi_j(V_{\mathrm{g}}, -V_{\mathrm{c}}) - \phi_j(V_{\mathrm{g}}, V_{\mathrm{c}})| = 2\pi$, where we assume $\eta = 0.5$. Along this line we change the energy of the incident electron by $\Delta E = 2eV_c/2$. This enables us to infer the gate voltage lever arm α from the width and from the half of the height of the resonant pattern in the $G(V_{\mathrm{b}}, V_{\mathrm{g}})$-plane,

$$\alpha = \frac{V_c}{(V_{\mathrm{g},1} - V_{\mathrm{g},2})}. \tag{4.4}$$

4.C A simple transfer matrix approach to secondary interference

Using a simple (non-unitary) transfer matrix description of the system [110], we can understand the evolution of the slow modulation of the conductance in armchair-like CNTs from the mixing of the channels upon reflection at the contacts. We consider two waves in the channels a and b before and after the scattering event. For simplicity, we consider only one pair of incident waves from one side of the cavity and one pair of outgoing waves on the other side of the cavity. Since we do not study the full scattering problem, which would include both in- and out-going waves on both sides of the cavity, the amplitudes can not be related to probabilities. The initial and final states are represented by the vectors

$$|i\rangle = \begin{pmatrix} a \\ b \end{pmatrix} \quad \text{(initial)} \qquad \text{and} \qquad |f\rangle = \mathbf{M}|i\rangle \quad \text{(final)},$$

where $\mathbf{M}$ is a (complex) two-by-two transfer matrix and a and b are complex numbers characterizing the plane waves before entering the cavity. Although

---

[2] For positive gate voltages the quantum dot is seperated from the leads by Schottky barriers. These barriers can induce largely asymmetric voltage drops.

$\mathbf{M}$ is not describing the full scattering problem, the squares of the amplitude of the transmitted wave $|f\rangle$ in the two channels reproduce the transmission $\mathcal{T}$, i.e.,

$$\mathcal{T} \propto \sum_{ij} |\mathbf{M}_{ij}|^2. \tag{4.5}$$

$\mathbf{M}$ is constructed from a product of matrices which describe the effect of different elements of the cavity on the wave function. In particular, the transmission through the (symmetric) left and right barriers is described by matrices

$$\mathbf{T} = \mathbf{T}_\mathrm{l} = \mathbf{T}_\mathrm{r} = \begin{pmatrix} t & 0 \\ 0 & t \end{pmatrix},$$

where the coefficients t are real for simplicity. Passing through the CNT we acquire gate voltage dependent phases $\phi_a(V_\mathrm{g})$ and $\phi_b(V_\mathrm{g})$ in the two modes, respectively:

$$\mathbf{T}_\mathrm{c} = \begin{pmatrix} \mathrm{e}^{\mathrm{i}\phi_a} & 0 \\ 0 & \mathrm{e}^{\mathrm{i}\phi_b} \end{pmatrix}.$$

The reflection at the two interfaces is described by

$$\mathbf{R} = \mathbf{R}_\mathrm{l} = \mathbf{R}_\mathrm{r} = \begin{pmatrix} r & r' \\ r' & r \end{pmatrix},$$

where the reflection coefficients r and r' are real numbers and r' induces a *mixing* of the channels.

We calculate $\mathbf{M}$ taking into account two different electron paths in the cavity. This is the minimal ingredient to observe wave interference in the transmitted signal. The first electronic path is one where the electron is directly transmitted, while in the second path it travels one lap before leaving the cavity. The transfer matrix reads

$$\mathbf{M} = \mathbf{T}\mathbf{T}_\mathrm{c}\mathbf{T} + \mathbf{T}\mathbf{T}_\mathrm{c}\mathbf{R}\mathbf{T}_\mathrm{c}\mathbf{R}\mathbf{T}_\mathrm{c}\mathbf{T} = \mathbf{T}\mathbf{T}_\mathrm{c}(\mathbb{1} + \mathbf{R}\mathbf{T}_\mathrm{c}\mathbf{R}\mathbf{T}_\mathrm{c})\mathbf{T}. \tag{4.6}$$

When we relate $\mathbf{M}$ to the transmission using Eq. (4.5), the matrices $\mathbf{TM}$ and $\mathbf{T}$ outside the bracket only add global phases and amplitudes to the diagonal elements. The global phases vanish when taking the absolute values and the global amplitudes are not important for our argument. Evaluating the part in brackets in Eq. (4.6), we obtain

$$\mathbb{1} + \mathbf{R}\mathbf{T}_\mathrm{c}\mathbf{R}\mathbf{T}_\mathrm{c} = \begin{pmatrix} 1 + r^2\mathrm{e}^{2\mathrm{i}\phi_a} + r'^2\mathrm{e}^{\mathrm{i}(\phi_a+\phi_b)} & rr'(\mathrm{e}^{\mathrm{i}(\phi_a+\phi_b)} + \mathrm{e}^{\mathrm{i}2\phi_b}) \\ rr'(\mathrm{e}^{\mathrm{i}(\phi_a+\phi_b)} + \mathrm{e}^{\mathrm{i}2\phi_b}) & 1 + r^2\mathrm{e}^{2\mathrm{i}\phi_b} + r'^2\mathrm{e}^{\mathrm{i}(\phi_a+\phi_b)} \end{pmatrix}. \tag{4.7}$$

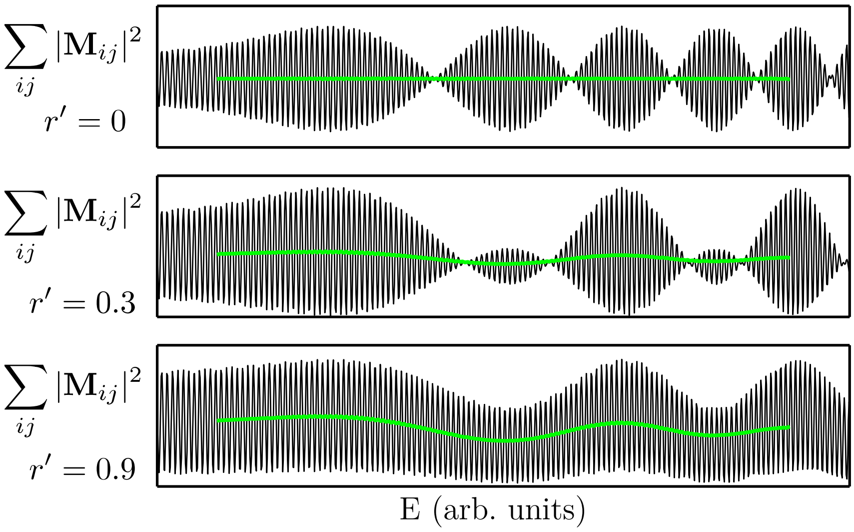

Figure 4.C.1: The sum $\sum_{ij} |\mathbf{M}_{ij}|^2$ plotted as a function of energy in arbitrary units. The green line is the sliding average of the black line. $\phi_a(V_\mathrm{g})$ and $\phi_b(V_\mathrm{g})$ are given by second order polynomials with slightly different quadratic prefactor. (a) $r' = 0$, no mode mixing occurs and a beat can be observed. The sliding average is constant. (b,c) Mode mixing is increased to $r' = 0.3$ (b) and to $r' = 0.9$ (c). The off-diagonal terms induce a slow modulation of the signal that is reflected also in the sliding average.

In the pure armchair case $r' = 0$, so we end up with a diagonal matrix and obtain, using Eq. (4.5),

$$\mathcal{T} \propto \sum_{n=1}^{2} |[\mathbb{1} + \mathbf{R}\mathbf{T}_\mathrm{c}\mathbf{R}\mathbf{T}_\mathrm{c}]_{nn}|^2 = 2\left\{1 + r^4 + r^2\left[\cos(2\phi_a) + \cos(2\phi_b)\right]\right\}, \quad (4.8)$$

where $[M]_{ij}$ refers to the matrix element M_{ij}. The transmission can be identified as a beat of two waves with phases $\phi_a \neq \phi_b$ as a function of the gate voltage.

When we allow for $r' \neq 0$, the square of the absolute values of a diagonal entry of the matrix in Eq. (4.7),

$$\begin{aligned}\left|\left[\mathbb{1} + \mathbf{R}\mathbf{T}_\mathrm{c}\mathbf{R}\mathbf{T}_\mathrm{c}\right]_{11}\right|^2 &= 1 + r^4 + 2r^2\cos(2\phi_a) + 2r'\cos(\phi_a + \phi_b) \\ &\quad + 2r^2 r'^2 \cos(\phi_a - \phi_b) + \mathcal{O}(r'^4), \qquad (4.9)\end{aligned}$$

is proportional to the cosine of the phase difference $\phi_a - \phi_b$. Note that the off-diagonal entries,

$$\left|\left[\mathbb{1} + \mathbf{R}\mathbf{T}_\mathrm{c}\mathbf{R}\mathbf{T}_\mathrm{c}\right]_{12}\right|^2 = \left[\mathbb{1} + \mathbf{R}\mathbf{T}_\mathrm{c}\mathbf{R}\mathbf{T}_\mathrm{c}\right]_{21} = 2r^2 r'^2 \left(1 + \cos(\phi_a - \phi_b)\right), \quad (4.10)$$

contain these phase differences, too. They are responsible for the slow oscillation of the conductance and its sliding average.

In Fig. 4.C.1 we plot $\sum_{ij} |\mathbf{M}_{ij}|^2$ as a function of energy for different values of r'. To obtain the plots, we write the function $\phi_j(E)$ as a second order polynomial with a slightly different coefficient in front of the quadratic term for the two channels j. In Fig. 4.C.1(a), the mixing is absent, $r' = 0$, and Eq. (4.8) shows a beat. The hull curve evolves with a phase $\phi_a - \phi_b$, see Fig. 4.C.1(a), exhibiting two maxima of transmission within one period. The average of the transmission calculated over a few periods of ϕ_a or ϕ_b is constant since both constituents of the transmission function bear a constant average. In (b), the finite mixing leads to a deformation of every second anti-node (i.e., regions with constructive interference). The sliding average (yellow line in (b)) is slightly modulated. Finally, in Fig. 4.C.1(c), the terms $\propto \cos(\phi_a - \phi_b)$ in Eq. (4.9) and Eq. (4.10) induce a more prominent modulation of the transmission as a function of the phase difference. The average of the transmission clearly follows the modulation.

4.D Fabrication of Sample AD_CB14

The base of the structure is made of a conducting Si substrate with high positive doping with a $500\,\mu$m SiO_2 layer on top. The wafers are cut into 4×4 mm pieces, spin-coated with negative photoresist (Shipley Microposit 1805), and exposed to a mercury light source for 30 s under a optical mask. The mask allows the exposure of 25 structures with 6 contact pads on each structure. After developement, the sample is put in a vacuum and 40 nm Re is sputtered on top. After a lift-off of the remaining resist and the metall on top, only the contact pads remain. In a next step, PMMA-resist is spin-coated for an electron-beam lithography (EBL) process to define the smaller, sub-μm structures. After the development, 35 nm of Re is sputtered in vacuum followed by 5 nm of Pt. After another lift-off process, the metallic structures on the sample are complete. In a similar, final lithographical step, small dots of catalyst solution, composed of transition metal oxide and metalorganic particles suspended in methanol, are deposited in the center of the structures. They serve as seed particles for the CNT growth in a chemical-vapor deposition (CVD) process that takes place in a quartz tube at 900° C under an atmosphere of hydrogen and methane. The growth direction of the CNT can not be controlled within our setup. Hence, the design of the inner contact structures is chosen in a way to achieve a reasonable yield of CNTs that bridge two contacts. The CVD completes the fabrication process. We apply the CVD growth as the last step of the process in order to achieve

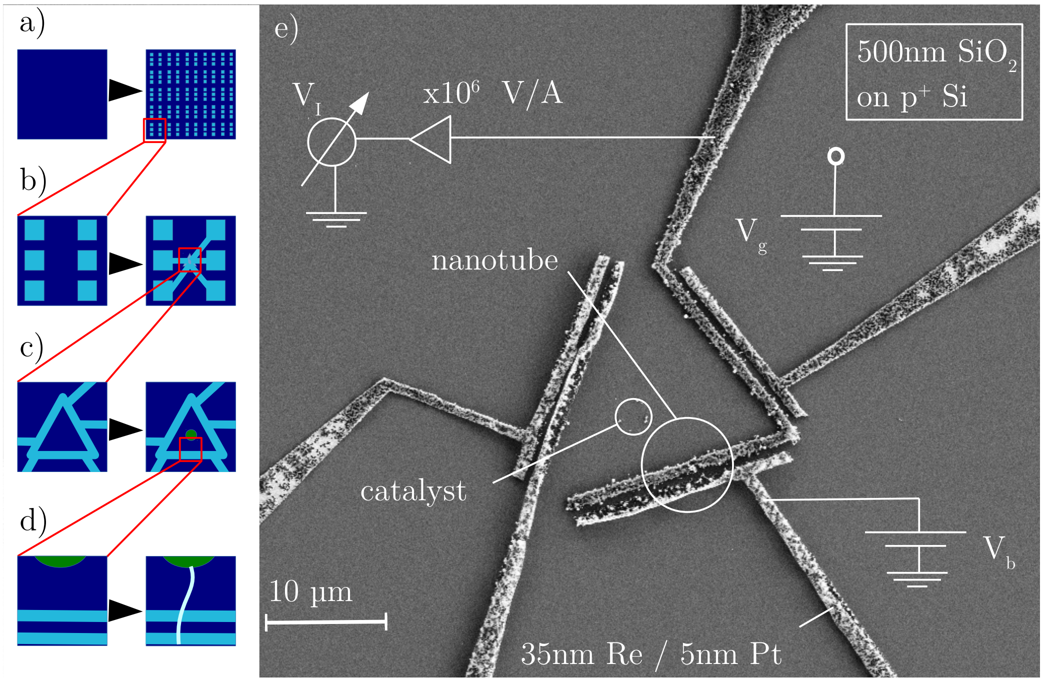

Figure 4.D.1: Overview of the fabrication process for sample AC_CB14. (a) Optical lithography is used to define the bonding pads. (b) In an EBL step, the inner structures that serve as contacts to the CNT are patterned and metallized. (c) A small quantity of catalyst is deployed by means of EBL lithography in the center of the structure. (d) In a chemical-vapor deposition (CVD) process, a CNT forms starting from the catalyst dot and bridging a pair of contacts. (e) Electron micrograph of a sample similar to sample (A) after the CVD process. The sample shows inner structures that are slightly deformed by melting during the CVD process. The measurment circuit is indicated by white symbols. Between a pair of contacts, a bias voltage V_b is applied. The current signal is amplified by a current-voltage amplifier with an amplification A. The resulting current is given by the product with the measured voltage signal $I = AV_\mathrm{I}$. The potential of the quantum dot can be changed by the global backgate voltage V_g.

defect free nanotubes [8]. We try to avoid any further steps that can lead to a contamination after the CVD step, including electron beam or force microscopy. Details on the parameters of each fabrication step can be found below.

4.D.1 Optical lithography

Si/Sio$_2$ samples, 8×8 mm in size, are cleaned by oxygen plasma and acetone. As a first step, we apply the Shipley S1805 positive photo-resist. The resist centrifuge is set to 4500 rpm for 30 s. On a hotplate, the resist is baked for 120 s. In a second step, a *Karl Suss MJB3* mask aligner is used to expose parts of the sample to ultra-violet light for 30 s. As a last step, a 1:3 NaOH/H_2O mixture is used to develop the resist by immersing the sample for $30 - 40$ s. The sample is cleaned by rinsing in high-purity water.

4.D.2 Electron beam lithography

Metal contacts We prepare the sample by rinsing with acetone and iso-propanol. As a resist, we deploy polymethyl-methacrylate (PMMA) 200k, dissolved in chlorobenzene (3.5%) by spin-coating in two phases: 5 s at 3000 rpm and 30 s at 8000 rpm. The resist is baked at 150 °C for 6 min.

For the electron beam lithography, a *Zeiss LEO* electronic microscope is used. Within high vacuum (pressure $< 2 \cdot 10^{-5}$ mbar), a small acceleration voltage of 10 kV is used to align the sample and reduce the exposure prior to the writing process. The lithography process for the metallic structures is performed at an acceleration voltage of 30 kV using a 30 μm aperture and an area dose of 195 μC/cm^2. The resulting beam current is 320 pA. We develop the exposed resist within a mixture of methyl-isobutylketone (MIBK) and iso-propanol (1:3) for 120 s and rinse the sample with iso-propanol for 30 s.

Catalyst dot As a resist, we apply two layers of resist: 2% PMMA (950k) on top of 7% PMMA (200k). For both layers, the spin-coating parameters are similar to the recipe for the contacts. During the EBL process, a higher area dose of 300 μC/cm^2 at 25 kV is used.

4.D.3 Metallization

In this step, a metal film with different layers is sputtered on top of the resist. Within a high-vacuum (10^{-8} mbar) chamber, we first create an argon plasma (Ar 6.0) at a power of 100 W yielding a deposition rate for Re of 1.5 Å/s. Within a second deposition step, we use an electron gun on a Pt target. At a

40 mg	$Fe(NO_3)_3 \cdot 9H_2O$
30 mg	Al_2O_3 nanoparticles
10 mg	$[CH_3COCH = COCH_3]_2MoO_2$

Table 4.D.1: Constituents of the catalyst solution serving as a seed for the chemical vapor deposition of the CNT.

gun current of 440 mA we typically obtain deposition rates of $0.1 - 0.2$ Å/s. The rates highly depend on the quality of the electron beam focus and the condition of the Pt target. The surplus metal is removed by keeping the sample in acetone at 60 C° for at least one day followed by additional rinsing within acetone with the help of a syringe.

4.D.4 Catalyst deployment

The constituents of the catalyst solution are given in Tab.4.D.1. One droplet is applied per 4×4 mm sample and blow-dried carefully. A uniform distribution of catalyst on the sample is desirable. On a hot-plate, the sample is baked for 6 min. For the lift-off, we immerse the sample in acetone for 4 min. The amount of catalyst particles on the sample is checked with an optical microscope. Additional rinsing is performed as needed.

4.D.5 CNT growth

The final step of the fabrication process is the chemical vapor deposition of the CNTs. Within a quartz tube attached to a gas handling system, the sample is heated under argon atmosphere (1500 sccm) to 850 °C. The argon valve is closed and the remaining argon is rinsed by hydrogen (20 sccm) for 10 min. The methane valve is opened to allow for a flow of 10 sccm. Under this conditions, CNTs form starting from the catalyst particles. After 15 min, we close the methane and hydrogen valves, open the argon valve again (1500 sccm) and initiate the cool-down.

4.E Transport characteristics of AD_CB14

AD_CB14 exhibits a high level of conductance up to $3.5G_0$ ($G_0 = e^2/h$), see Fig. 4.E.1. On the hole side, i.e., for values $V_g < 0.7\,\text{V}$ we clearly observe a Fabry-Perot interference pattern in Fig. 4.D.1(b) with a frequency doubling in the region $-8\,\text{V} < V_g < -5\,\text{V}$. On the electron side for $V_g > 2\,\text{V}$ the wave guide behavior can also be observed. The gate conversion factor is given by

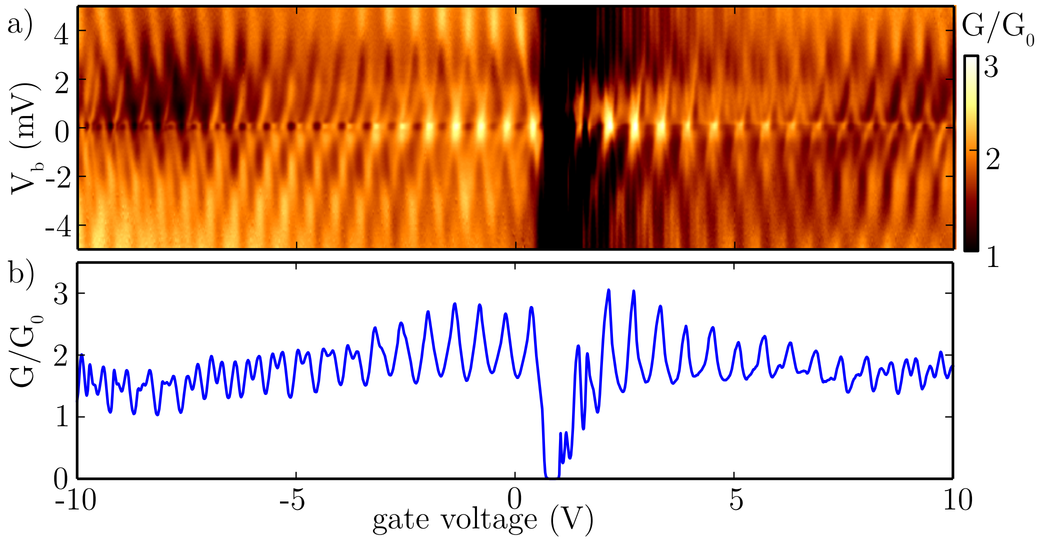

Figure 4.E.1: Differential conductance as a function of gate and bias voltage (a) and at zero bias (b). Besides an oscillation with the fundamental frequency f_1 that can be observed, e.g., in the region $-3\,\mathrm{V} < V_\mathrm{g} < 0\,\mathrm{V}$, secondary interference is visible on the left and on the right side of the gap above 6 V and below $-5\,\mathrm{V}$.

$\alpha_\mathrm{FP} = 0.0062 \pm 0.0005$ in these regions.[3] On the electron side in the range $1.5\,\mathrm{V} \leq V_\mathrm{g} \leq 1.0\,\mathrm{V}$, one charging state characteristic to transport in the Coulomb blockade regime can be distinguished. For the charging state we obtain $\alpha_\mathrm{CB} = 0.11$. The bandgap measures $40 \pm 5\,\mathrm{meV}$. The fundamental frequency of the Fabry-Perot transmission signal extracted by a Fourier analysis, $f_1 \simeq 250 \pm 20\,\frac{1}{eV}$, is related to the length of the cavity, L, as

$$L = \pi \hbar v_\mathrm{F} f_1. \tag{4.11}$$

At a Fermi velocity of 800 km/s [38], we estimate a length of $L \simeq 420 \pm 10\,\mathrm{nm}$, in agreement with the approximate height of the rhombic pattern, $\Delta V_\mathrm{b} \simeq 3.6\,\mathrm{meV} \simeq 1/\alpha f_1$, in Fig. 4.E.1(a). We summarize these FP transport characteristics in Tab. 4.E.1.

4.E.1 Properties of the Fabry-Perot cavity

Although $G(V_\mathrm{g})$ in Fig. 4.E.1 exhibits clear signs of secondary interference, an analysis similar to the one carried out for KG_R3BB lacks a minimal

---

[3] A discussion on the extraction of the lever arm in the ballistic FP regime can be found in Sec. 4.B.

$\alpha_{\mathrm{CB}}[\cdot 10^{-2}]$	$\alpha_{\mathrm{FP}}[\cdot 10^{-3}]$	E_{gap}	ΔE_{gap}	$f_1\,[\frac{1}{\mathrm{eV}}]$	L [μm]
1.1 ± 0.2	7.3 ± 0.4	40 ± 5	7.0 ± 0.5	250 ± 10	0.41 ± 0.03

Table 4.E.1: Gate conversion factors, energy gap, offset of the energy gap, fundamental frequency and length extracted for sample AD_CB14. α_{CB} is specific to the range $1.5\,\mathrm{V} \leq V_{\mathrm{g}} \leq 2.0\,\mathrm{V}$. For $V_{\mathrm{g}} < 0.7\,\mathrm{V}$ and $V_{\mathrm{g}} > 2.0\,\mathrm{V}$ we obtain α_{FP}. All energies are given in units of meV.

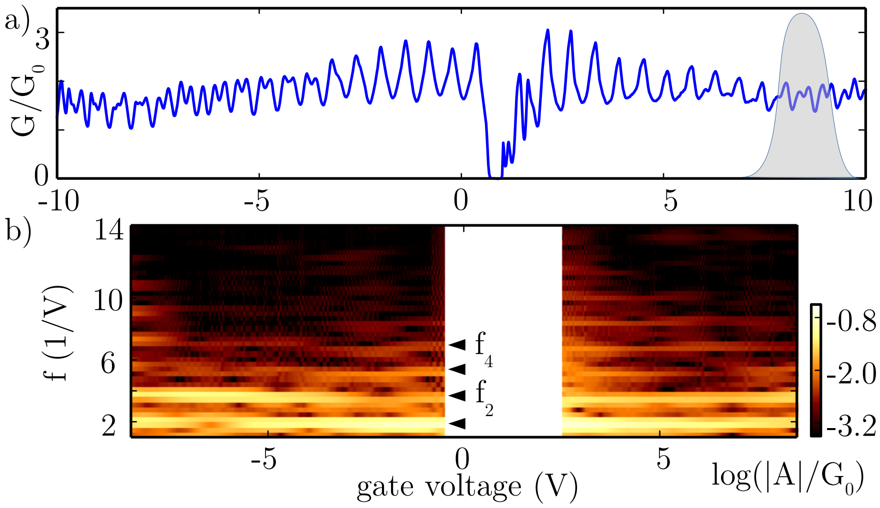

Figure 4.E.2: (a) Zero bias conductance $G(V_{\mathrm{g}})$. (b) Logarithmic plot of the FT amplitudes of (a) using a sliding window of width 3 V (grey shaded area). The amplitudes of the first four harmonics f_n, $n = 1, \ldots, 4$ appear as horizontal lines highlighted by small triangles.

number of periodic slow modulations. The extremal gate voltage values used in the conductance measurements are smaller, $-10\,\mathrm{V}$ and $10\,\mathrm{V}$. It is thus less likely to observe multiple periods of the secondary interference, since the period decreases for higher energies. At the same time, the tube is shorter by a factor of two and both the period of the primary and the period of the secondary interference are doubled.

However, the estimation of the average length of the electron path in the spirit of Sec. 3.2.3 is possible. In Fig. 4.E.2(a) we show $G(V_{\mathrm{g}})$ together with the logarithm of the FT amplitudes in (b). Up to six harmonics are visible as horizontal lines. Using Eq. (3.12) and Eq. (3.9) we estimate the average length of the electronic path from the decay of the amplitudes. Similar to the analysis in Sec. 3.2.3, the amplitudes are averaged over the gate voltage range to the right of the bandgap and over the range to the left of the bandgap,

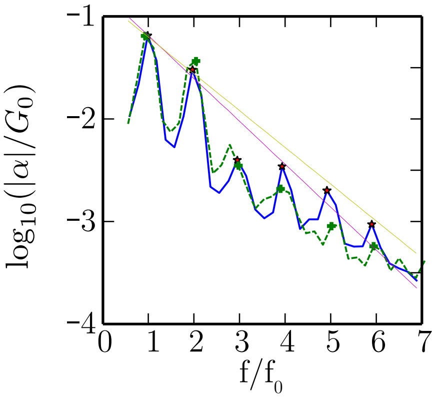

Figure 4.E.3: FT amplitudes averaged over the left, $V_\mathrm{g} < -0.5\,\mathrm{V}$ (green dashed line), and over the right side, $V_\mathrm{g} > 2.5\,\mathrm{V}$ (blue solid line), of the bandgap on the gate voltage axis. The decay of the amplitudes with the harmonic number is fitted using Eq. (3.12).

sample	T_avg	T_p	r_1	r_2	$l_\mathrm{avg}[L]$	$l_\mathrm{avg}^\mathrm{FT}[L]$
AD_CB14	0.46	0.76	0.71	0.35	1.1	1.4
KG_R3BB	0.24	0.47	0.97	0.33	1.3	1.8

Table 4.E.2: Table with extracted parameters for samples AD_CB14 and KG_R3BB. The reflection coefficients r_1 and r_2 are evaluated directly from the peak and average values of the conductance data. The two values in the last column for $l_\mathrm{avg}^\mathrm{FT}$ are extracted from the positive gate voltage range and the negative gate voltage range for AD_CB14 and for the ranges $-5\,\mathrm{V} < V_\mathrm{g} < -0.5\,\mathrm{V}$ and $-14\,\mathrm{V} < V_\mathrm{g} < -5\,\mathrm{V}$ for KG_R3BB, respectively.

respectively. This way we obtain the averaged amplitudes as a function of the frequency for the gate voltage ranges $-10\,\mathrm{V} < V_\mathrm{g} < -0.5\,\mathrm{V}$ (green dashed line in Fig. 4.E.3) and $2.5\,\mathrm{V} < V_\mathrm{g} < 10\,\mathrm{V}$ (blue line). From a fit to Eq. (3.12) we extract the product $|r_1||r_2|$ and calculate $l_\mathrm{avg}^\mathrm{FT}$. The results are shown in Tab. 4.E.2 together with an estimation of the path from the peak conductance and the average conductance (compare Sec. 3.2.3).

Sample AD_CB14 is more transparent and most electrons are directly transmitted. Again, the l_avg extracted directly from the conductance data is smaller than $l_\mathrm{avg}^\mathrm{FT}$ from the Fourier analysis.

Part IV

Concluding remarks

We study two conceptually different regimes of electronic transport in carbon nanotubes. In the first part, we start from the sequential tunneling description that is suitable for the Coulomb blockade regime and apply a non-perturbative extension, the *dressed-second order*(DSO) approach, to access the intermediate regime between Coulomb blockade and mixed-valence regime, where stronger correlations between quantum dot and contacts lead to the Kondo effect. The charge fluctuations that are accounted for in the DSO approach are sensitive to the ferromagnetic properties of the contacts. This enables us to analyze the specific features observed in the differential conductance and the tunneling magneto-resistance data. For even stronger coupling, we enter the regime of ballistic transport, where we observe electronic wave-interference phenomena, similar to the Fabry-Perot interference in optics. This is the subject of the second part. We find that the symmetries of the carbon nanotube are the key to the interpretation of the peculiar *secondary interference* patterns. The second part closes with experimental observations in the transparent regime that require a more detailed analysis. This collection of data is meant to encourage future studies which hopefully can answer the open questions connected to these experimental observations.

The two opposite regimes we discuss here are only two examples of a variety of phenomena that can often be observed in experiments on a single device, just by varying the gate voltage. From the measurement on sample CB3224, e.g., we briefly discussed the spectrum of excited states of the single-electron state in Sec. 1.2.3. Yet, already the spectrum of the two-electron state is subject to an ongoing analysis which would span a chapter on its own. When the coupling to the quantum dot on the CNT is increased in the very same measurement, for higher gate voltages, we obtain data that strikingly demonstrates a SU(4) Kondo effect, specific to CNTs. This part of the analysis is covered in Ref. [17] in detail. For negative gate voltages we observe hole transport in this sample, and a Fabry-Perot interference pattern, similar to the one we discussed in Ch. 3, is found. In yet another experiment on the same device, nanomechanical experiments focus on the vibrational degrees of freedom, see Ref. [52]. Pointing out this rich variety, we hope to convince the reader that electronic transport in carbon nanotubes is a versatile playground for the curious physicist that still deserves its unique standing among solid state material systems.

Acknowledgment

The results condensed in this thesis heavily rely on preceding work of colleagues that I, hopefully, have not forgotten to cite at the appropriate place. There is, however, a large amount of preceding work which can not be directly cited and is nevertheless indispensable for the success of a project. This is especially true if one tries to participate both in experimental and theoretical explorations without strong expertise in neither of the two.

In this spirit I thank Johannes Kern and Davide Mantelli from the theory department for the help with the DSO. These guys actually know how to do a proper calculation. Also from the theory group, there is Miriam del Valle and Magdalena Marganska who helped me to understand the CNT structure. To Magda again for relaxing duets with the clarinet, thanks and please excuse my frequent bail-outs. In the first measuring period I was kindly introduced to the cryo setup by Daniel Schmid and Peter Stiller. They also assisted me with fabricating my first CNT samples on my own - thank you. Kudos also to Klaus Kronfeldner for the constant support and help with the mixing cryostat. Thanks to Ina Schneider, Daniel Steininger, Ondrej Vavra and Lorentz Fuchs and to all the helping hands in the clean room and in the lab. Thanks for the support from my group, to Pascal Brunner, Karl Götz, Stefan Blien and Dominik Berndt. Thanks to Karl also for proliferating the use of colorview2d. With Nicola Paradiso I had much fun in the Fabry Perot project and the discussions were always inspiring. I like your style. I also enjoyed being part of the lab-measurement team, namely working with Christian Butschkow, Alexei Iankilevitch, and Andreas Hüttel. Who needs Lab-View as long as someone knows how to program Perl?

Thanks, Juri for your patience at lunchtime. I sabotaged your efficient daily schedules with great success. Finally, let me thank the three supervisors of mine, Milena Grifoni from the theory department, Christoph Strunk and Andreas Hüttel from the experimental division. Their combined effort enabled the hybrid position between experiment and theory and the two projects covered in this thesis.

Bibliography

[1] L. V. Radushkevich and V. M. Lukyanovich. "On the structure of carbon formed by thermal decomposition of carbon monoxide on iron contacts". In: *Zh. Fiz. Khim.* 26 (1952), p. 88.

[2] S. Iijima. "Helical microtubules of graphitic carbon". In: *Nature* 354.6348 (1991), pp. 56–58. ISSN: 0028-0836.

[3] A. Rahman et al. "Theory of ballistic nanotransistors". In: *IEEE Transactions on Electron Devices* 50.9 (2003), pp. 1853–1864. ISSN: 00189383.

[4] C. Subramaniam et al. "One hundred fold increase in current carrying capacity in a carbon nanotube-copper composite." en. In: *Nature communications* 4 (2013), p. 2202. ISSN: 2041-1723.

[5] R. K. Cavin, P. Lugli, and V. V. Zhirnov. "Science and Engineering Beyond Moore's Law". In: *Proceedings of the IEEE* 100.Special Centennial Issue (2012), pp. 1720–1749. ISSN: 0018-9219.

[6] *Moore's Law Is Showing Its Age.* `http://www.wsj.com/articles/moores-law-is-showing-its-age-1437076232`. Accessed: 2015-11-30.

[7] T. Simonite. "Carbon Nanotubes Could Step In to Sustain Moore's Law". In: *TECHNOLOGY REVIEW* 117.5 (2014), pp. 17–17. ISSN: 1099-274X.

[8] A. K. Hüttel et al. "Carbon nanotubes as ultrahigh quality factor mechanical resonators." In: *Nano letters* 9.7 (2009), pp. 2547–52. ISSN: 1530-6992.

[9] J. Moser et al. "Nanotube mechanical resonators with quality factors of up to 5 million." In: *Nature nanotechnology* 9.12 (2014), pp. 1007–11. ISSN: 1748-3395.

[10] M. J. Biercuk et al. "Anomalous conductance quantization in carbon nanotubes". In: *Physical Review Letters* 94.2 (2005), p. 26801. ISSN: 0031-9007.

[11] J.-P. Cleuziou et al. “Carbon nanotube superconducting quantum interference device.” In: *Nature nanotechnology* 1.1 (2006), pp. 53–9. ISSN: 1748-3395.

[12] A. Y. Kasumov. “Supercurrents Through Single-Walled Carbon Nanotubes”. In: *Science* 284.5419 (1999), pp. 1508–1511. ISSN: 00368075.

[13] N. Mason, M. J. Biercuk, and C. M. Marcus. “Local gate control of a carbon nanotube double quantum dot.” In: *Science (New York, N.Y.)* 303.5658 (2004), pp. 655–8. ISSN: 1095-9203.

[14] F. Kuemmeth et al. “Coupling of spin and orbital motion of electrons in carbon nanotubes.” In: *Nature* 452.7186 (Mar. 2008), pp. 448–52. ISSN: 1476-4687.

[15] T. Jespersen et al. “Gate-Dependent Orbital Magnetic Moments in Carbon Nanotubes”. In: *Physical Review Letters* 107.18 (2011), p. 186802. ISSN: 0031-9007.

[16] G. A. Steele et al. “Large spin-orbit coupling in carbon nanotubes.” In: *Nature communications* 4 (Jan. 2013), p. 1573. ISSN: 2041-1723.

[17] D. R. Schmid et al. “Broken SU(4) symmetry in a Kondo-correlated carbon nanotube”. In: *Physical Review B* 91.15 (Apr. 2015), p. 155435. ISSN: 1098-0121.

[18] T. S. Jespersen et al. “Gate-dependent spin–orbit coupling in multielectron carbon nanotubes”. In: *Nature Physics* 7.4 (2011), pp. 348–353. ISSN: 1745-2473.

[19] T. Kamimura, Y. Ohno, and K. Matsumoto. “Transition between Particle Nature and Wave Nature in Single-Walled Carbon Nanotube Device”. In: *Japanese Journal of Applied Physics* 48.1 (2009), p. 015005. ISSN: 0021-4922.

[20] E. A. Laird et al. “Quantum transport in carbon nanotubes”. In: *Reviews of Modern Physics* 87.3 (2015), pp. 703–764. ISSN: 0034-6861.

[21] W. Liang et al. “Fabry - Perot interference in a nanotube electron waveguide.” In: *Nature* 411.6838 (June 2001), pp. 665–9. ISSN: 0028-0836.

[22] A. Javey et al. “Ballistic carbon nanotube field-effect transistors.” In: *Nature* 424.6949 (2003), pp. 654–7. ISSN: 1476-4687.

[23] A. I. Ekimov, A. L. Efros, and A. A. Onushchenko. “Quantum size effect in semiconductor microcrystals”. In: *Solid State Communications* 56.11 (Dec. 1985), pp. 921–924. ISSN: 00381098.

[24] R. P. Andres et al. “"Coulomb Staircase" at Room Temperature in a Self-Assembled Molecular Nanostructure”. In: *Science* 272.5266 (May 1996), pp. 1323–1325. ISSN: 0036-8075.

[25] H. W. Postma et al. “Carbon nanotube single-electron transistors at room temperature.” In: *Science (New York, N.Y.)* 293.5527 (July 2001), pp. 76–9. ISSN: 0036-8075.

[26] S. Datta. *Electronic transport in mesoscopic systems*. Cambridge University Press, 1997, p. 377. ISBN: 0521599431.

[27] H. Grabert. “Dissipative quantum tunneling of two-state systems in metals”. In: *Physical Review B* 46.19 (Nov. 1992), pp. 12753–12756. ISSN: 0163-1829.

[28] C. J. Gorter. “A possible explanation of the increase of the electrical resistance of thin metal films at low temperatures and small field strengths”. In: *Physica* 17.8 (Aug. 1951), pp. 777–780. ISSN: 00318914.

[29] L. P. Kouwenhoven et al. “Electron transport in quantum dots.” In: *Proceedings of the Advanced Study Institute on Mesoscopic Electron Transport* (1997).

[30] M. Gaaß. “The Kondo effect in single wall carbon nanotubes with ferromagnetic contacts”. PhD thesis. University of Regensburg, 2011.

[31] R. Saito, M. Dresselhaus, and G. Dresselhaus. *Physical Properties Of Carbon Nanotubes*. World Scientific, 1998. ISBN: 978-1-86094-093-4.

[32] L. C. Venema. “Imaging Electron Wave Functions of Quantized Energy Levels in Carbon Nanotubes”. In: *Science* 283.5398 (Jan. 1999), pp. 52–55. ISSN: 00368075.

[33] X. Du et al. “Approaching ballistic transport in suspended graphene.” In: *Nature nanotechnology* 3.8 (2008), pp. 491–5. ISSN: 1748-3395.

[34] T. Ando. “Theory of Electronic States and Transport in Carbon Nanotubes”. en. In: *Journal of the Physical Society of Japan* 74.3 (Mar. 2005), pp. 777–817. ISSN: 0031-9015.

[35] A. H. Castro Neto et al. “The electronic properties of graphene”. In: *Reviews of Modern Physics* 81.1 (Jan. 2009), pp. 109–162. ISSN: 0034-6861.

[36] J. W. G. Wilder et al. “Electronic structure of atomically resolved carbon nanotubes”. In: 391.6662 (Jan. 1998), pp. 59–62. ISSN: 0028-0836.

[37] M. Marganska, P. Chudzinski, and M. Grifoni. “The two classes of low-energy spectra in finite carbon nanotubes”. In: *Physical Review B* 92.7 (Aug. 2015), p. 075433. ISSN: 1098-0121.

[38] M.S. Dresselhaus, G. Dresselhaus, and P.C. Eklund. *Science of Fullerenes and Carbon Nanotubes: Their Properties and Applications*. Academic Press, 1996, p. 965. ISBN: 0122218205.

[39] A. M. Lunde, K. Flensberg, and A.-P. Jauho. “Intershell resistance in multiwall carbon nanotubes: A Coulomb drag study”. In: *Physical Review B* 71.12 (Mar. 2005), p. 125408. ISSN: 1098-0121.

[40] C. Kane, L. Balents, and M. P. A. Fisher. “Coulomb Interactions and Mesoscopic Effects in Carbon Nanotubes”. In: *Physical Review Letters* 79.25 (1997), pp. 5086–5089. ISSN: 0031-9007.

[41] X. Zhao et al. “Smallest carbon nanotube is 3 a in diameter.” In: *Physical review letters* 92.12 (2004), p. 125502. ISSN: 0031-9007.

[42] S. Bandow et al. “Effect of the Growth Temperature on the Diameter Distribution and Chirality of Single-Wall Carbon Nanotubes”. In: *Physical Review Letters* 80.17 (1998), pp. 3779–3782. ISSN: 0031-9007.

[43] M. Ouyang et al. “Energy gaps in "metallic" single-walled carbon nanotubes.” In: *Science (New York, N.Y.)* 292.5517 (2001), pp. 702–5. ISSN: 0036-8075.

[44] V. N. Popov. “Curvature effects on the structural, electronic and optical properties of isolated single-walled carbon nanotubes within a symmetry-adapted non-orthogonal tight-binding model”. In: *New Journal of Physics* 6 (2004), pp. 17–17. ISSN: 1367-2630.

[45] L. P. Kouwenhoven, D. G. Austing, and S. Tarucha. “Few-electron quantum dots”. In: *Reports on Progress in Physics* 64.6 (June 2001), pp. 701–736. ISSN: 0034-4885.

[46] Y. Oreg, K. Byczuk, and B. I. Halperin. “Spin Configurations of a Carbon Nanotube in a Nonuniform External Potential”. In: *Physical Review Letters* 85.2 (July 2000), pp. 365–368. ISSN: 0031-9007.

[47] L. Mayrhofer and M. Grifoni. “The spectrum of interacting metallic carbon nanotubes: exchange effects and universality”. In: *The European Physical Journal B* 63.1 (2008), pp. 43–58. ISSN: 1434-6028.

[48] A. Makarovski et al. “Persistent orbital degeneracy in carbon nanotubes”. In: *Physical Review B* 74.15 (Oct. 2006), p. 155431. ISSN: 1098-0121.

[49] S. Sapmaz et al. “Electronic excitation spectrum of metallic carbon nanotubes”. In: *Physical Review B* 71.15 (Apr. 2005), p. 153402. ISSN: 1098-0121.

[50] M. T. Woodside and P. L. McEuen. “Scanned probe imaging of single-electron charge states in nanotube quantum dots.” In: *Science (New York, N.Y.)* 296.5570 (May 2002), pp. 1098–101. ISSN: 1095-9203.

[51] H. Ajiki and T. Ando. “Electronic States of Carbon Nanotubes”. en. In: *Journal of the Physical Society of Japan* 62.4 (Apr. 1993), pp. 1255–1266. ISSN: 0031-9015.

[52] D. R. Schmid. “Suspended Carbon Nanotubes as Electronical and Nano-Electro-Mechanical Hybrid Systems in the Quantum Limit”. PhD thesis. University of Regensburg, 2014.

[53] T. Ando. “Spin-Orbit Interaction in Carbon Nanotubes”. In: *Journal of the Physics Society Japan* 69.6 (June 2000), pp. 1757–1763. ISSN: 0031-9015.

[54] E. McCann and V. I. Fal’ko. “Degeneracy breaking and intervalley scattering due to short-ranged impurities in finite single-wall carbon nanotubes”. In: *Physical Review B* 71.8 (Feb. 2005), p. 085415. ISSN: 1098-0121.

[55] J. Von Neumann. *Mathematical foundations of quantum mechanics.* Princeton [N.J.]: Princeton University Press, 1955. ISBN: 9780691028934.

[56] K. Blum. *Density Matrix Theory and Applications.* 2012. ISBN: 3642205615.

[57] J. Kern and M. Grifoni. “Transport across an Anderson quantum dot in the intermediate coupling regime”. In: *The European Physical Journal B* 86.9 (Sept. 2013), p. 384. ISSN: 1434-6028.

[58] A. Dirnaichner et al. “Transport across a carbon nanotube quantum dot contacted with ferromagnetic leads: Experiment and nonperturbative modeling”. In: *Physical Review B* 91.19 (May 2015), p. 195402. ISSN: 1098-0121.

[59] E. Wigner. “On the Quantum Correction For Thermodynamic Equilibrium”. In: *Physical Review* 40.5 (1932), pp. 749–759. ISSN: 0031-899X.

[60] K.-S. Kim, H.-J. Kim, and M. Sasaki. “Boltzmann equation approach to anomalous transport in a Weyl metal”. In: *Physical Review B* 89.19 (May 2014), p. 195137. ISSN: 1098-0121.

[61] C. W. J. Beenakker. “Theory of Coulomb-blockade oscillations in the conductance of a quantum dot”. In: *Physical Review B* 44.4 (July 1991), pp. 1646–1656. ISSN: 0163-1829.

[62] Y. Meir, N. S. Wingreen, and P. A. Lee. “Transport through a strongly interacting electron system: Theory of periodic conductance oscillations”. In: *Physical review letters* 66.23 (1991), pp. 3048–3051.

[63] J. König et al. “Resonant tunneling through ultrasmall quantum dots: Zero-bias anomalies, magnetic-field dependence, and boson-assisted transport”. In: *Physical Review B* 54.23 (Dec. 1996), pp. 16820–16837. ISSN: 0163-1829.

[64] H.-P. Breuer and F. Petruccione. *The Theory of Open Quantum Systems*. 2002. ISBN: 0198520638.

[65] T. Mori and S. Miyashita. “Dynamics of the Density Matrix in Contact with a Thermal Bath and the Quantum Master Equation”. en. In: *Journal of the Physical Society of Japan* 77.12 (2008), p. 124005. ISSN: 0031-9015.

[66] R. C. Iotti, E. Ciancio, and F. Rossi. “Quantum transport theory for semiconductor nanostructures: A density-matrix formulation”. In: *Physical Review B* 72.12 (2005), p. 125347. ISSN: 1098-0121.

[67] A. G. Redfield. “On the Theory of Relaxation Processes”. English. In: *IBM Journal of Research and Development* 1.1 (1957), pp. 19–31. ISSN: 0018-8646.

[68] I. Knezevic and B. Novakovic. “Time-dependent transport in open systems based on quantum master equations”. In: *Journal of Computational Electronics* 12.3 (2013), pp. 363–374. ISSN: 1569-8025.

[69] S. Koller. “Spin phenomena and higher order effects in transport across interacting quantum-dots”. PhD thesis. Universität Regensburg, 2009.

[70] S. Koller, L. Mayrhofer, and M. Grifoni. “Spin transport across carbon nanotube quantum dots”. In: *New Journal of Physics* 9.9 (Sept. 2007), pp. 348–348. ISSN: 1367-2630.

[71] A. Cottet et al. “Controlling spin in an electronic interferometer with spin-active interfaces”. In: *Europhysics Letters (EPL)* 74.2 (Apr. 2006), pp. 320–326. ISSN: 0295-5075.

[72] J. Barnaś and I. Weymann. “Spin effects in single-electron tunnelling”. In: *Journal of Physics: Condensed Matter* 20.42 (Oct. 2008), p. 423202. ISSN: 0953-8984.

[73] S. Sahoo et al. “Electric field control of spin transport”. In: *Nature Physics* 1.2 (Oct. 2005), pp. 99–102. ISSN: 1476-0000.

[74] J. Samm et al. “Optimized fabrication and characterization of carbon nanotube spin valves”. In: *Journal of Applied Physics* 115.17 (May 2014), p. 174309. ISSN: 0021-8979.

[75] S. Koller, M. Grifoni, and J. Paaske. “Sources of negative tunneling magnetoresistance in multilevel quantum dots with ferromagnetic contacts”. In: *Physical Review B* 85.4 (Jan. 2012), p. 045313. ISSN: 1098-0121.

[76] Y. Alhassid et al. “Linear conductance in Coulomb-blockade quantum dots in the presence of interactions and spin”. In: *Physical Review B* 69.11 (Mar. 2004), p. 115331. ISSN: 1098-0121.

[77] J. Holm et al. “Gate-dependent tunneling-induced level shifts observed in carbon nanotube quantum dots”. In: *Physical Review B* 77.16 (Apr. 2008), p. 161406. ISSN: 1098-0121.

[78] H. Aurich et al. “Permalloy-based carbon nanotube spin-valve”. In: *Applied Physics Letters* 97.15 (2010), p. 153116. ISSN: 00036951.

[79] D. Choo et al. “A model of the magnetic properties of coupled ferromagnetic/antiferromagnetic bilayers”. In: *Journal of Applied Physics* 101.9 (2007), 09E521. ISSN: 00218979.

[80] A. Cottet and M.-S. Choi. “Magnetoresistance of a quantum dot with spin-active interfaces”. In: *Physical Review B* 74.23 (Dec. 2006), p. 235316. ISSN: 1098-0121.

[81] J. Gramich et al. *Fork stamping of pristine carbon nanotubes onto ferromagnetic contacts for spin-valve devices.* Apr. 2015. URL: `http://arxiv.org/abs/1504.05693`.

[82] J. P. Cleuziou et al. “Interplay of the Kondo Effect and Strong Spin-Orbit Coupling in Multihole Ultraclean Carbon Nanotubes”. In: *Physical Review Letters* 111.13 (Sept. 2013), p. 136803. ISSN: 0031-9007.

[83] J. Soo Lim et al. “Kramers polarization in strongly correlated carbon nanotube quantum dots”. In: *Physical Review B* 83.15 (Apr. 2011), p. 155325. ISSN: 1098-0121.

[84] M. Rontani. *Anomalous magnetization of a carbon nanotube as an excitonic insulator.* 2014. URL: `http://arxiv.org/abs/1405.3108`.

[85] M. F. Crommie, C. P. Lutz, and D. M. Eigler. “Confinement of electrons to quantum corrals on a metal surface.” In: *Science (New York, N.Y.)* 262.5131 (Oct. 1993), pp. 218–20. ISSN: 0036-8075.

[86] E. J. Heller et al. “Scattering and absorption of surface electron waves in quantum corrals”. In: *Nature* 369.6480 (June 1994), pp. 464–466. ISSN: 0028-0836.

[87] M. A. Topinka. “Imaging Coherent Electron Flow from a Quantum Point Contact”. In: *Science* 289.5488 (Sept. 2000), pp. 2323–2326. ISSN: 00368075.

[88] A. F. Young and P. Kim. “Quantum interference and Klein tunnelling in graphene heterojunctions”. In: *Nature Physics* 5.3 (Feb. 2009), pp. 222–226. ISSN: 1745-2473.

[89] S. J. Tans et al. “Individual single-wall carbon nanotubes as quantum wires”. In: *Nature* 386.6624 (1997), pp. 474–477. ISSN: 0028-0836.

[90] C. T. White and T. N. Todorov. “Quantum electronics. Nanotubes go ballistic.” In: *Nature* 411.6838 (2001), pp. 649–651. ISSN: 0028-0836.

[91] J. Kong et al. “Quantum Interference and Ballistic Transmission in Nanotube Electron Waveguides”. In: *Physical Review Letters* 87.10 (Aug. 2001), p. 106801. ISSN: 0031-9007.

[92] H. Man, I. Wever, and A. Morpurgo. “Spin-dependent quantum interference in single-wall carbon nanotubes with ferromagnetic contacts”. In: *Physical Review B* 73.24 (2006), p. 241401. ISSN: 1098-0121.

[93] J. Jiang, J. Dong, and D. Xing. “Quantum Interference in Carbon-Nanotube Electron Resonators”. In: *Physical Review Letters* 91.5 (Aug. 2003), p. 056802. ISSN: 0031-9007.

[94] H. Jiang et al. “The effect of uniaxial and torsional deformations on quantum interference of carbon nanotubes”. In: *Physics Letters A* 351.4-5 (2006), pp. 308–313. ISSN: 03759601.

[95] L. Yang et al. “Quantum interference in carbon nanotube electron resonators”. In: *Physical Review B* 69.15 (2004), p. 153407. ISSN: 1098-0121.

[96] A. Dirnaichner et al. *Secondary electron interference from trigonal warping in clean carbon nanotubes.* 2016. URL: `http://arxiv.org/abs/1602.03866`.

[97] J. R. Taylor. *An Introduction to Error Analysis: The Study of Uncertainties in Physical Measurements.* 1997. ISBN: 093570275X.

[98] D. Hofstetter and R. L. Thornton. “Theory of loss measurements of Fabry – Perot resonators by Fourier analysis of the transmission spectra”. In: *Optics Letters* 22.24 (1997), pp. 1831–1833.

[99] V. V. Deshpande et al. “Mott insulating state in ultraclean carbon nanotubes.” In: *Science (New York, N.Y.)* 323.5910 (2009), pp. 106–10. ISSN: 1095-9203.

[100] J. Lee et al. “Real Space Imaging of One-Dimensional Standing Waves: Direct Evidence for a Luttinger Liquid”. In: *Physical Review Letters* 93.16 (Oct. 2004), p. 166403. ISSN: 0031-9007.

[101] N. Y. Kim et al. “Tomonaga-Luttinger Liquid Features in Ballistic Single-Walled Carbon Nanotubes: Conductance and Shot Noise”. In: *Physical Review Letters* 99.3 (2007), p. 036802. ISSN: 0031-9007.

[102] A. P. Micolich. “What lurks below the last plateau: experimental studies of the $0.7 \cdot 2e^2/h$ conductance anomaly in one-dimensional systems.” en. In: *Journal of physics. Condensed matter : an Institute of Physics journal* 23.44 (2011), p. 443201. ISSN: 1361-648X.

[103] J. Heyder et al. “Relation between the 0.7 anomaly and the Kondo effect: Geometric crossover between a quantum point contact and a Kondo quantum dot”. In: *Physical Review B* 92.19 (2015), p. 195401. ISSN: 1098-0121.

[104] F. Bauer et al. “Microscopic origin of the ‘0.7-anomaly’ in quantum point contacts”. In: *Nature* 501.7465 (2013), pp. 73–78. ISSN: 0028-0836.

[105] D. Tománek and S. G. Louie. “First-principles calculation of highly asymmetric structure in scanning-tunneling-microscopy images of graphite”. In: *Physical Review B* 37.14 (1988), pp. 8327–8336. ISSN: 0163-1829.

[106] M. del Valle, M. Margańska, and M. Grifoni. “Signatures of spin-orbit interaction in transport properties of finite carbon nanotubes in a parallel magnetic field”. In: *Physical Review B* 84.16 (2011), p. 165427. ISSN: 1098-0121.

[107] M. del Valle et al. “Tuning the conductance of a molecular switch.” In: *Nature nanotechnology* 2.3 (2007), pp. 176–9. ISSN: 1748-3395.

[108] C. J. Lambert and D. Weaire. “Decimation and Anderson Localization”. In: *physica status solidi (b)* 101.2 (1980), pp. 591–595. ISSN: 03701972.

[109] S. Krompiewski, J. Martinek, and J. Barnaś. “Interference effects in electronic transport through metallic single-wall carbon nanotubes”. In: *Physical Review B* 66.7 (2002), p. 073412. ISSN: 0163-1829.

[110] M. Born. *Principles of optics electromagnetic theory of propagation, interference, and diffraction of light.* Oxford ;New York: Pergamon Press, 1964.